UNIVERSITY OF COPENHAGEN
FACULTY OF SCIENCE

Doctoral Thesis

Morten Ankersen Medici

Search for Dark Matter Annihilation in the Galactic Halo using IceCube

Academic supervision by Jason Koskinen and Stefania Xella

November 2016

Abstract

The existence of dark matter has by now been demonstrated to such a degree that the next step is to understand what actually constitute this unknown gravitational mass. The total amount of matter in the universe cannot be explained without the introduction of a particle beyond the Standard Model, and with the right properties of this hypothesized particle, it is possible to look for a signal from dark matter annihilation. In this work, the dark matter particle candidate of weakly interacting massive particles shall be presented, and the possibilities of observing it's self-annihilation to neutrinos shall be pursued with the IceCube Neutrino Observatory located in the dark clear ice deep underneath the South Pole.

An infill to IceCube with a denser instrumentation allows the detection of neutrinos with energies down to 10 GeV. By using this sub-detector as the fiducial volume, and the rest of IceCube as a veto detector for atmospheric muons it is possible to search for a neutrino signals form the center of the Milky Way located on the souther hemisphere. In this thesis, a complete analysis is carried out on data from 1004 days of IceCube data, looking for an excess of neutrinos consistent with the dark matter halo of the Milky Way over a uniform atmospheric background. No significant excess is observed, and constraints are presented for the thermally averaged product of the self-annihilation cross-section and the relative speed $\langle \sigma v \rangle$, which for the annihilation of a 100 GeV WIMP through W^+W^-, result in a limit at $\langle \sigma v \rangle = 3.84 \cdot 10^{-23} \mathrm{cm}^3\mathrm{s}^{-1}$. The result of the present analysis improves the previous IceCube limits below masses of weakly interacting massive particles of 500 GeV and constitute current world leading results of weakly interacting massive particles annihilting to neutrino for masses between 50 and 200 GeV.

Resumé

Eksistensen af mørkt stof er idag demonstreret i så stor grad at det næste skridt er at forstå hvad der udgœr denne ukendte gravatationelle masse. Den samlede masse i universet kan ikke forklares uden at introducere eksotisk partikel uden for Standard Modellen. Hvis denne hypotetiske partikel har de rette egenskaber er det muligt at lede efter et signal fra mœrkt stof der annihilerer i universet, hvor særligt signalet fra Mælkevejen er forventet til at være særligt kraftigt. I denne afhandling bliver svagt vekselvirkende partikler med masse introduceret, og mulighederne for at detektere deres selv-annihilation til neutrino forfœlges ved hjælp af IceCube Neutrino Observatorie bygget i den mœrke klare is dybt under Sydpolen.

Et segment af IceCube har en tættere instrumenteres der giver mulighed for at detektere neutrinoer med energier ned til 10 GeV. Ved hjælp af denne sub-detektor udfœres en jagt efter selv-annihilation af svagt vekselvirkende massive partikler til neutrinoer. I denne afhandler er den komplette analyse af 1004 dage med data fra IceCube beskrevet. Intet significant signal blev detekteret og istedet sætter denne analyse en grænse for mulige værdiger af selv-annihilations raten $\langle \sigma v \rangle$ til neutrinoer, som for selv annihlation at en 100 GeV partikel der annihilerer til neutrinor gennem W^+W^-, svarer til $\langle \sigma v \rangle = 3.84 \cdot 10^{-23} \mathrm{cm}^3\mathrm{s}^{-1}$. Resultaterne præsenteret sætter verdens førende grænseværdier på $\langle \sigma v \rangle$ for masser mellem 50 og 250 GeV.

Acknowledgements

I am grateful to my functioning supervisor Jason, I managed to finish my main analysis on time, and arrive at the best limits in the world. You do not settle for less. Even though those disappointed eyes can fill me with shame in an instant, you manage to help, guide, and challenge in equal amounts. It has been a pleasure to test drive you as a PhD advisor, you have earned your next student.

Thanks to Stefania to providing me the opportunity to participate in the amazing program of neutrino physics, it is a pleasure to see faculty member pursuing new topics, and providing the means to execute it.

I have had a great suite of office mates. First with a fan of exploring the ironic to the limit, thanks for pushing it to the line Joakim, there is no reason to settle for less. Michael has acted a my personal mentor into the nitty gritty details of IceCube, thanks for being extremely patient and immensely helpful throughout all the hours in the office. Eva always had a great skill of bringing joy and entertainment to the office, please continue that trend whereever you go, remember to stretch during the day. With the latest addition of Tom a new level of nice seems to be have been settled in the office. I hope to spend more time with everyone of you, even when we go our separate ways.

Ken is the most friendly man in the universe, and you were part of making my stay abroad in Toronto the most amazing experience. My only regret is that I never got up early enough to join you in the gym. It is always a pleasure to have you around, and I think you should guide many more students, because you make it a pleasure being an exploring physicist.

Thanks to past, present and newly started students and PostDocs within high energy physics and cosmology at NBI for finding topics to discuss, for being clever, and for having fun.

At the Niels Bohr Institute there are a plenitude of clever minds, with expertise on more than a few topics, and it is great that you take the time to go over topics and discussions one more time. The brightest critic I found in Subir, who always has the nerve to tell people off, getting away with it because he is right. Philip has been extremely helpful, and a pleasure to know, even though I am not sure if the appreciation go both ways.

Within IceCube there are too many to thanks, but you all know who you are. Good people in IceCube, thanks for joining IceCube Swimming Club (special thanks to Alexander Stasik for cofounding) Thanks to my parents for taking care of me, in many different ways. You have truly made me to whom I am, which among others have given me the drive to pursue and complete this thesis. It is amazing how much love and passion you show for me and my interest, and I am proud to have you as my parents. Kristine, my sweetest darling, the time with you is only getting better, and seeing how you manage to put up with me when I am under pressure, with optimism, happiness and love. You are my wonderful missus, thanks for taking me with you on our next adventure.

Throughout the thesis, IceCube Neutrino Observatory shall be referred to as IceCube. In order not to create any confusion for those rap music fans out there, who are envious of having a picture taken with IceCube, I present a picture with me and the real IceCube in Figure 0.1 (at least the more photogenenic part of IceCube).

Figure 0.1: The author posing alongside IceCube

Contents

1 Dark matter **1**
- 1.1 Evidence for dark matter . . . 1
- 1.2 Dark matter candidates . . . 5
- 1.3 Detection techniques . . . 9
- 1.4 Dark matter distributions in the Milky way . . . 12
- 1.5 Neutrino signal from dark matter annihilation . . . 13

2 Neutrino astrophysics and matter interaction **17**
- 2.1 Neutrino oscillations . . . 17
- 2.2 Neutrino interactions . . . 19
- 2.3 Cherenkov radiation . . . 21
- 2.4 It came from outer space . . . 24

3 IceCube Neutrino Observatory **27**
- 3.1 South Pole ice as detection medium . . . 27
- 3.2 Photon signals in the ice . . . 30
- 3.3 Detection technology . . . 32
- 3.4 Detector layout . . . 34
- 3.5 Events in the detector . . . 35
- 3.6 Data processing . . . 37
- 3.7 Detector stability . . . 39

4 IceCube Event Simulation **43**
- 4.1 Particle event generation and/or interaction simulation . . . 43
- 4.2 Particle propagation . . . 44
- 4.3 Photon propagation . . . 45
- 4.4 Noise emulation . . . 45
- 4.5 Detector response simulation . . . 46

5 Data selection **49**
- 5.1 Signal and background components . . . 49
- 5.2 Datasets and blindness . . . 50
- 5.3 Event selection strategy . . . 52
- 5.4 Cut level 2 . . . 53
- 5.5 Cut level 3 . . . 53
- 5.6 Cut level 4 . . . 55
- 5.7 Cut level 5 . . . 63

5.8 Level 6 variables 66
5.9 Prioritized list of variables at level 6 73
5.10 Multivariate analysis tool - the boosted decision tree 73
5.11 Event rates and effective area 75
5.12 Final data properties 77

6 Analysis method **81**
6.1 Producing PDFs 81
6.2 Likelihood formulation 84
6.3 Statistical treatment of analysis 84
6.4 Systematic uncertainties 87

7 Results **95**
7.1 Unblinding data 95
7.2 Comparisons to other experiments 101
7.3 Outlook 101

8 Conclusion **105**

Bibliography **107**

1

Dark matter

Most of our universe seems to be composed of some gravitational mass that is not gas, dust, rocks, planet, stars, or supermassive black holes. It does not interact with electromagnetic radiation and has, as such, been named *dark matter* (DM). The history of dark matter is not long and starts (like many other good stories in physics) with the observation of something that is out of the ordinary[1, 2]. The evidence for particle dark matter shall here be presented and the possibility of a neutrino signal from annihilating Weakly Interacting Massive Particles (WIMPs) will be discussed.

1.1 Evidence for dark matter

The mystery started in 1933 with Fritz Zwickys measurement of the Coma cluster by, which showed a surprisingly large spread in velocity of the galaxies (then referred to as nebulae) in the cluster. The spread in velocities was used as a measure for the rotational speed of the individual galaxies in the cluster (as the entire cluster is also moving), and it was much higher than what the apparent luminous mass should be able to sustain without the cluster breaking apart. Specifically, Zwicky estimated that, if the Coma cluster is in a stationary equilibrium, the average spread in velocity should be 80 km/s, whereas the observation of a difference in velocity of 1500-2000 km/s would require a 400 times larger density of the Coma cluster[3]. Even when considering more conservative estimates of the distribution of the mass in Coma, each galaxy would need to be about 150 times more massive than local galaxies of the same brightness[4]. A similar discrepancy was observed for the Virgo cluster around the same time[5]. Either the calculation (or the observations) was wrong and the apparent additional mass did not exist, or maybe it "*represents a great mass of internebular material within the cluster*"[6] as Sinclair Smith formulated it in the conclusions of his study of the Virgo cluster. Even though the idea of it being something else than ordinary matter was only formulated later[7, 8], this quote from Smith turned out to be right, which can be understood from the current amount of evidence for this unknown gravitational mass in and between galaxies.

1.1.1 Rotational speed curves

The rotational speed curves of galaxies and galaxy clusters were the first place that the existence of dark matter was observed. For a collection of massive objects, the velocity $v(r)$ of an object bound to that system at a given radius r, is determined from the integrated mass $M(r)$ within a shell at that radius. From Newtonian

dynamics of circular motion and Newtons law of universal gravitation, $v(r)$ can be calculated as[9]:

$$v(r) = \sqrt{\frac{GM(r)}{r}}, \tag{1.1}$$

where G is the gravitational constant. By measuring the velocity of e.g. galaxies in a cluster, the distribution of mass in the cluster can be determined, or conversely the expected velocities can be estimated from the measured mass of the cluster. The mass of e.g. the Coma cluster was estimated from the luminosity of the cluster[3], by comparing it to the luminosity of galaxies for which the masses were more well established. And the mystery arose from the fact that those two mass measurements were in conflict; there was more mass in the clusters than the luminous mass could account for.

The same indications of 'missing mass' appeared with the first studies of the rotation of the individual galaxies, based on the velocity of bright stars[10]. The galaxy NGC 3115 offers particularly clear measurements of the rotational velocities, as it is seen 'edge on' from Earth[2], resulting in a smaller uncertainty on the rotational velocities. Again, a similar observation was made by Jan Hendrik Oort, where it was observed that the light density in NGC 3115 decreased more sharply at higher radii than the mass density (inferred from rotational velocities). Oort concluded that "*The strongly condensed luminous system appears embedded in a large and more or less homogeneous mass of great density*"[11].

A typical rotation curve for a galaxy is presented in Figure 1.1, where the measured data points clearly deviate from the expectation based on the luminous matter in the dashed line[12]. There is also a contribution from hot gas, constrained using the hydrogen 21 cm line[13]. However, that is still not enough to describe the observation, and an additional component is added to the fit; a spherical halo of dark matter. The matter contribution of the dark matter halo (indicated with the dot-dashed line) is then estimated from a fit of the three components to the observed data.

While this is a compelling argument for the existance of dark matter, rotation curves are not the only evidence for a non-luminous component of mass in the universe.

1.1.2 Gravitational Lensing

Following the theory of general relativity, massive potential wells modify the geodesics (i.e. the space-time equivalent of a straight line) as a generalized gravitational force, such that the path of light will be bent by the gravity of massive objects. Those objects effectively behave as lenses distorting the light arriving at earth from distant galaxies. From the amount of lensing, the gravitational mass of the lensing objects along the line of sight of a distant source can be determined[15]. If the lensing object is directly between the observer, and the source and is massive enough, a *strong lensing* of the source object can be observed. In this situation the gravitational mass can be determined by comparing observations to the expectations for the light pattern (e.g. modelled with simulations)[16]. However, often the lensing is only distorting the light from the distant galaxies very slightly, and it is essential to exploit the general lensing of a collection of galaxies. This *weak lensing* is

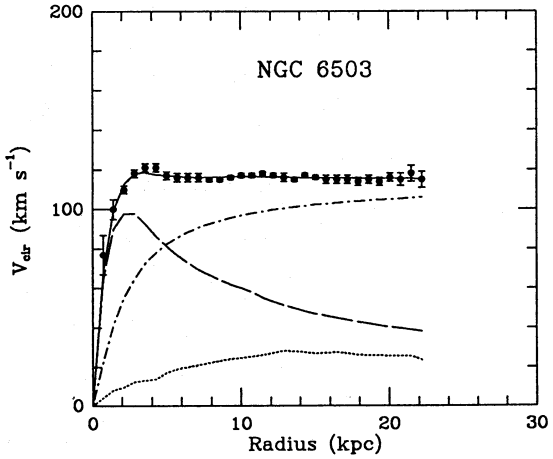

Figure 1.1: Rotation curve for NGC 6503, with the measurements represented by dots, and the individual components of the visible mass, gas, and a dark matter halo, in dashed, dotted, and dot-dashed line respectively. The dark matter halo distribution is fit such that the sum (presented in solid line) matches the data (modified from Ref. [14]).

thus more of a statistical measure of the average shear, determining the amount of gravitational mass in a region. It is the most common method of determining the mass distribution in the universe, and provides evidence for dark matter on all scales with a direct measure of the non-luminous gravitational mass[17].

1.1.3 Baryon Acoustic Oscillations

The Cosmic Microwave Background (CMB) provides information about the universe at the time of recombination, i.e. the point in time when the photons energy had decreased enough to no longer ionize atoms in the universe. At that point photons could stream freely through the universe, before which the photons interacted strongly with the charged protons and electrons of the early universe[18]. Today it is observed as the CMB, a nearly uniform distribution of light. However, the CMB exhibits minute anisotropies, corresponding to the energy density anisotropies in the universe at the time of recombination. Before recombination, the density of baryonic matter would be affected by the attraction of gravitationally overdense regions and the expansion of regions where the resulting overdensity caused the radiation pressure to build up and push back on the baryons. These *baryon acoustic oscillations* abruptly ended at recombination when the photons escaped the baryonic matter and the radiation pressure vanished, and density anisotropies (over- or underdensities) in the early universe are now imprinted in the CMB[19].

The deviations from the uniform temperature map of the CMB are mapped to a power spectrum in terms of spherical harmonic functions. The power spectrum of a given universe will be dependent on the energy density and it's distribution between different components in the universe, as illustrated in Figure 1.2. The energy density ρ is typically presented relative to the critical energy density ρ_c (for which the spatial geometry of the universe is flat), since the density fraction, $\Omega = \rho/\rho_c$, is independent of the size of the universe. More baryons in the early universe will enhance both the gravitational potentials and the radiation pressure,

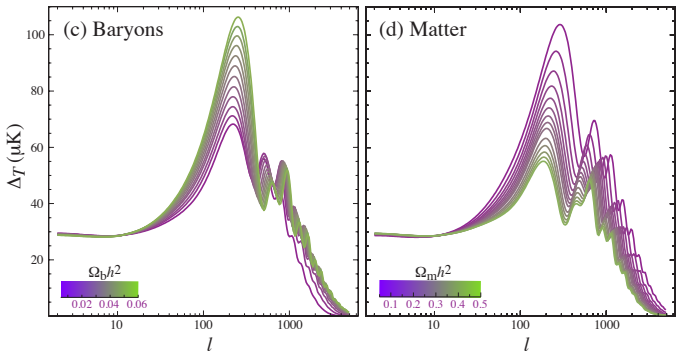

Figure 1.2: The power spectrum describing the amplitude of the baryon acoustic oscillations (measured as a temperature difference, ΔT, in the CMB) is affected by the exact energy/mass density of e.g. baryons, Ω_b, and the general density of matter, Ω_m. A large baryon density will enhance the baryon acoustic oscillations, whereas an increasing amount of dark matter will dampen the oscillations, because the gravitational potentials will dominate over the radiation pressure (modified from Ref. [19]).

.

resulting in large amplitude of the baryon acoustic oscillations, which results in a larger first peak of the power spectrum[20]. If the matter density is increased without increasing the baryon density (corresponding to a larger fraction of dark matter), only the gravitational attraction grows, because dark matter does not couple to radiation. Hence, a larger amount of dark matter would dampen the effect from the radiation pressure, resulting in a smaller amplitude for the baryon acoustic oscillations, and thus lower peaks in the power spectrum[20].

The inverse approach can be applied to an observation of the power spectrum of the current universe. The energy densities of the individual components can be determined from precision measurements of the power spectrum. In the cosmological standard model, ΛCDM (which assumes the existence of a cosmological constant and cold dark matter), the energy density is divided between dark energy Λ (responsible for the acceleration of the expansion of the universe), and matter m, currently estimated to be[21]:

$$\begin{aligned} \Omega_\Lambda &= 0.685 \pm 0.013, \\ \Omega_m &= 0.315 \pm 0.013. \end{aligned} \tag{1.2}$$

The matter component can be separated into dark matter (DM) and baryons (b) as:

$$\begin{aligned} \Omega_{\mathrm{DM}} &= 0.264 \pm 0.005, \\ \Omega_b &= 0.049 \pm 0.001. \end{aligned} \tag{1.3}$$

Even though the calculations leading up to these results are assuming a specific model (ΛCDM), the observations are nevertheless consistently rejecting a universe made up of only baryonic matter[22].

1.1.4 Large scale structures

After recombination only the gravitational attraction has affected the matter distribution, and over time this has resulted in the universe today, where there are

empty voids and relatively dense concentrations of matter (filaments). These *large scale structures* can be observed with galaxy maps, e.g. the Sloan Digital Sky Survey[23]. The power spectrum of the two-point correlation function between galaxies (corresponding to the modes of the power spectrum of higher order than the CMB power spectrum) can be predicted from a cosmological model[19]. By measuring the distance between galaxies in large scale structures, the resulting power spectrum provides information about the energy density in the universe (in a similar way as for the investigation of the CMB)[24]. The results from the large scale structure contribute information that break the degeneracies of e.g. Ω_Λ and Ω_m in the CMB results, adding valuable constraints on the cosmological parameters[25, 26].

Through simulations of clustering of dark matter, one can more directly follow the effect of dark matter on the development of large scale structure[27, 28]. By introducing the right amount of dark matter into the simulation, it reproduces the voids and filaments of matter observed in the large scale structure[29]. Most important for the possible dark matter candidates, the simulations demonstrate that relativistic (or hot) dark matter generate too little clustering of galaxies at shorter distances (smaller scales) compared to observation[30]. A possible dark matter particle must be massive enough to be non-relativistic in the early universe, i.e. *cold* dark matter (CDM). On the other hand, simulations with only cold dark matter are in tension with some observations, because they predict too many subclusters of matter within galaxies. This problem can be relieved by a hot dark matter component that has been cooled down (referred to as warm)[31], though it is still a debated topic in the literature.

1.2 Dark matter candidates

The observational evidence of an additional gravitational component in the universe, can be explained by three different classes of ideas: 1) It might be some known component that is unaccounted for in the measurements. 2) Our theories of gravitation might not be correctly describing our universe. 3) New theories beyond that of the Standard Model can describe dark matter by introducing a new particle. As shall be demonstrated in the following, current observations indicate that dark matter cannot be explained with solely the first and second idea.

1.2.1 What dark matter is not

"It is of course possible that luminous plus dark (cold) matter, when combined, give a significantly higher density" (my translation)[3]. With this comment Fritz Zwicky referred to gas, faint galaxies, and intergalactic stars, because he thought they could be constituting the dark matter. The list of candidates for the invisible mass can be further expanded to known objects that are very massive, but very dim, like small black holes, brown dwarfs, etc[22]. Studies of the microlensing (time varying weak lensing) of distant stars by massive compact objects have, however, ruled out the possibility of a significant contribution to the Milky Way galactic halo from compact objects with masses between $10^{-7} - 10$ solar masses[32]. With the measurements of the CMB power spectrum, this strongly constrains the contribution to dark matter from baryonic mass.

Neutrinos constituting dark matter Massive neutrinos will contribute to the matter density in the universe (if they are no longer relativistic), in much the same way as dark matter (e.g. an invisible mass). At least two of the neutrinos described in the Standard Model have a non-zero mass, and all three neutrinos are active (as opposed to sterile, see below), in the sense that they are interacting (weakly) with ordinary matter. A massless neutrino produced in the early universe would have a kinetic energy corresponding to the present temperature of the CMB (T_{CMB})[33], and a neutrino with mass $m_\nu \gg T_{\mathrm{CMB}}$ would be non relativistic. Since the smallest mass difference of the neutrino mass eigenstates $\sqrt{\Delta m^2_{21}} > T_{\mathrm{CMB}}$ at least 2 active neutrinos are no longer relativistic, and will behave like dark matter. With the current estimate of 113 neutrinos/antineutrinos per cm^3 of each flavor, one can write down the following expression for the relative neutrino energy density (assuming all three neutrino flavors are non-relativistic)[34]:

$$\Omega_\nu = \frac{\rho_\nu}{\rho_c} \sim \frac{\sum m_\nu}{93 \text{ eV}}. \tag{1.4}$$

This means that with a measurement of the sum of neutrino masses, the energy density from neutrinos can be determined and compared to the total matter density. The current best limit on the sum of neutrino masses from laboratory measurements of β-decays results in an energy density of neutrinos of $\Omega_\nu < 0.04$. Comparing this to the estimated dark matter density of $\Omega_{\mathrm{DM}} = 0.26$, it follows that neutrinos can only be a subdominant part of dark matter. Further, the masses of the Standard Model neutrinos are too small to constitute cold dark matter[33].

Sterile neutrinos The neutrinos in the Standard Model are all left-handed, and referred to as active neutrinos, because they can interact with other particles via the weak force. Because all other particle in the Standard Model have right-handed counterparts, it is a natural extension to introduce right-handed neutrinos with no interaction with the Standard Model (as the weak force only couple to left-handed particles)[35]. The existence of such a class of *sterile* neutrinos has not been confirmed, but various theories offer properties of the sterile neutrinos that can explain unanswered questions in particle physics. Sterile neutrinos coupled to the oscillation of the active neutrinos has been popular in explaining anomalies in the neutrino oscillation experiments[36]. Depending on the mass of the sterile neutrino, it can also serve as a dark matter candidate if the mass is significantly larger than that of the active neutrinos[37], however the simple scenario of sterile neutrinos constituting all dark matter is not favoured[38].

1.2.2 A dark matter particle

If dark matter cannot be explained by known particles, then an alternative idea is that the apparent additional mass is not missing, but can instead be described by modifying Newton's law of gravity at large scales. The implementation of this idea has been very successful in describing rotation curves of galaxies, however in order to explain the observations of interstellar collisions (or galaxy mergers), the introduction of at least a 2 eV sterile neutrino is needed[39].

1E0657-56 ('The Bullet Cluster') and MACS J0025.4-1222 are galaxy mergers where it has been observed that the gravitational mass moves along with the galax-

ies, whereas the concentrations of gas is slowed down by the interstellar collisions[40, 41]. Abel 520 ('The Train Wreck') was believed to show the opposite result, with a dark matter core residing within the gas concentration[42], as one would expect from dark matter interacting with the gas. But later it was determined that it also exhibit two separated dark matter concentrations as well[43]. Those observations are difficult to explain without the introduction of some invisible matter that has no interaction with the interstellar gas. Since no known particle from the Standard Model is abundant enough, one has to introduce new particles beyond the Standard Model to constitute the invisible matter.

1.2.3 The WIMP candidate for particle dark matter

So dark matter cannot be explained by any combination of particles currently in the Standard Model, but there is enough to choose from in models beyond the Standard Model[22].

From what we know, dark matter must be stable (at least compared to the age of the universe)[44]. Since it is 'dark' it cannot have any electric charge, and because dark matter has been observed to be non-baryonic it can not have a color change which would couple it to baryons.[22]. The observations of galaxy mergers further impose bounds on the interaction of dark matter with itself, which is found to be insignificant[40, 41, 43, 45, 46], though it is still a topic of discussion in the literature[47]. However, it might couple weakly to the Standard Model, as a Weakly Interacting Massive Particle (WIMP), which will be the focus of this thesis. The existence of WIMPs are motivated in multiple theories, here two popular candidates can be mentioned.

In the SUperSYmmetric (SUSY) extension to the Standard Model, each boson in the Standard Model gets a fermionic super-partner and the fermions get a bosonic super-partner. SUSY introduces many additional parameters for the extra particles, which is reduced in the Minimal Supersymmetric Standard Model (MSSM)[22]. MSSM introduces the quantum number of R-parity for all particles, such that the Standard Model particles have an R-parity of $+1$, and the supersymmetric particles have an R-parity of -1. Under the assumption of conservation of R-parity, the lightest supersymmetric particle (LSP) must be stable, and represent a good candidate for dark matter. The only way the LSP could be destroyed is via annihilation of a pair of LSPs (or *self-annihilation*), which would produce a signal of Standard Model particles.

In the extension to the Standard Model of Universal Extra Dimensions (UEDs), each Standard Model particle field can propagate in additional dimensions to produce higher order modes or *Kaluza-Klein* states[48]. The lightest Kaluza-Klein (LKP) state of the neutrino would be a stable particle with a mass below 1 TeV, which would be another attractive candidate for dark matter[22].

In the early universe, the WIMP number density n was governed by the rate of annihilation and creation of WIMPs and a thermodynamic equilibrium would be reached (if the concentration of WIMPs was high enough). The annihilation rate Γ, must be proportional to the annihilation cross-section σ, and the velocity of the WIMPs v[49]:

$$\Gamma = n\sigma v. \tag{1.5}$$

Since the velocity of the individual WIMPs are not known, only the velocity averaged product of the WIMP self annihilation and velocity ($\langle\sigma v\rangle$) can be determined from a given rate of WIMP annihilations. Assuming that the WIMP is the only particle beyond the Standard Model (or that all other particles that might be created in the early universe promptly decay to the WIMP) we can write the Boltzmann equation for the evolution of the WIMP particle density as[50]:

$$\frac{\mathrm{d}n}{\mathrm{d}t} = -3Hn - \langle\sigma v\rangle\left(n^2 - n_{\mathrm{eq}}^2\right) \tag{1.6}$$

Here the first term is diluting the density along with the expansion of the universe with the Hubble constant H, and the second term refers to the annihilation or production of WIMPs to, or from, Standard Model particles (towards the number density at equilibrium n_{eq})[51]. As the universe cools, the production rate will drop, and as the universe expands the annihilation rate will drop.

When the thermal equilibrium can no longer be maintained, the WIMPs *freeze-out*, and the comoving density stays constant (i.e. the number density decreases only with the expansion of the universe[52]), and the WIMP is described as a *thermal relic*. In this simple picture, the Boltzmann equation of Eq. (1.6) can be solved and provide an order of magnitude estimation for the relation between the relic abundance and $\langle\sigma v\rangle$[53]:

$$\Omega_{\mathrm{DM}}h^2 \sim \frac{3\cdot 10^{-27}\mathrm{cm}^3\mathrm{s}^{-1}}{\langle\sigma v\rangle}. \tag{1.7}$$

With the current estimate for the energy density of dark matter of $\Omega_{\mathrm{DM}} = 0.26$, the value of the velocity averaged product of the annihilation cross section and the relative velocity should be at the '*natural scale*' of $\langle\sigma v\rangle \sim 10^{-27}\mathrm{cm}^{-3}\mathrm{s}^1$ (depending on WIMP mass[54]).

One can (from dimensional analysis) determine that $\langle\sigma v\rangle \sim g_{\mathrm{DM}}^4/m_{\mathrm{DM}}^2$[55], which has inspired the search for a 100-1000 GeV particle with a coupling, g_{DM}, similar to the weak force. This obviously makes the WIMP a popular candidate for dark matter, though the natural scale value of $\langle\sigma v\rangle$ can also be achieved with other combinations of coupling strength and masses[56], like e.g. the strongly interacting massive particles (SIMPs)[57].

The mass of the WIMP is somewhat bounded ($0.1\ \mathrm{eV} \ll m_{\mathrm{DM}} < 120\ \mathrm{TeV}$) at higher mass by a unitarity constraint on WIMP annihilation[58], and from lower mass if it is to be a cold relic[59]. However, the strength of the annihilation cross section also determines when freeze out happens. If the annihilation cross section is large, the WIMP stays in equilibrium longer, hence it might freeze out after the temperature is much lower than the mass of the WIMP, and would constitute cold dark matter. If the WIMP mass is very low, the temperature will most probably always be larger than the WIMP mass at freeze out, and the WIMP would constitute hot dark matter.

The WIMP is an exciting candidate to look for. If it self-annihilates and has a significant coupling to the Standard Model, it can produce a signal that can be detected. If the coupling to the Standard Model is too weak it might not be possible to investigate, and it would constitute a *hidden sector* that we might never learn more about. This is an open invitation to go and look for the WIMP, and that shall be the exclusive dark matter candidate considered in this work.

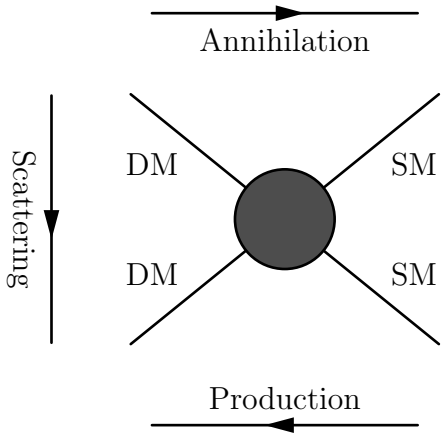

Figure 1.3: Popular representation of three ways to search for WIMPs, given that it can interact with Standard Model particles.

1.3 Detection techniques

Following the schematic of Figure 1.3, the current WIMP searches are trying to detect/measure WIMPs either annihilating to, scattering on, or being produced from Standard Model particles. For completeness, a brief overview of the general assumptions and approaches of current dark matter detection strategies shall here be presented. With the focus in this work on the indirect search of neutrinos from dark matter annihilations in the galactic halo, more details on the expected signal shall be described in the following sections.

1.3.1 Direct detection

As the Earth moves around the Sun it passes through the dark matter halo of the Milky Way, and if the halo is indeed composed of WIMPs, they will have a chance of scattering off of ordinary matter. When the WIMPs scatter directly off of a nuclei, the nuclei will recoil, which can be detected as a production of e.g. heat, ionization, and/or scintillation light. The expected rate for such a *direct detection* is determined by the WIMP number density, velocity relative to the Earth, and the WIMP-nucleon scattering cross section. Of those, only the WIMP-nucleon scattering cross section is unknown and unbounded, and is categorized into either a spin-dependent or spin-independent scattering cross section. The spin-dependent scattering σ_{SD} is proportional to the total spin J of the nucleus and is constant with larger atomic mass, whereas the spin-independent scattering cross section σ_{SI} grows with larger atomic mass[22]. Further, some kind of inelastic scattering where the WIMP excites the electrons in the atoms could also lead to a detection[60]. Not knowing more about the WIMP-nucleon interaction, all of these ideas are being investigated.

There is a range of experimental results from detectors measuring on recoils in either crystals or liquids. At the time of writing, there are excesses observed from DAMA[61], CoGeNT[62] (though later disputed[63]), CDMS-II (Si)[64] (but not in CDMS-II (Ge)[65]), and CRESST-II[66], while other experiments have not observed any signal, and have instead resulted in limits as seen from Figure 1.4. Depending on which models are used to describe the interaction between ordinary matter and

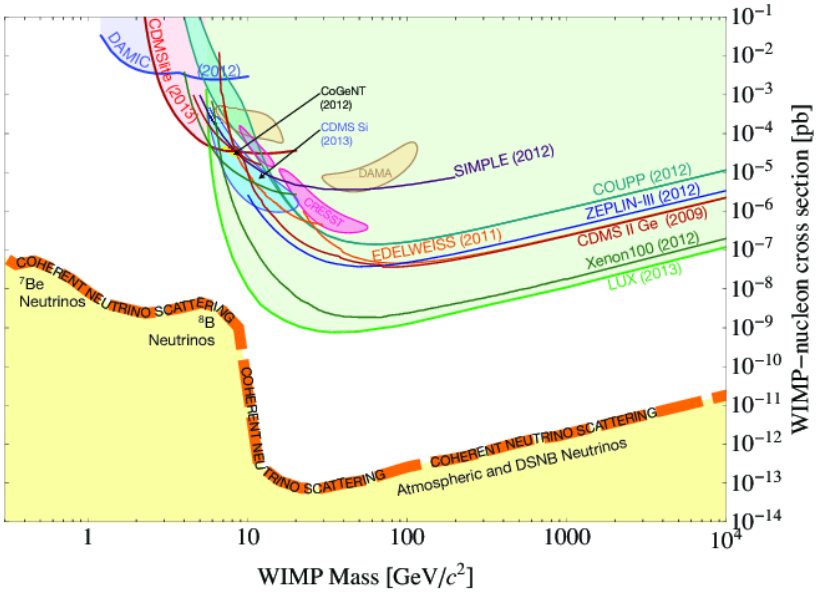

Figure 1.4: Plot of the gloabl limits by direct detection experiment, showing the conservative level at which coherent neutrino scattering becomes a significant problem (from [68]).

dark matter, some of the current claims are still not ruled out[67]. At the time of writing there is no strong evidence favoring one dark matter model over the other.

Assuming that the current excesses are not caused by WIMP-nucleon interactions, the explorations continue towards lower values for the WIMP-nucleon cross section. However, at some point the experiments will reach an irreducible background from coherent neutrino-nucleus scattering of low energy neutrinos produced in the Sun[69]. As these will begin to be detected in the experiments[70, 71, 68] it will be a considerable challenge for the direct dark matter searches, but it will also provide more information about the solar neutrinos.

1.3.2 Direct production

With the high energy available in the proton collisions at LHC, it should be possible to produce WIMPs (depending on the theoretical coupling to standard model). Various types of effective models (and more recently the simplified models[72]) are used to systematically classify all the possible interactions between WIMPs and quarks/gluons. Having experiments built to be hermetically closed (at least around the beam axis), means that the missing energy transverse to the beam axis can be determined. Because missing transverse energy is a signature of neutral particles leaving the detector, e.g. a stable dark matter particle like the WIMP, this is the dominant strategy for collider probes of dark matter. Neutrinos produced in various Standard Model processes constitute the main background to such a signal, and no significant deviations from the Standard Model has yet been observed[49, 73].

The limits on the cross section for a given model can be translated into a WIMP-nucleon scattering or WIMP annihilation cross section, but it is strongly dependent on the choice of the parameters governing the intermediate particles[74, 75].

1.3.3 Indirect detection

In the event that WIMPs can self-annihilate or decay to Standard Model particles, an *indirect detection* of WIMPs can be made by looking for an elevated flux of particles from astrophysical objects with large concentrations of dark matter. That might be the Sun, galaxies, or galaxy clusters. Dwarf galaxies have a high mass-to-light ratio, so the dark matter content can be estimated relatively accurately, due to a lower light emission foreground. The precise distribution of dark matter in galaxies are currently under discussion (as will be presented in Section 1.4), and the difference becomes more apparent for extended sources, affecting the searches for WIMP annihilations or decays in our own galaxy more than dwarf galaxies. However, the signal from the Milky Way will be much stronger as the Earth is completely engulfed in the dark matter halo, and much closer to the strong signal expected from the center of our own galaxy.

Through the annihilation or decay of the WIMPs, any pair of Standard Model particles might be produced. Depending on the detector/telescope, one can look for a specific particle produced directly in the annihilation or in the subsequent decay chain.

Due to the proliferation of precision astronomy and astrophysics telescopes (both ground and space-based), WIMP annihilation or decay to photons is an opportunistic channel. Satellite missions aim at detecting photons in the energy range of keV (X-ray) to GeV (γ-ray). Ground-based detectors use telescope dishes to look for cosmic photons at various energies from radio waves to Cherenkov radiation from charged particles in the atmosphere induced by high energy cosmic photons. WIMPs annihilating to photons will produce distinct line spectra at the mass of the WIMP, and the detection and confirmation of such a line would be a strong signal of WIMPs. The observation of an excess from the center of the Milky Way around 1-4 GeV seen in data from Fermi telescope is one of many interesting observations that is still unresolved[76]. The ground Cherenkov telescope MAGIC has not observed any excess and provide some of the strongest limits on WIMP annihilations from photons[77].

Even though the charged cosmic rays do not point back to their origin, space-based experiments like PAMELA[78] and AMS-02[79] can search for dark matter in the energy distribution of e.g. positrons. The positron fraction is expected to decrease at higher energies, so the current observations of the fraction flattening out can be interpreted as signal from dark matter annihilations or decay.

WIMPs might also annihilate into neutrinos, which are electrically neutral and their direction is thus only affected by gravitational potentials, and neutrinos also scatter less than photons as they propagate through the interstellar medium. When the neutrinos from WIMP annihilations gets detected at the Earth they will mainly point directly back to their origin. In order to detect the neutrinos large Cherenkov detection experiments like Super-Kamiokande[80], ANTARES[81] or IceCube[82] are used. This work presents the analysis of 3 years of IceCube data searching for signal from WIMP annihilations. In the following sections, the distribution of dark matter in the Milky Way, and the expected flux of neutrinos from the WIMP annihilations shall be discussed.

The search for a neutrino signal from WIMP annihilation further adds the unique possibility to look for WIMPs annihilating directly into neutrinos.

Solar WIMP search The closest significant accumulation of WIMPs happens in the Sun. In the same way as for direct detection considerations, the WIMPs might scatter off the nucleons in the Sun, lose momentum, and thereby get trapped in the gravitational potential of the Sun. Moving through the galactic dark matter halo, the Sun can thereby accumulate WIMPs. In turn this means that an indirect search of WIMP annihilation in the Sun, probes the WIMP-nucleon cross section, and not the annihilation cross section. In this way such indirect searches compete with the direct searches, and are also less sensitive to possible isospin violations in the WIMP-nucleon scattering[83].

1.4 Dark matter distributions in the Milky way

The focus of this thesis is on dark matter in our own galaxy, and hence the dark matter distribution will be important. Generally, galaxies are modelled with a simplified approach containing a luminous central bulge, a luminous flat disk, and a spherically symmetric dark matter halo. There might be subclusters and other irregularities in the spherical halo, but they are assumed to be small enough to be within the uncertainties on the models[84].

In this work two different models shall be considered; the Navarro, Frenk, and White (NFW) profile[85, 86] and the Burkert profile[87]. Early N-body simulations of clustering of cold dark matter showed that they all generated halos with a universal density profile. The density of the dark matter is modeled with a logarithmically changing slope in the NFW profile,

$$\rho(r)_{\mathrm{NFW}} = \frac{\rho_0}{r/R_H\,(1 + r/R_H)^2}. \tag{1.8}$$

Here the scale radius R_H represents the slope change, and the density scale ρ_0 sets the overall density. The NFW profile is very successful in describing both the outer and inner parts of the simulated halos[88]. It is designed to have the densities diverging for the central regions[86], which is in contrast with other models that describe more constant densities near the core.

Observations of low brightness galaxies serve as good comparisons to the simulations, as the low brightness is due to the baryonic matter not having formed as stars, and the galaxies are dominated by dark matter. The NFW profile does not provide a good fit for the density of low brightness galaxies, and e.g. overestimates the central density[89]. As an alternative the Burkert profile provides another phenomenological model, which instead has a finite central density; effectively a much wider core region with a constant density. It matches the NFW profile at high radii and is also parametrized with a scale radius R_H and density scale ρ_0:

$$\rho(r)_{\mathrm{Burkert}} = \frac{\rho_0}{(1 + r/R_H)\,(1 + (r/R_H)^2)}. \tag{1.9}$$

Which profile correctly describe a universal dark matter halo profile strongly depends on the sample of galaxies chosen (observation or simulation), and there is a long list of halo profiles under discussion in the literature[90]. This work shall focus on only the NFW and Burkert profiles, as most other popular halo models lie somewhere in between the two.

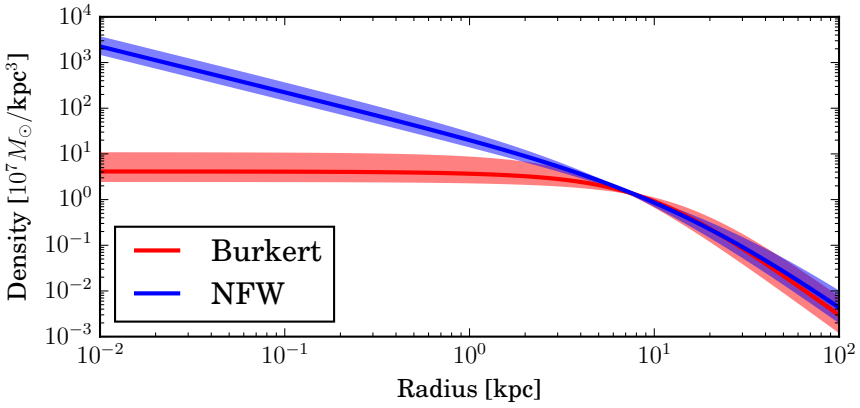

Figure 1.5: The dark matter halo density in the Milky Way, according to the two models considered in this work. The bands show the 1σ uncertainty bands (based on Ref. [84]).

A fit of the profiles to a given dataset is needed in order to establish the values of the density scale and scale radius. In this work the results of Ref. [84] shall be used, in which the author used observations of e.g. extra bright stars and gas clouds within the Milky Way. Ref. [84] further concluded that the Burkert profile is preferred, but fits of both profiles shall be considered here, using the parameters of the fit shown in Table 1.1. As illustrated on Figure 1.5 the NFW profile has a much denser center, whereas the Burkert profile is somewhat more uniform, with a lower density in the center.

Table 1.1: Parameters for the NFW and Burkert halo profiles fit to the Milky Way presented in Ref. [84].

	$\rho_0[10^7 M_\odot/kpc^3]$	R_H [kpc]
NFW	$1.4^{+2.9}_{-0.93}$	$16.1^{+17.}_{-7.8}$
Burkert	$4.13^{+6.2}_{-1.6}$	$9.26^{+5.6}_{-4.2}$

1.5 Neutrino signal from dark matter annihilation

As WIMPs annihilate in the Milky Way, they may produce any pair of Standard Model particles; leptons, quarks, or bosons. The quarks and bosons will decay to leptons and/or lighter quarks. Taus and muons will decay to lighter leptons that will eventually produce neutrinos. The light quarks hadronize and produce mesons, that subsequently decay to leptons or photons. Depending on the annihilation channel and decay chain, a number of neutrinos will be produced, propagate to Earth, and can be detected in neutrino observatories.

Going back to the annihilation rate in Eq. (1.5), the flux of neutrinos from the WIMP annihilations is proportional to the thermally averaged product of the WIMP annihilation cross-section and relative velocity $\langle \sigma v \rangle$, and the WIMP density

$n_{\mathrm{DM}} = \rho_{\mathrm{DM}}/m_{\mathrm{DM}}$. The differential flux of neutrinos from WIMP annihilations is given as a function of the included arrival directions of neutrinos, described by the opening angle Ψ, of a cone pointing away from Earth:

$$\frac{d\Phi}{dE_\nu}(\Psi) = \frac{1}{4\pi}\frac{\langle\sigma v\rangle}{2m_{\mathrm{DM}}^2}\frac{dN}{dE_\nu}\int_{\mathrm{los}}\rho_{\mathrm{DM}}^2(r(l,\Psi))dl. \tag{1.10}$$

The spherically uniform production of neutrinos is taken into account by normalising with a 4π solid angle, and the factor of $1/2$ is introduced since two WIMPs are annihilating. The line-of-sight (los) integral of $\rho_{\mathrm{DM}}(r)$ in Eq. (1.10) is calculated along a line l through the dark matter halo of density, so the the radial dependence of the density is calculated in terms of l and Ψ as[91]:

$$r(l,\Psi) = \sqrt{R_\odot^2 - 2lR_\odot\cos\Psi + l^2}. \tag{1.11}$$

Here $R_\odot \approx 8$ kpc indicates the radius of the Sun's orbit in the Milky Way. The integral should cover the full halo, but for the numerical calculation it is truncated at $R_{\mathrm{halo}} = 50$ kpc, outside of which the halo no longer significantly contributes to the signal, as seen on Figure 1.5. The integration limit l_{max}, is then determined as[91]

$$l_{\mathrm{max}} = \sqrt{R_{\mathrm{halo}}^2 - R_\odot\sin^2\Psi} + R_\odot\cos\Psi. \tag{1.12}$$

In order to have a non-divergent line-of-sight integral for the otherwise divergent NFW profile, a flat density is used for the central core within $r < 0.0015$ kpc, following the approach of previous analyses[92].

The energy distribution of neutrinos from the decay chain dN/dE_ν in Eq. (1.10) will be dependent on the annihilation channel and WIMP mass m_{DM}. For a given WIMP annihilation model the energy distribution will be a sum over all the possible annihilation channels, with associated branching ratios. However, in this work, no specific WIMP annihilation models shall be tested, and instead a 100% branching ratio into one of five different annihilation channels shall be tested. The channels considered are annihilation through $b\bar{b}$, W^+W^-, $\mu^+\mu^-$, $\tau^+\tau^-$, or annihilation directly to $\nu\bar{\nu}$. Any admixture of branching ratios will then be bounded by at least one of the 100% branching ratio scenarios.

In Figure 1.6 an example of the energy distribution of muon neutrinos from various annihilation channels is shown. The energy distributions used in this work are produced using the PYTHIA[93] event generator, where a generic particle with mass $2m_{\mathrm{DM}}$ is forced to decay to either of the considered annihilation channels. This emulates the non-relativistic dark matter annihilation through a mediator to Standard Model particles. Annihilation straight to neutrinos produce a perfect line spectrum, however, in order to be consistent with the use of the simulated datasets, the line spectrum of the neutrinos has been smeared out with a Gaussian with a width of 5% of the WIMP mass. This will not have a significant effect on the results in this work, as the neutrino energy is not used in the analysis presented in this work.

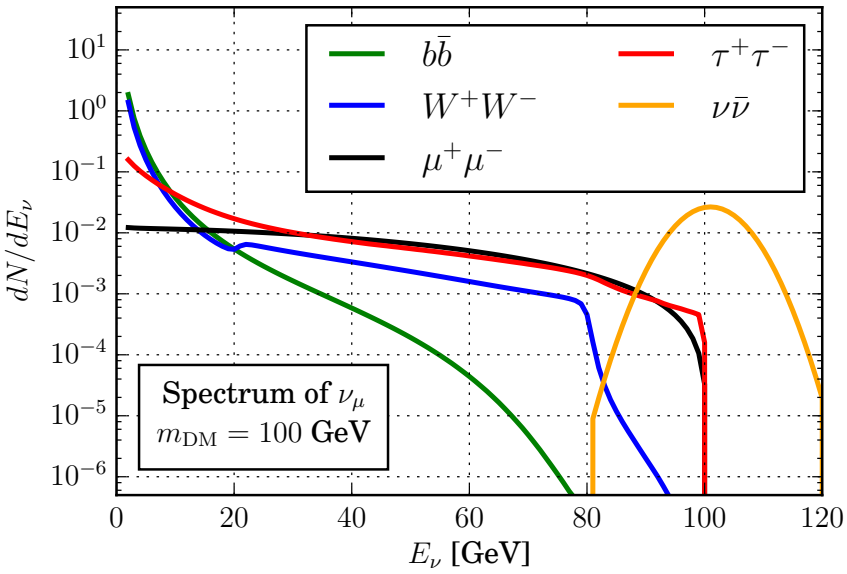

Figure 1.6: The differential distribution of muon neutrinos from the annihilation of a 100 GeV WIMP, through five benchmark annihilation channels assuming a 100% branching ratio. The distributions are determined using particle annihilations in PYTHIA, however the line spectrum of the annihilation directly to neutrinos has been broadened by a gaussian with a width of 5% of the mass of the WIMP.

2

Neutrino astrophysics and matter interaction

The neutrino is electrically neutral, hence its path is not bent in interstellar magnetic fields. This means that it points back to it origin and can be used as a messenger particle to study astrophysics. The field of neutrino astrophysics is relatively young, but has gained interest since it offers a different approach to the information compared to what can be inferred from conventional astronomy using the photon as the messenger particle. As the neutrino only interacts weakly, the scattering and absorption is a negligible issue compared to photons and cosmic ray messengers. This also poses the extreme challenge of detecting the neutrinos, which requires either an immense flux (achievable from particle accelerators) or very large target masses (with which the neutrino interact).

When looking for a neutrino signal from WIMP annihilation in the Milky Way, the flux cannot be changed and hence the detection depends on extremely large detectors, like the IceCube Neutrino Observatory. In order to utilize the detector, an understanding of the properties of the neutrino and details of the neutrino interaction with matter is important. This shall be covered in this chapter before covering the detection of the interacting neutrinos in the following chapter. In any neutrino observatory, a rate of neutrinos (and muons) from other sources will also be present. They pose a background for the search of neutrinos from WIMP annihilations in the Milky Way, which shall be discussed at the end of this chapter.

2.1 Neutrino oscillations

It was once a problem that experiments on Earth measured only one third of the rate of neutrinos from the Sun, compared to the expectation from the solar model of nuclear reactions[94]. We now know that it is due to *neutrino oscillations*, i.e. neutrinos transforming between the three flavor states, electron, muon and tau[95]

Neutrino oscillations are described quantum mechanically as a mix of flavor states ν_f, which are linear combinations of the mass eigenstates ν_i, defined by the mixing elements U_{fi}, of the Pontecorvo-Maki-Nakagawa-Sakata (PMNS) matrix[96, 97].

$$\nu_f = \sum_{i=1}^{3} U_{fi}^{\mathrm{PMNS}} \nu_i \tag{2.1}$$

The mixing is normally parametrized by 3 mixing angles θ_{12}, θ_{23}, and θ_{13} and a phase δ_{CP} related to the charge-parity violation of neutrinos.

If one considers the two neutrino flavor case of ν_α and ν_β, one can arrive at the following expression for the probability of a neutrino with energy E, transforming to the other type after propagating a distance L[35]:

$$P_{\nu_\alpha \to \nu_\beta} = \sin^2(2\theta) \sin^2 \left(\frac{(m_2^2 - m_1^2)c^3}{4\hbar} \frac{L}{E} \right) \tag{2.2}$$

where m_i is the mass of neutrino mass eigenstate i, and θ is the mixing parameter parametrizing the corresponding 2×2 mixing matrix. Here neutrinos have been considered to have relativistic momentum (compared to their mass), and the approximation of $L = ct$ has been made.

For neutrinos travelling galactic distances the propagation distance is no longer well-defined and must be averaged out, so the second sine-function of Eq. (2.2) disappear. This is referred to as *long baseline neutrino oscillations* for which the neutrino flavor ratio at Earth $\nu_{f_\odot}$ can be calculated from the flavor ratio at the source ν_{f_S} by transporting it to Earth with the PMNS matrix.

$$\{\nu_f\}_\odot = U^{\text{PMNS}} \{\nu_f\}_S \tag{2.3}$$

The long baseline neutrino oscillations will be applied to the signal neutrinos from WIMP annihilations in the galactic halo, since they will be produced all through the galactic halo.

2.1.1 Neutrino mass

As can been seen from Eq. (2.2) apart from a mixing parameter, neutrinos also need a mass difference in the mass eigenstates for oscillations to occur. With the three active flavors present in our universe, it indicates that at least two of the neutrino mass eigenstates must be non-zero. The mass differences can be parameterized in terms of $\Delta m_{21}^2 = m_2^2 - m_1^2 \approx 7.5 \cdot 10^{-5}$ eV^2 and $\Delta m_{31}^2 = m_3^2 - m_1^2 \approx 2.45 \cdot 10^{-3}$ eV^2 [98]. The values illustrate that the neutrino masses are all close to each other relative to the mass of all other Standard Model particles.

The absolute mass of the electron neutrino can be determined from precise β-decay measurements, as a non-zero mass will affect the endpoint of the decay energy spectrum. At the high energy tail of the spectrum there is a limit to how much energy the electron can carry away if the associated neutrino has mass. The difference between the decay endpoint and the energy available in the decay, can be attributed to the mass of the electron neutrino[99], with the current best limit being $m_{\nu_e} \leq 2.05$ eV[100].

In a similar way the possibility of a Majorana mass term in the description of neutrinos can be probed in double β-decay experiments, looking for events where the two neutrinos annihilate, and the energy of the two electrons will be at the end point. This is an ongoing search, where next phase experiments will either be discovering, or ruling out, neutrino Majorana masses for the inverted mass ordering[101].

The combined mass of all three flavors of neutrinos can be probed by cosmological observations. Because neutrinos have mass they affect the baryon acoustic oscillations in the early universe (the result of which is imprinted on the CMB) as well as the evolution of large scale structures. Even though the effect is small and degenerate with other cosmological parameters[102], there is some sensitivity

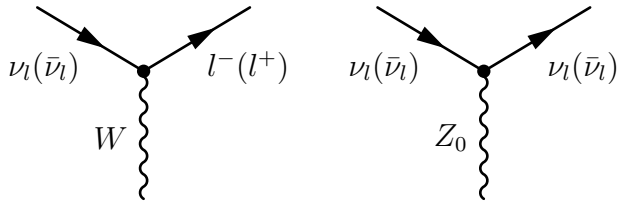

Figure 2.1: The two fundamental vertices in neutrino interactions illustrated for neutrinos (antineutrinos). The charged (neutral) current interaction vertex is shown on the left (right) of a neutrino with flavor l.

to the neutrino mass sum. The Planck mission set a limit of $\sum m_\nu < 0.59$ eV (using less conservative techniques, e.g. lensing corrections, they can push it down to 0.14 eV)[103]. Combining multiple observables it is possible to arrive at even stronger bounds of $\sum_i m_i < 0.12$ eV by using the Lyman-α forest from the Sloan Digital Sky Survey dataset[104]. However, cosmologically derived bounds become more and more dependent on observation techniques, model assumption, and its given parameter space[105].

2.2 Neutrino interactions

As the existence of neutrinos can only be detected through their interaction with matter, the details of neutrino interactions shall here be presented. They will assume the neutrino, but will also cover the case of anti-neutrinos (unless explicitly mentioned). Neutrinos in the Standard Model interact by the two vertices presented in Figure 2.1. Either transforming to a charged lepton with similar flavor and parity in a *charged-current* (CC) interaction with a W boson, or by emitting/absorbing a Z boson in a *neutral-current* (NC) interaction.

These basic vertices translate into a number of different interactions with matter, depending on the energy of the neutrino, shown in the left panel of Figure 2.2. Quasi-elastic (QE) interactions with the entire nucleus as a whole where a single (or only a few) nucleons are liberated in the neutrino interaction. Resonance production (RES) of various baryons (mainly pions), where the target nucleus decays after getting excited to a resonant state by the interaction with the neutrino. In addition, one can also classify coherent pion production, where the pion is produced directly in the interaction. Above 100 GeV most of the interactions will be Deep Inelastic Scattering (DIS), where the neutrino interacts with the individual constituent quarks and gluons of the nucleons[106]. In the elastic scattering of neutrinos off of nuclei, the nuclei experience a recoil that can be detected in some neutrino experiments, but not in IceCube. Interactions with the bound electrons are negligible compared to neutrino-nucleus interactions and the enhanced W-boson resonance (of $\bar{\nu}_e + e^- \rightarrow W^-$), is only relevant for anti-electron neutrinos with PeV scale energies[107].

In the right panel of Figure 2.2 the expected distribution of muon neutrino interactions from a 300 GeV WIMP annihilating through W^+W^- (assuming $\langle \sigma v \rangle = 10^{-19}\text{cm}^3/\text{s}$). It is a stacked histogram of the different types of interactions at the next to final level of event selection for the analysis presented in this work. The

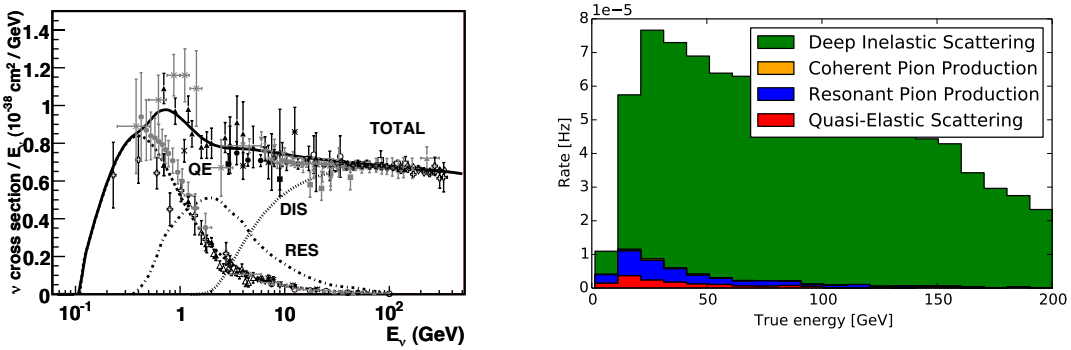

Figure 2.2: Left: The different components of the muon neutrino charged-current interaction with an iso-spin atomic target as a function of energy (from [106]). Right: The different components present at the next to final event selection level of the analysis presented later in this work.

distributions match the expectation from the cross-section estimates, maybe with a slight preference for DIS (as that will generally produce more charged particles and hence more light).

2.2.1 Fate of interaction products

Effectively, neutrino interactions result in a shower of daughter particles from the struck nuclei and/or the production of a charged lepton with the same flavor as the incoming neutrino. Depending on energy losses of the interaction products as they propagate through the interaction medium (which shall here be assumed to be ice), a different amount of information about the neutrino can be extracted.

Hadrons propagating through matter lose their energy through *hadronic showers*, mainly through the production of pions[108]. The hadronic shower produced in or initiated by ejected particles in the neutrino interaction loses it's energy within a few interaction lengths[109], which for ice corresponds to a few meters.

A produced electron mainly loses energy through *electromagnetic cascades*, with an alternating production of photons (through bremsstrahlung) and electron-positron pair production (by the photons)[108]. The depth at which the shower reaches it's maximum number of particles is logarithmic in energy, after which it diminishes exponentially[109]. The majority of the electromagnetic cascade will be contained within 4 times the depth at shower maximum[110, 108], which for ice corresponds to at most 5 meters for an electron with an energy of 1 TeV. Tau particles have relatively short lifetimes which will be time dilated depending on their energy. At the energies considered (1-1000 GeV) the shower initiated by the decay of the tau happens before the hadronic shower from the hit nuclei dies out and they can therefore not be distinguished (and only above about 1 PeV, the separation becomes significant). If a muon is produced in the tau decay, it will share the characteristics of the charged-current muon neutrino interaction.

Due to the mass of the muon, it only starts losing significant energy to bremsstrahlung at energies 1 TeV (whereas for electrons it starts at about 80 MeV). At a few hundred GeV the muon is minimum ionizing and loses only about 30 GeV per 100 meters travelled through ice[95]. This means that muons will travel many hundred

meters through the ice before losing enough energy to stop and decay, and the muon will therefore spatially separate itself significantly from the hadronic cascade (depending on energy).

2.2.2 Properties of the interaction products

The energy of the muon neutrino in charged-current interactions is deposited into a hadronic cascade and a muon propagating out of the cascade. For the two other charged-current interactions (electron and tau), the lepton travels relatively short distance within the hadronic cascade. In all neutral-current interactions the energy delivered by the neutrino is deposited in the hadronic cascade.

This makes the interactions with no muons more likely to be contained within a detector, making it easier to estimate the energy of the neutrino. For muon neutrino charged-current interactions, the muon might leave the detection volume before decaying, resulting in an incomplete measure of the energy. However, by detecting the energy losses over a longer distance, it is easier to determine the direction of muon compared to the relatively short distance the other leptons travel.

The analysis of this work will depend on the reconstruction of the arrival direction of the neutrino which will be limited by the intrinsic uncertainty of the space angle between the incoming neutrino and the outgoing lepton. In the charged-current interaction, the average space angle difference is approximated to be[95]

$$\langle \theta_{\nu l} \rangle \approx \frac{1.5^\circ}{\sqrt{E_\nu \ [\mathrm{TeV}]}}. \tag{2.4}$$

Since only the charged leptons can be reconstructed, the distribution of signal will be smeared out by the space angle difference of Eq. (2.4). However, for most cases it will be smaller than the resolution on the reconstruction of the lepton.

2.3 Cherenkov radiation

When a charged particle moves through a dielectric medium with a speed higher than the phase speed of light in the medium it will emit *Cherenkov radiation*[111, 112]. The first observations of the effect were reported in 1934 by Pavel Cherenkov[113], and the effect was explained theoretically by Ilya Frank and Igor Tamm[114], predicting the number of photons created in the process from classical electrodynamics. They could conclude that the observations possible at the time by Cherenkov[115] were in the *"best possible agreement with the theory"*[114].

When a charged particle traverses a dielectric medium with refractive index n, the electric field of the charged particle will polarize atoms in the medium, because the electric field of the traversing particle will displace the nucleus from the electrons, causing the atom to get a tiny dipole moment[116]. The electromagnetic disruption of the medium caused by the polarization, propagates with the phase speed of light in that medium c/n[108]. If the particle is moving with a speed $v < c/n$, the disturbance propagates through the medium faster than the particle moves, and an observer far from the particle will see all the electromagnetic waves arriving with a small shift in their phase, effectively cancelling out the contributions by destructive interference. This is illustrated on the left panel of Figure 2.3.

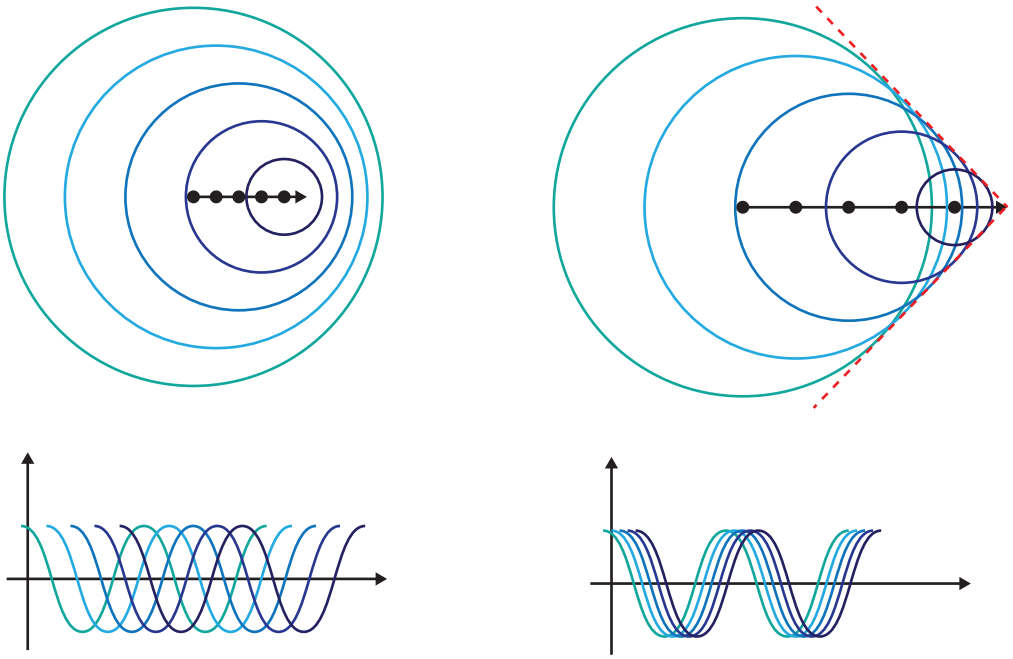

Figure 2.3: Illustration of the propagation of an electromagnetic disturbance in a dielectric medium caused by the polarization and subsequent depolarization of the material from a charged particle. Below, the electromagnetic wave in the medium at a specific point in space is illustrated. The situation is shown for different criteria of the speed v of the charged particle. Left: For $v < c/n$ where the disturbance is cancelling out. Right: For $v > c/n$ the disturbance interferes constructively along the dashed red line, effectively producing a plane wave in a cone around the track.

In the case where the charged particle moves with $v > c/n$, the individual electromagnetic disturbances interfere constructively (indicated on the snapshot on the right panel of Figure 2.3), effectively generating a plane wavefront.

The angle θ_C of the wavefront (or surface of the cone in 3D) to the propagation direction can be determined from the speed of the particle and the refractive index of the medium by comparing the distance traversed by the particle and photons in some time t:

$$\cos(\theta_C) = \frac{\frac{c}{n} \cdot t}{v \cdot t} = \frac{c}{nv}. \tag{2.5}$$

The index of refraction n in a dispersive medium (like ice) is dependent on the frequency ω of the light, which is accommodated in the equations by the simple substitution of $n \to n(\omega)$[116].

The energy threshold at which a particle produces Cherenkov photons depends on the mass of the particle. The relativistic energy of a particle is $E = \gamma mc^2$, and it's kinetic energy can be found as $E_{\text{kin}} = E - mc^2$. Remembering the formulation of the relativistic γ-factor, one can find that[108]:

$$\frac{v}{c} = \sqrt{1 - \left(\frac{mc^2}{E}\right)^2}. \tag{2.6}$$

So in order for a particle to have $v \geq c/n$ it needs a minimal energy of

$$E_{\text{kin,threshold}} = mc^2 \left(\sqrt{\frac{n^2}{n^2 - 1}} \right). \tag{2.7}$$

The threshold energy is hence dependent on the mass of the given particle, such that an electron (muon) will need to have a kinetic energy of at least 0.27 (56.2) MeV to produce Cherenkov radiation in ice at a wavelength of 400 nm where $n_{\text{ice}}(400 \text{ nm}) = 1.32$[95]. Compared to energy losses of charged particles from ionization and radiative losses of e.g. bremsstrahlung, the Cherenkov radiation can be regarded as non-destructive[109].

2.3.1 Cherenkov photon count

The Cherenkov photons are emitted over a large range of wavelengths, increasing in intensity with energy, with about 50% higher intensity for blue light (413 nm) than red (620 nm)[108]. In the approximation where the travel distance L is much larger than the wavelength λ of the Cherenkov photons considered, the number of photons emitted N can be determined from[117]:

$$\frac{dN}{d\lambda} = \frac{2\pi\alpha}{\lambda^2} L \sin^2 \theta_C \qquad L \gg \lambda, \tag{2.8}$$

where α is the fine structure constant. From integrating Eq. (2.8) for $\lambda \in [350; 600]$ nm (the sensitive range of IceCube, details in Section 3.3.1), one can expect a few thousand photons for each centimeter a charged particle moves through ice (with a kinetic energy above the Cherenkov threshold)

Imagine that the same number of photons are propagating away from a point along the track of the charged particle in a uniform sphere. A light sensor with an active surface area of 0.1 m^2 (slightly smaller than in IceCube) located 50 meters away will receive an average of a few photons for each meter of particle propagation. Hence it should be possible to detect the presence of e.g. a muon if it is closer to a light sensor than 50 meters and/or propagates longer than one meter. It will be discussed in the following chapter, that the situation is more complex in IceCube, since one needs to factor in the absorption and scattering of the photons as they propagate through the ice, and the limited detection efficiency of the light sensor.

2.3.2 Cherenkov radiation from secondaries

In most neutrino interactions multiple particles are created. All charged particles that move through the ice will produce light if their energy is above the Cherenkov threshold, however the production of Cherenkov photons is the same at all energies. The average number of particles produced in the hadronic cascade from a DIS interaction increases with the energy of the neutrino. A muon with higher energy has a larger probability for radiative energy losses, and electrons with more energy produce an electromagnetic cascades with more electron-positron pairs[118]. Since each of the secondary particles that has sufficient energy will also produce Cherenkov radiation, more energetic neutrinos will end up producing more light. For a muon with an energy of 100 (1000) GeV, the total Cherenkov radiation will be increased by about 50% (250%) due to secondaries[118].

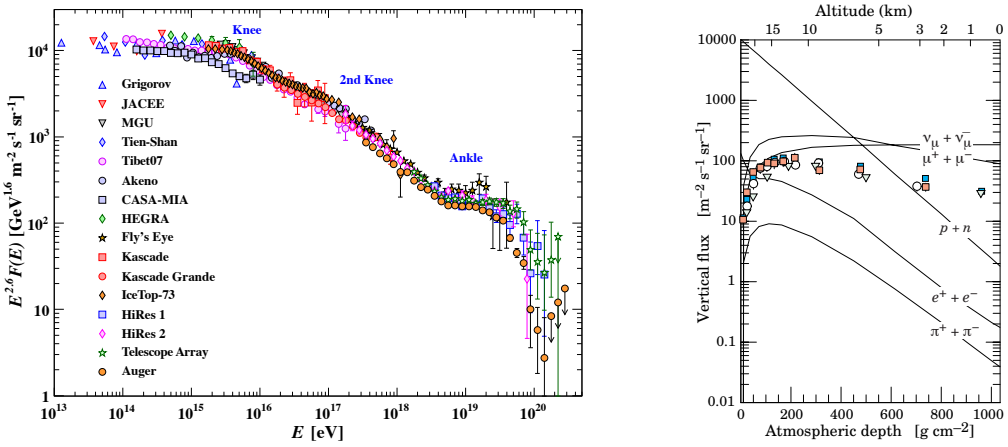

Figure 2.4: Left: The flux of cosmic rays measured by various experiments. At energies below the 'knee' the spectrum follows a $E^{-2.6}$ power law. At energies above the 'knee' the spectrum can not be described by a simple power law. Right: Vertical flux of the major components of cosmic rays as a function of atmospheric depth. Data points show measurements of muons with energies $E_\mu > 1$ GeV, recorded with various balloon experiments. (Both figures from Ref. [95]).

2.4 It came from outer space

The Earth is constantly bombarded with charged particles and ionized atomic nuclei, collectively referred to as *cosmic rays*. Being of great importance for exploring particle physics, they also pose new mysteries, as cosmic rays with extremely high energies above 100 EeV have been measured on earth[119, 120], which is illustrated in the left panel of Figure 2.4.

For the work presented in this thesis, the cosmic rays are of interest due to the particle showers produced when they strike the air molecules in the Earth's atmosphere. In these *air showers*, a large number of secondary particles are produced in the general direction of the primary particle, and the particle shower develops as the secondaries decay or undergo subsequent interactions with the atmosphere. In order to minimize the background from particles produced in the air shower, neutrino experiments are constructed deep underground.

The air showers will be dominated by neutral and charged pions. The neutral pions decay through electromagnetic showers producing photons and electrons/positrons, that have a low probability of penetrating deep into material, and are therefore of little importance.

The charged pions decay to muons and anti-muon neutrinos (at a nearly 100% branching ratio). If a muon decays before arriving at the neutrino detector it produces an electron (that is quickly absorbed), a muon neutrino, and an electron neutrino. So, at the surface of the Earth, the air showers are dominated by neutrinos and muons, both with a vertical flux of ~ 100 s^{-1}m^{-2}[95], significantly higher than the other major components illustrated on the right panel of Figure 2.4.

In the case of IceCube, which is covered by 1.5 kilometers of ice (as shall be discussed in further detail in the next chapter), only the muons and neutrinos reach the neutrino detector. Hence, they constitute the dominant background for the search of neutrinos from WIMP annihilations in the Milky Way in IceCube.

2.4.1 Atmospheric muons

Atmospheric muons penetrate into the volume of IceCube from above at a high rate, but their contribution can be reduced by focusing on signals starting within the volume of IceCube.

Even though the rate of atmospheric muons and neutrinos from air showers are about the same at the surface of the Earth, the rate of triggering on atmospheric muons in IceCube is many orders of magnitude higher than that of atmospheric neutrinos. Most muons above a certain energy will be detected in a neutrino experiments, whereas the low interaction cross section of neutrinos result in only a fraction of them being detected.

The flux of atmospheric muons disappears about 10 km below the surface of the earth[95], hence all atmospheric muons will arrive at IceCube from above. As a result the atmospheric muons are by far the biggest background for studies of neutrinos from the Southern Hemisphere. For the present search for neutrinos from WIMP annihilations in the Milky Way the dominant fraction of signal neutrinos will originate from the center of zur galaxy, which is located on the Southern Hemisphere. Hence, most of the focus in the event selection will be on removing atmospheric muons.

If their downgoing direction can be determined well enough, one can remove the atmospheric muons by identifying them as they penetrate into the detector. Neutrino-induced muons might also penetrate into the detector, but they can also start within the detector.. By detecting the light from muons entering the detector, the muons can be identified as possible atmospheric muons and removed from the sample. Many different techniques are developed and employed in order to veto the incoming muons, which shall be discussed through the event selection for the analysis.

2.4.2 Atmospheric neutrinos

Most of the atmospheric neutrinos penetrate the entire Earth without interacting, and since the cosmic ray flux is more or less uniform around the Earth[121], atmospheric neutrinos will arrive at IceCube from all directions. The atmospheric neutrinos are an important flux source in the measurements of the neutrino mixing parameters[122], but will be a background component in searches for neutrinos with extraterrestrial origin. The atmospheric neutrinos cannot individually be distinguished from signal neutrinos, instead the classification must be done statistically by looking at timing, energy, and direction. Neutrinos from WIMP annihilations described in this work are not transient events and the energy has not been incorporated into this work, since the energy can not be resolved well enough to provide a significant contribution to the sensitivity of the analysis. However, the direction is expected to be correlated with the dark matter halo of the galaxy, which differs from the uniform production of atmospheric neutrinos.

In this work the flux of atmospheric neutrinos described in Ref. [123] will be used. That flux model is estimated from cosmic ray observations, geomagnetic maps, seasonal variations in the atmosphere, etc. The flux model will be used to estimate the fraction of atmospheric neutrinos at the final level of the event

selection, however, in the final analysis, experimental data will be used to estimate the background.

2.4.3 Astrophysical neutrinos

The extremely high energy cosmic rays have sparked an interest in finding the astrophysical sources for the associated extreme accelerators. Currently no known sources have the size of field strength to accelerate protons and heavier nuclei to the energies observed in cosmic rays[124]. The search cannot be carried out with photons, as the universe is effectively opaque to photons with energies above 100 TeV, because they will pair produce electrons and positrons on the CMB photons[124].

Neutrinos offer the possibility to look for the astrophysical source by detecting extremely high energy neutrinos, and should be noted that in a dedicated search, IceCube found evidence of extraterrestrial neutrinos, with a few events with a reconstructed energy of about 1 PeV[125]. At the time of writing there are no evidence for significant clustering on the sky.

However, for neutrino energies below 100 TeV the astrophysical neutrinos will be swamped by the atmospheric neutrinos, which is also the case for the present analysis for which the astrophysical neutrinos will not be significant background.

3

IceCube Neutrino Observatory

Propagating charged particles passing through materials may be detected via emited Cherenkov photons. The IceCube Neutrino Observatory (IceCube) uses the 2800 meters thick ice layer[126] at the South Pole as a detection medium, and the photons are detected with a cubic kilometer array with thousands of digital optical modules (DOMs).

The initial feasibility study of using ice as a detection medium was carried out in Greenland[127], and the first generation neutrino detector in ice at the South Pole began with the deployment of AMANDA[128]. The efforts have always been to build something as large as possible in order to search for the rare, extremely high energy neutrinos. As such, the detection instrumentation must be much sparser than in a typical particle detector in order to cover as large a volume as possible, which is exactly possible by exploiting Cherenkov radiation and the very clear ice at the South Pole. The mission of detecting astrophysical neutrinos culminated with the recent success of IceCube in detecting the first neutrinos with energies above one PeV[125]. However, the size of IceCube also provides great possibilities for detecting neutrinos around 100 GeV, which shall be exploited to search for neutrinos from annihilating WIMPs.

This chapter shall present the properties of the ice at the South Pole, the topologies of the Cherenkov photons before and after detection in IceCube and cover the detection technique and layout of IceCube.

3.1 South Pole ice as detection medium

The ice at the South Pole is unique, and is formed by the compression of tens of thousands of years of snowfall. This means that the ice has not yet been reproduced in a lab, and it is not feasible to remove a sufficiently large sample to accurately and precisely determine the optical properties. The only way is to determined the properties of the ice in-situ.

3.1.1 Optical properties of the ice

Throughout the ice sheet, the optical properties of the ice change. This directly affects both the scattering and absorption of the ice. Generally the dominant cause for photon scattering is air bubbles, and impurities in the ice are the dominant cause for the absorption. Under high pressure, air bubbles in ice get embedded in the ice molecules (as so called gas clathrate hydrates) and effectively disappear. For the ice at the South Pole this phenomenon has been observed to occur 1200

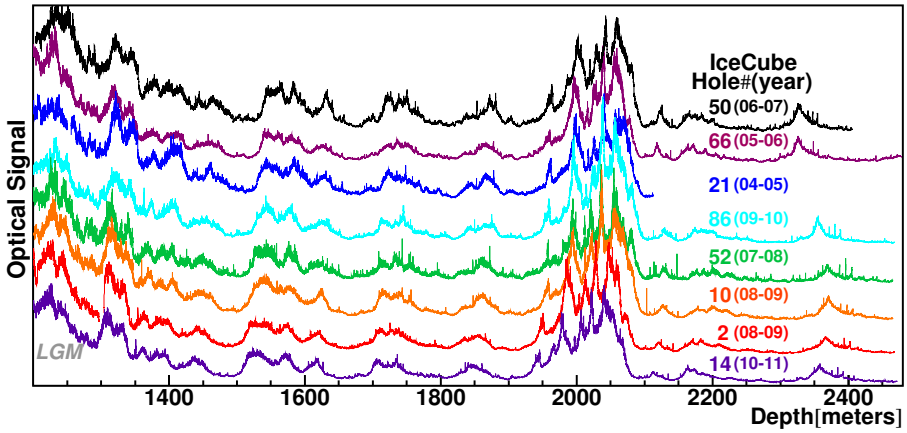

Figure 3.1: Photon count for the dust logger (see text) from 8 different drill holes. The count is related to the scattering coefficient, and demonstrates that the scattering gets continuously smaller as a function of depth, with the exception of some layers with a significantly larger scattering corresponding to dust from identified ice ages (from Ref. [133]).

meters below the surface[129], which in practice means that the scattering off of air bubbles becomes subdominant below a depth of 1400 m[130]. As IceCube is deployed between 1450-2450 m below the surface, the contribution from air bubbles can be ignored in the description of the ice around IceCube with the dominant contribution originating from impurities (or *dust*) in the ice. The effect on the photon propagation from the optical properties of the ice is quantified (measured and modelled) in terms of an effective absorption length a_{dust} and effective scattering length b_e[131].

Dust logger As a probe of the optical properties, a *dust logger* was lowered into 8 of the 86 boreholes (before deploying the detector modules), continuously emitting blue (404 nm) photons perpendicular to the hole, with a 90°opening angle. At the bottom of the dust logger a photomultiplier tube (PMT) was installed, optically separated from the emitter by two layers of light absorbers[132]. The photons detected by the photon counter will be dominated by back scattering of photons from the emitter, hence the photon count is correlated with the effective scattering coefficient of that given layer of ice. As can be seen from Figure 3.1, there is generally less scattering deeper in the ice, however, there are recurring layers in the ice where the scattering is enhanced, especially the *dust layer* at a depth of 2000-2050 m, originating from past ice ages where more dust were accumulated in the atmosphere. The dust logger further revealed a slight depth offset of the scattering peaks at different horizontal positions in the detector volume (running 225° SW)[133], corresponding to a varying *tilt* of the ice layers of a few percent.

Flasher runs A number of light emitting diodes (LED) are installed within the DOMs in the ice (described in Section 3.3), and by 'flashing' the LEDs the propagation of photons through the ice can be studied. With the position of the flashing DOM, the data from the non-flashing DOMs in these *flasher runs* is used to model the optical properties. An example of the photons originating from flashers in the ice is presented in Figure 3.2, showing that the ice changes optical properties at

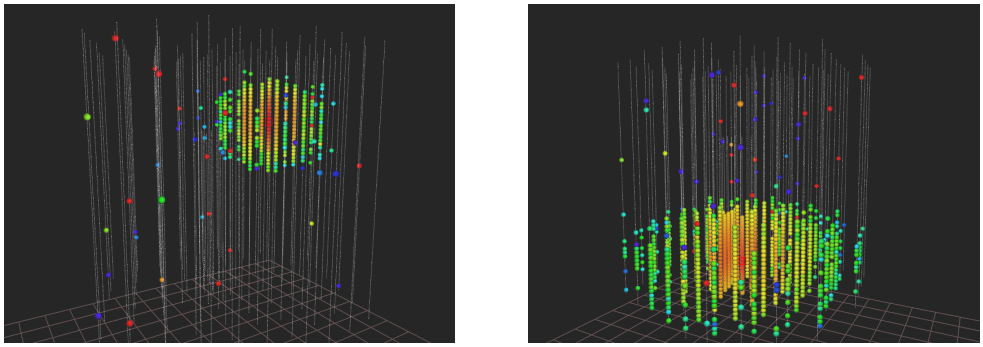

Figure 3.2: Data from two different events from flashing LEDs with the same intensity, with the flashing DOM encased by the red square. Left: flasher in the shallow ice. Right: flasher in the deep ice.

different depths. The brightness and timing of the LED flashes can be varied for different investigations (more details in Section 3.3.3).

3.1.2 Ice modeling

With the data from the flasher runs, the optical properties of the ice between 1450-2450 m is modeled by segmenting it into 100 vertical layers 10 m thick each with uniform values of a_{dust} and b_e throughout the horizontal plane of that segment (taking the tilt into account)[131]. From a given set of starting values for the 200 parameters, photons from one flashing DOM (emitter) are simulated and propagated through the ice, and the corresponding total charge and distribution of arrival times at the receiving DOMs (receiver) are determined. The distributions obtained from simulation are compared to the actual observation in the detector with the same set of emitter and receiver pairs, the 200 parameters are varied and new simulations are run until the most likely values for a_{dust} and b_e are found. The parameters are estimated with about 10% uncertainty (statistic and systematic errors), and, as is illustrated on Figure 3.3, the ice model follows the profile of the dust logger very well, which serves as a validation of the method. With values of $a_{\text{dust}} \in [18; 276]$ m and $b_e \in [5; 89]$ m, photons are scattered more in the ice than e.g. clear water, but the absorption is smaller[134, 135].

In order to judge how well the model describes the ice, the charge distribution of an emitter-receiver pair is measured in both data and simulation. The distribution of ratio between the data and simulated is fitted with a Gaussian, and the width is determined to be about 30% (depending on the events used in the calculation), and is quoted as the *model error* for the ice model. The model described above is referred to as *SPIce Mie* in the rest of the work.

A slight azimuthal anisotropy in the photon detection of about 10% (peaking in the direction of the ice flow) has been identified more recently[136]. The updated ice model, *SPIce Lea*, incorporates this effect which brings the model error down to about 18%, and shall be used as the baseline for simulation used in this work.

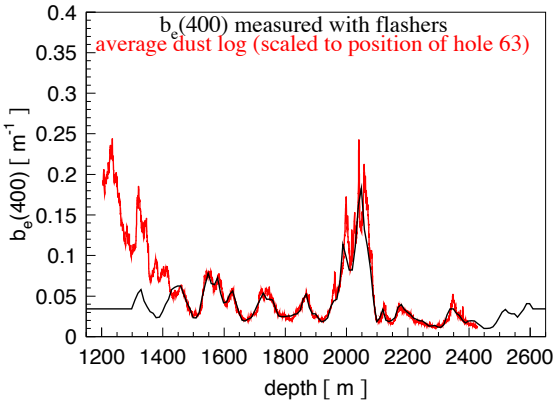

Figure 3.3: Comparison of the average dust log (red) to the inverse effective scattering length (on this plot referred to as b_e) determined from flasher data, providing a validation of the ice model for the South Pole ice (from Ref. [131]).

3.1.3 Hole ice

The modeling above only describes the *bulk ice*, but the DOMs are situated in refrozen ice from the water produced when melting the ice in the borehole. This *hole ice* will have different optical properties than the bulk ice. To visually monitor the optical properties of the hole ice and to follow the freeze-in, two cameras are installed in one of the drill holes. Using lights and lasers installed with the cameras, it has been confirmed that most of the impurities and bubbles from the water are situated in an inner column of the refrozen ice column, created as the water froze from the outer walls of the drill hole inwards. As a result, the scattering and absorption in this *bubble column* are relatively high (compared to the bulk ice), whereas the outer part of the refrozen ice columns is relatively clear.

The higher scattering in the hole ice (dominated by the bubble column) makes it more likely for down-going photons to be registered in a DOM, which has the PMT facing downwards. The scattering in the hole ice is therefore implemented as an angular acceptance modification in simulation, the shape of which depends on the effective scattering length. With the use of flasher data from AMANDA (the predecessor to IceCube), the effective scattering length in the hole ice is estimated to be about 0.17 m, significantly shorter than for the bulk ice[137].

3.2 Photon signals in the ice

With a model describing the scattering and absorption through the ice, it becomes possible to understand the light emission patterns in the ice for different neutrino interactions and backgrounds. In Figure 3.4, Cherenkov photons emitted by the particles produced in different neutrino interactions are illustrated. The color indicates when a given photon was produced, from red (just emitted) to blue (have been propagating through the ice for a while).

A muon neutrino charge current interaction produces a characteristic *track* as the ongoing muon propagates many hundred meters through the ice. In addition to the uniform Cherenkov radiation from the muon, the hadronic cascade from the

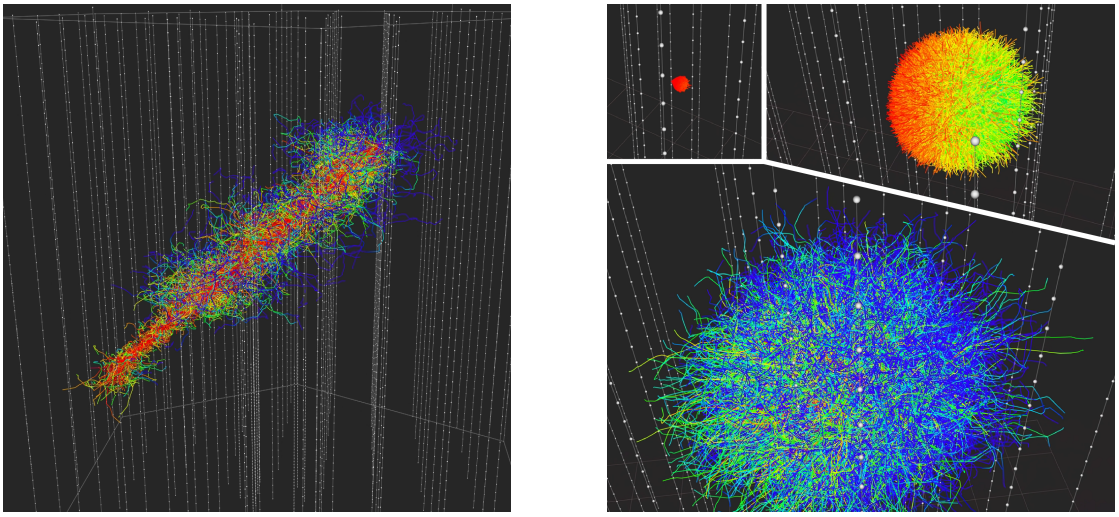

Figure 3.4: Simulation of photons produced in neutrino interactions with the color scale describing the timescale of a given photon depending on whether it has just been produced (red) or have propagated for a while (blue) (only 0.01% of the photons produced are shown). Left: A snapshot at the time of decay of the muon produced in a charged current interaction of a 200 GeV muon neutrino, after propagating a few hundred meters through the ice. Right: A cascade from an electron neutrino interaction, developing over the course of the three time snapshots developing a spherical cascade. Beginning with a clear Cherenkov cone from the initial electron propagating towards the left in the picture (upper left), the cone is soon drowned in photons from the secondaries from the electromagnetic cascade (upper right), though it is possible to gain some directional information from the timing of the photons, most of which is lost near the end of the cascade development (lower half).

interaction, the decay of the muon, and stochastic radiative losses of the propagating muon add secondary particles that might also emit photons.

Effectively, all other interactions produce the spherical *cascade* presented on the right of Figure 3.4. The picture is a montage composed of three snapshots of the photons produced in a charged current interaction of an electron neutrino at different times (same length scale). The cone of Cherenkov photons from the primary electron is visible on the first snapshot, but as the electron initiates the electromagnetic cascade and the photons propagate further away, the full shape gets more spherical. As the electromagnetic cascade dies off no more photons are produced and the remaining photons move further out through the ice until they get absorbed. From the color of the second snapshot it is clear that even though the cascade has a very spherical shape, there is a preferred direction following the initial electron.

At the energies considered, a charged current interaction of a tau neutrino would result in a photon signal like the cascade. There are naturally differences in the cascades produced by the different types of interactions, but most of the features disappear when one can only look at the photon production (and even more when considering that only a limited number of the photons are detected). Ultimately the efficiency and acceptance of the DOMs limits how clearly the photon signatures, available in the ice (and illustrated in Figure 3.4), can be captured by IceCube.

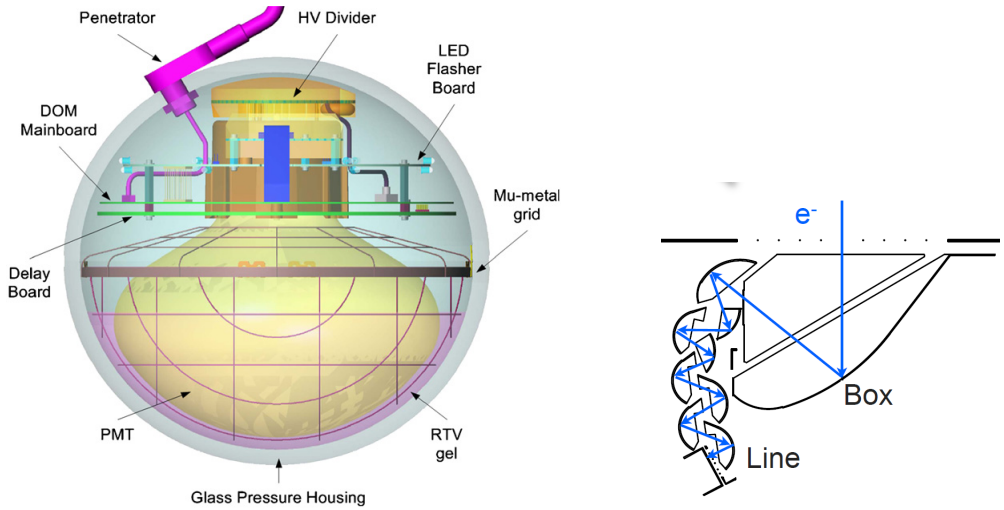

Figure 3.5: Left: The design of the 13 inch diameter Digital Optical Module with the most visible components being the PMT, the electronics boards, and the penetrator that serves as the only opening in the pressure sphere (from Ref. [138]. Right: A sketch of the box and line dynode structure employed in the IceCube PMTs.

3.3 Detection technology

In IceCube the Cherenkov photons is detected by photomultiplier tubes (PMTs) installed in the autonomous Digital Optical Modules (DOMs), containing all the electronics needed to record and digitize the signal from the PMT before sending it to the data acquisition system (DAQ).

3.3.1 Photon detection in the DOM

As the photon arrives at the DOM it must pass through the 0.5 inch thick glass of the pressure sphere which constitutes the outer shell of the DOM. The PMT is optically coupled to the glass with a gel to keep the scattering of the photon to a minimum and is shielded from Earth's magnetic field with a metallic net to improve the PMT collection efficiency (which is about 10% lower without shielding[139]). On the cathode of the 10 inch PMT, a photoelectron is knocked off by the photon with some *quantum efficiency* (QE). The glass of the pressure sphere is opaque to wavelengths longer than 350 nm (the gel has a cut-off at about 300 nm[140]), and the PMT loses sensitivity above 650 nm (peaking at 390 nm with a QE of 25%)[141] setting the sensitive range of the complete DOMs. PMTs with QE up to 35% are installed in the *high QE DOMs* deployed in later seasons (see Section 3.4).

The PMTs used in IceCube employ an asymmetric box and line dynode type structure (see Figure 3.5), and the photoelectron from the incident photon is attracted by the electric potential applied between the cathode and the subsequent dynodes. The amplification (gain) of the single photoelectron (SPE) through the PMT is about 10^7, resulting in an electric *pulse* with a voltage of about 8 mV[141]. The calibrated relationship between collected charge and number of photons is subsequently used to calculate the number of detected photons for a DOM in a given physics event.

Apart from the signal induced by the photoelectrons, there are other contributions. Many hundreds of nanoseconds after the main peak, a series of *afterpulses* can be detected. Afterpulses are the result of residual gas hitting the cathode, after being ionised by photoelectrons or their subsequent cascades, and account for about 6% of the overall photoelectron count, with an insignificant result on the reconstructions. In addition, *prepulses* caused by photons passing through the cathode and instead producing a photoelectron on the first dynode instead of the cathode, and *late pulses* arising from backscattering of electrons, are both subdominant effects compared to the time-smearing of the Cherenkov photons traveling through the ice[141].

3.3.2 Electronics

From a given pulse registered in the PMT, a *hit* is produced by the DOM electronics, containing the time stamp, a rough charge measurement, and the digitized *waveform* of the pulse. The analog PMT pulse is digitized in order to eliminate the analog cross talk which had been a problem in AMANDA.

The full information available for the event is only read out if *local coincidence* (LC) is observed. The LC condition is met when there is at least one additional hit on the nearest or next-to-nearest DOMs in the same drill hole within 1 μs. In that case, the pulse from the PMT is digitized on the Analog Transient Waveform Digitizer (ATWD), producing detailed waveform from 128 samples of the pulse, each with a length of 3.3 ns. Depending on the maximum charge, one of 3 gain stages ($\times 0.25$, $\times 2$, or $\times 16$) are applied in order to avoid saturate the digitizer. As it takes up to 29 μs to digitize the signal, two ATWDs are installed to decrease deadtime, as it allows a second digitization while the first ATWD is busy.

In addition the pulse is digitized by the fast Analog Digital Converter (fADC), which records the PMT pulse continuously, applying a gain of 16. The fADC digitizes the pulse with 265 samples of 25 ns length, hence providing a longer, but coarser waveform. If the LC condition is met, the entire 6.4 μs waveform is read out, and the fADC is ready again within 50 ns. The non-LC waveforms might be due to Cherenkov photons, so reading them out can provide valuable information. If there is no LC, only 3 samples centered on the peak of the fADC are read out.

3.3.3 Flashers

There are 12 LEDs installed in each DOM in six evenly spaced azimuth directions and two zenith directions, with intensity peaking at the horizon and 48 degrees above the horizon (after correcting for the diffraction of photons going through the DOM)[131]. The main purpose of the flashers is to calibrate and understand the detector, e.g. the geometry, the linearity of photon intensity measurements, and the ice properties (further discussed in Section 3.1.2).

The flasher LEDs can be programmed to flash with a rate of $610/2^x$ Hz (for $x < 9$), for durations up to 70 ns, and the total output of the LEDs can be varied from 10^6 to 10^{10} photons. The photons are emitted at a wavelength of 399 ± 14 nm, which corresponds to the wavelength with the highest intensity of Cherenkov photons (though 16 DOMs are equipped with LEDs emitting at different wavelengths)[131].

3.4 Detector layout

IceCube was constructed over 7 years and reached completion in 2011. The *in-ice* neutrino detection part of IceCube consists of two different layouts of 5160 DOMs in total, as indicated on Figure 3.6. 4680 DOMs are deployed with 60 DOMs on 78 strings in a systematic triangular pattern with an average string spacing of 125 m (except where the old pole station and landfills made drilling impossible). On each string the DOMs are deployed with a nominal spacing of 17 m, between 1450 m and 2450 m below the surface[82]. 480 DOMs are deployed in a more compact geometry on 8 strings with an average string spacing of 42 m, in order to produce a volume with denser instrumentation. The more compact array consists of an instrumented segment with 10 DOMs above the dust layer (*the plug*) and the remaining 50 DOMs below (*the fiducial*). The DOMs deployed in the fiducial segment (2100-2450 m) have a 7 m DOM spacing. The DOMs deployed in the plug (1750-1850 mbelow) have a 10 m DOM spacing and are designed as an additional veto layer[142]. For completeness it should be added that IceCube also has a surface array on top of the ice, where 160 water tanks (each with two DOMs) are used to study cosmic rays, and can potentially be used as an additional veto for very down-going atmospheric muons.

DeepCore fiducial volume The combination of the very central strings constitutes the *DeepCore* strings, as indicated with a dashed blue line on Figure 3.6. The DeepCore fiducial volume shall refer to the DOMs on the DeepCore strings that are situated below the top most DOM in the fiducial segment of the denser strings. Hence it includes DOMs with both nominal and high QE PMTs.

Coordinate system of IceCube Positions within IceCube are reported in a Cartesian coordinate system, where the $x-y$ plane is parallel to the surface of the Earth, and the z-axis perpendicular to that with the origin at an elevation of 883.9 m (2900 feet) above sea level. The y-axis is parallel to the Prime Meridian (pointing toward Greenwich) and the x-axis is perpendicular to that.

3.4.1 Realized geometry of in-ice detector

The positions of all the in-ice DOMs presented in Figure 3.6 are the realized *geometry* after completing construction. The layout was designed to be symmetric, but due to the old pole station, no strings could be deployed around $(x, y) = (200, 500)$, Instead the strings were reconfigured and deployed as dense strings together with the originally intended six strings. This is also the reason why the two strings #79 and #80 predominantly has DOMs with nominal PMTs, and only a dozen high QE PMTs.

The ice at the South Pole flows at about 10.1 meter per year (NW direction),[143]. From measurements with inclinometers installed in some of the drill holes, it has been determined that the ice shear is less than 0.002 per year[144]. For this negligible amount of ice shear, the detector will essentially move along with the ice, i.e. the relative positioning within IceCube is not expected to change. So when the geometry of the fully deployed detector is determined once, it stays the same.

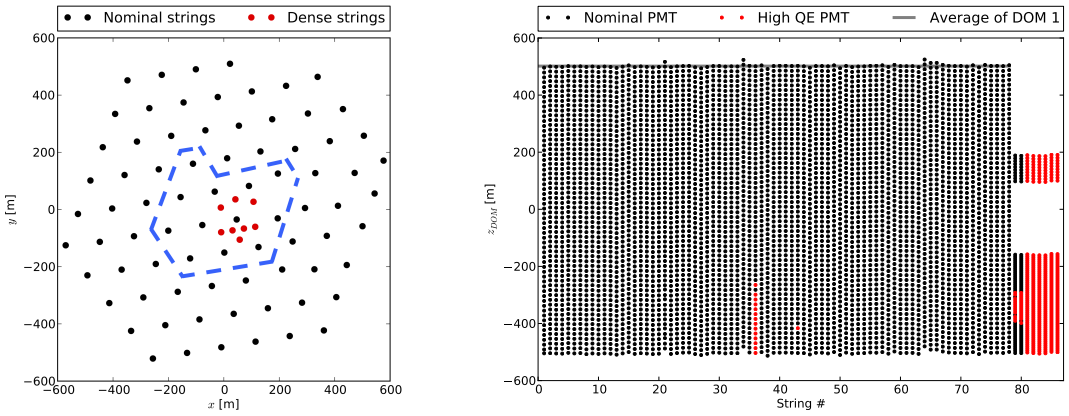

Figure 3.6: The realized position of strings and DOMs are presented using the IceCube coordinate system. Left: The (x, y) position of the strings of the IceCube in-ice array, with the DeepCore strings indicated with a blue dashed line. Right: The z position of the individual DOMs on the in-ice strings.

Stage 1 Geometry During deployment the GPS location for each drill hole is registered, and during drilling the drift is monitored using sensors in the drill, determining the offset of the DOMs assuming that the DOMs are in the center of the drill hole). Then the inter-DOM spacing is measured individually as they are lowered and the depth of the bottom-most DOM is determined from pressure measurements of the water column in the drill hole. The Stage 1 Geometry is formed using the combination of all position measurements of the detector's deployment.

Stage 2 Geometry Using flasher data, the leading edge of the photon travel time is measured for a few combinations of DOM pairs. From this information the distance between the DOM pairs is extracted and assuming that the DOM (x, y)-positions are consistent with those of the drill holes (within one meter), the z position is corrected to match the calculated distance. This constitutes the Stage 2 geometry which is used in this work. Using just the 5 nearest DOMs on the immediate neighbouring strings to triangulate the position of a given DOM, it was confirmed that the (x, y)-positions of the DOMs match that of the drill holes to within one meter.

3.5 Events in the detector

With the photon production and DOM hardware presented, a qualitative description of the possible event topologies in IceCube is helpful in visualising the experimental setup and understanding the steps taken in the analysis.

3.5.1 Tracks and cascades

Only DOMs that record a hit provide information about the photons produced in a given event. This means that the extensive photon production presented on Figure 3.4, results in the limited set of hits presented on Figure 3.7. Both panels show the hits recorded in charged current interactions of neutrinos with an energy of about

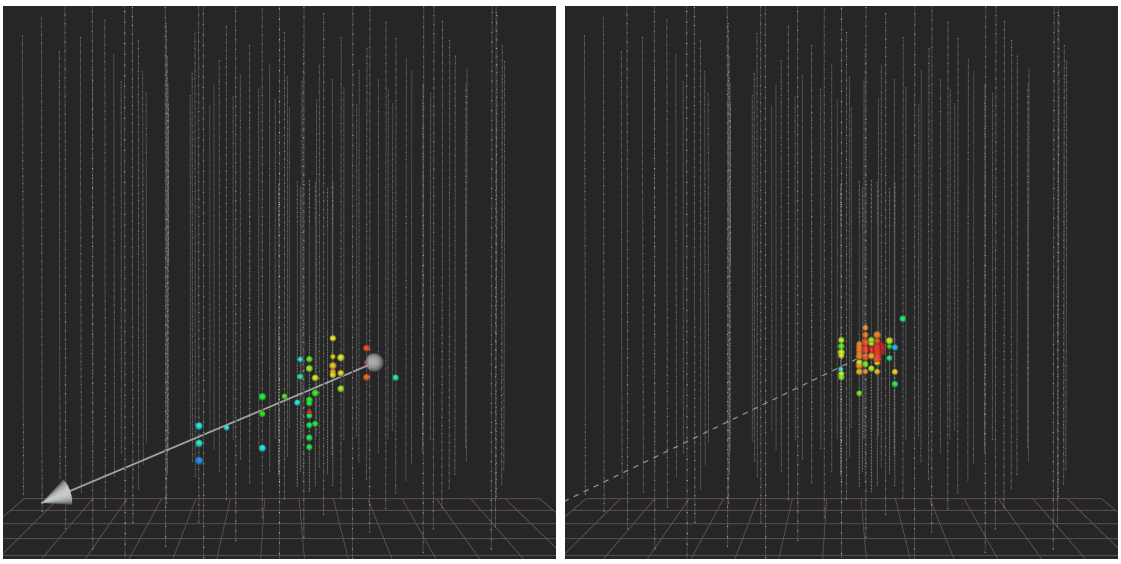

Figure 3.7: Left: Event display showing examples of the hits recorded from a 109 GeV muon track (with the arrow indicating the true position of the muon). Right: Event display showing a cascade of a 102 GeV electron (where the big red sphere indicate the interaction point, and the dashed line shows the direction of the primary electron from the interaction). For both of these events the noise hits have been cleaned away.

100 GeV. In the left panel a muon neutrino charged-current interaction produces a muon that propagates out of IceCube along the arrow producing a track of hits in its path. In the right panel an electron neutrino charge-current interaction produces an electron that loses it's energy in an electromagnetic cascade over a short distance resulting in a roughly spherically symmetric collection of hits.

However, if the track had been initiated in the middle of the denser strings (like in the cascade example) the hadronic cascade would be more visible, and if the muon had not been moving close to any strings there might not have been as many hits along the track. In that case the track will look more like the cascade, and the distinction between tracks and cascades becomes less clear. That is also the case as the muon energy decreases, which results in shorter tracks.

Generally, the resulting hit pattern of a neutrino interaction as a function of flavor, interaction, energy, and direction, will be strongly dependent on the position of the interaction within IceCube, due to the varying instrumentation density and ice clarity. Further, the relatively low detection efficiency of the DOMs means that a hit, recorded from the Cherenkov photons of one muon, might not be recorded for another muon with the exact same properties.

This becomes less of an issue at neutrino energies above a few hundred GeV, but is still important to keep in mind for the design of an event selection that can distinguish muons entering IceCube from muons produced by muon neutrino interactions within IceCube.

3.5.2 Noise

All around the particles propagating through the ice, DOMs register unrelated hits due to a range of effects that shall commonly be referred to as *noise*. The muon

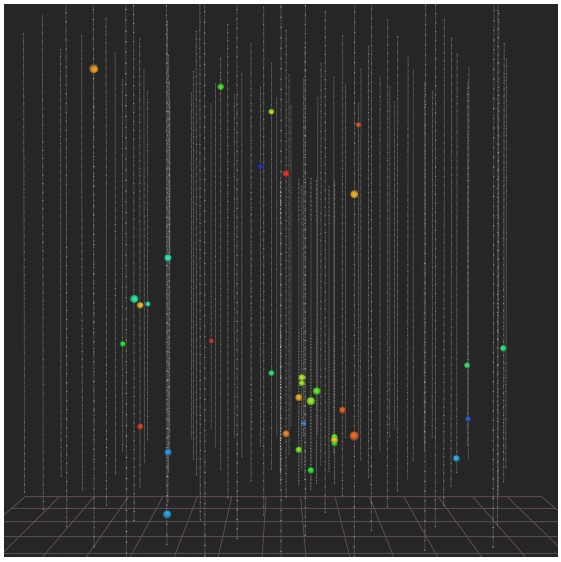

Figure 3.8: No cleaning has been applied to this event where no Cherenkov photons producing particles are present, it is therefore showing purely noise hits, corresponding to what would be on Figure 3.7.

neutrino and electron neutrino interactions shown in Figure 3.7 show series of hits that have been cleaned of noise. An event with only noise hits is presented in Figure 3.8. From the thermal noise in the electronics of the DOM, random noise hits are produced with a rate of about 700 Hz. Apart from that uncorrelated noise, it has been established that there is also a significant amount of additional hits correlated with previous hits on the same DOM that seem to originate from nuclear decays and faint scintillation in the glass sphere. The combination of those components results in an ever present background noise with an average rate of about 500 Hz for each DOM[145]. When trying to reconstruct an event, the noise adds misleading hits, and therefore it is important to clean the events as much as possible before going through the reconstruction algorithms (often applied early in the data processing).

3.6 Data processing

In order to limit storage requirement and the amount of uninteresting data that needs to be transferred from the South Pole, an online data processing system is employed at detection level to select relevant data that is more likely to be from neutrino interactions than from pure noise or atmospheric muons. This selection is based on the hits and LC information of a given event.

An IceCube event In this work an *event* shall refer to a time interval in data taking (typically 20 μs), selected with the intent that it contains interesting physics, e.g. a neutrino interaction or traversing muon. A data event will contain the digital waveforms from all the DOMs which recorded a hit within the time interval, used in the subsequent steps of the event analysis.

3.6.1 Triggering

The data acquisition system of IceCube continuously monitor the DOM LC signal, i.e. whether there is at least two hit on two DOMs that are each others nearest or next-to-nearest neighbors. The first level of selection is decided from a list of *triggers* based on various combinations of LC signal in IceCube. If at any given time the criteria of a trigger is fulfilled, the hit information from all the DOMs in the detector is read out for a given time interval around the time when the trigger condition was fulfilled. If time intervals of multiple triggers overlap, the most inclusive interval is read out, and subsequently split into multiple events. The events that trigger are referred to as *Level 1* (L1).

For this work only events fulfilling the Simple Multiplicity Trigger (SMT) are used. More precisely the SMT3, corresponding to 3 DOMs that have LC hits within a time window of 2.5 μs on strings in the DeepCore fiducial volume. The SMT3 has a rate of about 250 Hz, compared to about 2.9 kHz across all triggers in IceCube.

3.6.2 Pulse extraction

The digital waveforms for each hit in IceCube can not easily be used in further event reconstruction. Instead, the time and charge of the hit are determined. This is done for all hits even though more information is available for LC-hits. In this *feature extraction*, the waveform is first corrected for the time delay between the creation of the photoelectron and the time of digitization, as well as the complication from the inductive circuits between the PMT output and the digitizer. Then the calibrated waveforms are fit with templates describing the combined effect of the PMT and digitizer (specific for each gain channel) in order to extract the time and charge of the incident photoelectrons[146].

These *extracted pulses* are not providing the exact information of the hit, but the approach produces the best possible estimate. This set of extracted pulses form a *pulse series*, that serves as the basis for all subsequent reconstruction and analysis work.

3.6.3 Hit cleaning

The pulse series of all events will be contaminated by noise hits. This is problematic for e.g. event reconstruction algorithms where a fit might be pulled away from the actual value because of a noise hit, or a veto technique might result in removing too many actual signal events. Therefore a 'cleaning' of the pulse series is carried out to get rid of as many noise hits as possible, while retaining the hits caused by Cherenkov photons from charged particles in the ice. This can partly be done by exploiting that hits caused by Cherenkov photons will be clustered both in space and in time, whereas the noise will be randomly spread throughout the detector in space and time. The seeded radius-time (SRT) cleaning algorithm utilizes this spatial-temporal clustering, and uses the LC-hits as seeds for finding the pulses that should be kept. All non-LC hits that are within a distance of 150 m and a time of 1 μs of a seed are accepted and used as seeds for the next iteration. This continues until no more pulses are added and the accepted pulses constitute the *SRT cleaned pulses*.

3.6.4 Filtering

The triggered events are then run through a list of filters, and are only processed further if they fulfill the criteria of at least one filter. The events that pass the filtering level are referred to as *Level 2* (L2). There are numerous filters, and here it shall suffice to introduce the DeepCore Filter used in this work.

DeepCore Filter The center-of-gravity (COG) of an SMT3 event is calculated as the average position and time of the SRT-cleaned pulseseries within the DeepCore fiducial volume. The standard deviation of pulse times is calculated, and pulses further than one standard deviation from the average time are removed. A new COG is calculated for the remaining pulses. An event is only kept if there are fewer than two LC hits outside the DeepCore fiducial volume that can be causally connected with the new COG, where causally connected is taken to be an apparent speed $v \in [0.25, 0.4]$ m/ns between the DOM and the COG[142]. The rate of events that pass the DeepCore Filter is about 16 Hz.

3.6.5 Data transmission

The triggering and filtering comprises the online selection, and the data is transferred over satellite to the data warehouse at the University of Wisconsin-Madison (with a backup at DESY Zeuthen). Currently, the 100 GB/day bandwidth of the satellite is setting the upper limit for the throughput of the detector. About 80 GB is used for filtered data, and the rest is used for other special requests. There is also a backup saved to disk at the South Pole, which are shipped out once a year.

3.7 Detector stability

After detector completion, IceCube has had an uptime, i.e. fraction of the time where data is recorded, of about 99% on average, and in recent years the uptime is rarely below 99.5%. Due to a very stable operation of the detector, it is only when data for calibration is collected or in the event of rare software issues that IceCube experiences downtime. This is hugely important for the monitoring for the extremely rare signal from supernova explosions, however, for the signal neutrinos from WIMP annihilations the event rate is high enough that the high uptime mainly ensures as large a collection of events as possible. In this work, constraints are applied to the runs of data taking included in the analysis, that needs to show good data and run for longer than 100 minutes (ensuring a reasonable run length that will not be dominated by starting and stopping), resulting in about 95% clean uptime.

3.7.1 Dead DOMs

Since the ice at the South Pole does not experience any significant shear, the relative positions of the DOMs are not expected to change over time. However, the communication to a given DOM might break or some of the electronics in a DOM might die, which would exclude that DOM from data taking. For the data considered in this work, 86 of the 5160 DOMs in IceCube were not operational, due to

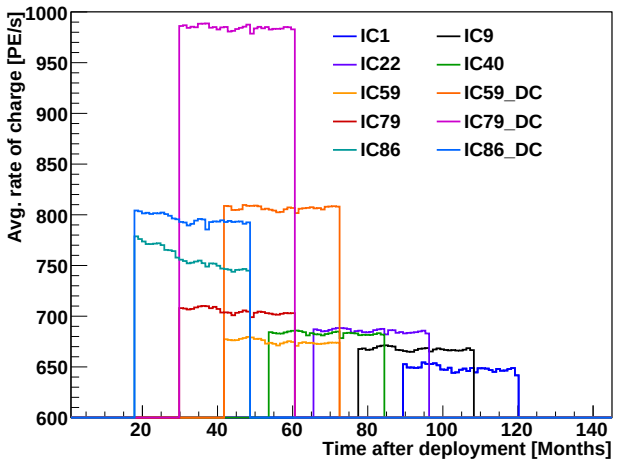

Figure 3.9: Average noise rates for DOMs as a function of time after deployment, illustrating the current decrease of noise rates for the strings most recently deployed (IC86 and IC86_DC). The DOMs are grouped into the different seasons of deployment, separating dense strings (DC) from nominal strings.

various reasons (poor communication, broken PMT, or simply never came online after deployment). The largest fraction of the dead DOMs were already dead at the time of deployment, and the rest have mainly stopped working following long power outages at the South Pole. The emergency power supplies keep power on IceCube for 15 minutes, but after that the DOMs power off, and cool down with about 10° C to the surrounding ice temperatures between -40° C to -20° C (warmer at larger depths), which might have caused DOMs to die after long power outages.

Only two of the DOMs died during the data taking considered in this analysis. Both are on a string at the edge of IceCube, and represent a vanishingly small fraction of the available DOMs, so they are not expected to have an impact. A slightly larger number of DOMs are running in a non-standard mode after encountering minor problems throughout the years of IceCube. Most of these non-standard DOMs are located next to dead DOMs. As the dead DOMs cannot check for LC conditions, the functioning neighboring DOMs are permanently set to fulfill the LC condition.

3.7.2 Decreasing noise levels

The noise hits in IceCube are decreasing with time after deployment, asymptotically reaching a stable level after a few years in ice which is illustrated on Figure 3.9. For the data used in this analysis, the change amounts to just a few percent, with the largest effect on the DOMs deployed most recently. This small change in noise levels is not expected to have an effect on the present analysis since all events with only noise are cut away early on in the event selection and the pulse series gets cleaned for noise such that the change in rate is negligible.

3.7.3 Continuous calibration

The baseline of the pulse digitizers (when they do not see a signal) is computed at the beginning of each physics data run. The transit time taken from photoelectron production to waveform readout from the digitizers is determined using a weak LED built into the electronics, and used as part of the feature extraction.

Since photons are discrete, the charge of the pulse from the PMT corresponding to a single photoelectron (SPE) can be determined for a given DOM using dark noise in the PMT. In this way one can establish the relation between voltage and gain, and the desired point of operation of the PMTs with a gain of about 10^7 can be achieved in the individual DOMs. This result in corrections of a few percent to the voltage which is applied continuously throughout the year, keeping the gain at the desired level of about 10^7.

The timing in the DOMs is known to 2 ns precision, which is important when measuring on particles moving with relativistic speed. The high precision is achieved with the frequent reciprocal active pulsing calibration (RAPCal) of the clocks in the individual DOMs to a common GPS clock at the surface. During RAPCal, a pulse is sent from the computers with the GPS clock to a DOM, the DOM registers the pulse, waits a fixed time d before sending an equal signal back to the surface. From the two sets of sending time, arrival time and received waveforms, the time offset between the two clocks is determined. Due to the limited information transmitted during a RAPCal, the calibration does not interfere with normal data taking[138].

3.7.4 Changes to the processed data

Finally the online data selection is periodically varied, by introducing new trigger items or filters. However, for the data considered, the trigger and filter items used in the analysis have not changed.

The fact that the detector has not changed significantly since completion, means that data for multiple years can be added more or less seamlessly.

4

IceCube Event Simulation

IceCube is sensitive to the passage of any charged particle, but only atmospheric muons and neutrinos will reach IceCube and produce Cherenkov light that will be detected. For the analysis of this work, the neutrino signal from WIMP annihilations is estimated by simulating neutrinos interacting with the ice at the South Pole, propagating the photons produced, and emulating the response of IceCube. In this chapter the details of the IceCube simulation chain will be presented, covering the production of both neutrino interactions and atmospheric muons. The simulation chain will be described by the following steps:

1. Particle event generation and/or interaction simulation
2. Particle propagation through the ice and photon production
3. Photon propagation through the ice
4. Noise emulation
5. Detector response simulation

4.1 Particle event generation and/or interaction simulation

Only atmospheric muons and neutrinos enter IceCube, so there will only be the need for simulating incident particles of those types. Depending on the type and/or energy, the interactions are modelled with different tools, in order to optimise the computation time.

4.1.1 Neutrino interaction simulation

The *GENIE Neutrino Monte Carlo*[147] (GENIE) is used to simulate interactions between neutrinos and target nuclei in the ice, generating the set of particles that are produced. For a neutrino with a certain flavor, energy, and direction, GENIE simulates a random (allowed) interaction. All neutrinos simulated are forced to interact, and subsequently each event gets a weight assigned according to the probability of that given interaction. The weights are used to get a realistic distribution of the events, independent on which interactions actually happened to be simulated. Compared to NuGen presented below, GENIE does not only include deep inelastic scattering, but also the suite of (quasi)-elastic and resonant interactions that

are relevant at neutrino energies below 100 GeV. This provide an added accuracy in simulating the neutrino interactions, though only a small fraction of the final events of this analysis originate from other than deep inelastic scattering (discussed in Section 2.2).

The current implementation of GENIE is used to model neutrinos with energies between 1-1000 GeV only. The GENIE datasets used in this work are generated according to an energy spectrum similar to that of atmospheric neutrinos, as the sets were produced for use in neutrino oscillation studies. However, for all events in the simulation a weight is calculated, such that the events can be re-weighted to any hypothesized neutrino signal. In addition, the neutrino events are also weighted according to their arrival direction, depending on the hypothesized neutrino signal.

In the initial studies for this work, the neutrino generator *NuGen* was used, as GENIE was only used to simulate events up to 200 GeV at that time. NuGen is an IceCube implementation of the ANIS event generator[148], that simulates deep inelastic scattering of neutrinos with the nucleons in the ice. Since the current GENIE simulation sets cover the relevant energy range of this analysis (as it simulate events up to 1 TeV), the NuGen files have not been used further than for the initial design of the event selection.

4.1.2 CORSIKA

In order to simulate the dominant background of atmospheric muons, the COsmic Ray SImulations for Kascasde[149] (*CORSIKA*) is used. CORSIKA is a simulation project for describing extensive air showers, and simulates the particles as they propagate through and interact with the atmosphere, until all particles have vanished or hit solid ground.

CORSIKA is run with some specific adaptations for IceCube. Neutrinos are not propagated in the CORSIKA simulations run in IceCube, and are instead modelled with the GENIE data sets. For the CORSIKA data sets investigatedin this work the SIBYLL hadronic model [150] is used, the composition of the primary cosmic rays are simplified to only five components (H, He, N, Al, Fe), and the energy distribution of these primaries follow the GassierH3a model[151]. Only the muons from the air showers are saved and propagated down to IceCube, because all other baryons, mesons, and leptons will be absorbed in the uninstrumented ice above IceCube. Even though only the muons are used, the full CORSIKA simulation is run in order to get the correct energy distribution of the muons.

In this analysis the background will be estimated from experimental data in the final analysis and not from the distributions from CORSIKA. Instead the CORSIKA sets are used to cross check the integrity of the general simulation chain.

4.2 Particle propagation

With the list of particles produced from GENIE or the set of muons from CORSIKA, the propagation and interaction of these particles are handled by different simulation projects depending on particle type and energy.

For the datasets used in this work the muons are propagated using `PROPOSAL`[152], a tool specialised for exactly that task configured with the details on both the uni-

form energy loss from ionisation and the stochastic losses from bremsstrahlung, nuclear interaction, and pair production as the muon moves through the ice. `PROPOSAL` also propagates any secondary leptons produced by the muon, and generates the Cherenkov photons that are emitted as the secondaty particles propagate through the ice.

Hadrons with energies less than 30 GeV, tau leptons, and muons from subsequent decays of the hadrons, as well as electrons and photons with energies less than 100 MeV are directly propagated using `GEANT4`[153]. The photon output of all hadrons with an energy above 30 GeV is evaluated using a parametrized form of the combined behaviour of the hadronic cascade. It has been demonstrated that the photon yield of this parametrization is not significantly different from that of directly propagating the individual particles.

4.3 Photon propagation

Photons with energies above 100 MeV are propagated through the South Pole ice using the IceCube specific project `clsim`[1]. `clsim` simulates the propagation of each individual photon through the ice until it is either absorbed by the ice or arrives at the surface of a DOM. The photon propagation applies the probability of absorption or scattering from a given ice model (discussed in Section 3.1.2). The photons that reach a DOM are kept with a specified probability based on their arrival direction and wavelength.

The different optical properties of the bubble column in the hole ice is parametrized as a function of incident angle between photon and DOM, thereby yielding a probability of the photon reaching the DOM (will be discussed further as a systematic uncertainty in Section 6.4).

The combination of the glass, gel, and PMT result in a limited wavelength acceptance of the DOMs, and a photon is kept with a certain probability corresponding to the acceptance at the wavelength of the photon.

Finally, each photon at the front of the PMT is kept with a probability corresponding to the quantum efficiency of the DOM. The resulting simulated photoelectrons (or *MCPE*s) are then used to simulate a response in the PMT base and DOM electronics.

4.4 Noise emulation

Before the electronics response of the MCPEs in the DOM is simulated, the effect from noise in the detector is added. Using the IceCube specific project `vuvuzela`[145], additional MCPEs are added for each DOM to the series of physics MCPEs (from the simulated Cherenkov photons) within a time window of 10 μs before and after the first and last existing MCPE. In the DOMs there are uncorrelated noise hits (originating from random thermal electronic noise) and noise hits correlated with previous hits in the DOM (most probably originating from scintillation light from radioactive decays in the glass sphere).

[1] github.com/claudiok/clsim

First, a number of uncorrelated noise hits are sampled from a Poisson distribution with a rate of about 20 Hz and distributed uniformly in time. The correlated noise hits are initiated with an uncorrelated component drawn from a Poisson distribution of about 200 Hz and also distributed uniformly in time. For each of those initial hits, a number of additional hits drawn from a Poisson distribution with a mean of 8 are determined, and their time relative to the initial hit is drawn from a log-normal distribution. The numbers mentioned are the common values, though it varies for different DOMs. The governing distributions have been determined from investigating the distribution of noise in the detector from special data runs, an then the individual components are fit for each DOM in order to accommodate variations across the detector[145].

4.5 Detector response simulation

With a set of individual MCPEs 'at the front of the PMT' (i.e. just after the PMT cathode), the IceCube program `PMTResponseSimulator`[154] simulates the response of the PMT to of each MCPE. The height of the pulse is sampled from a distribution of pulse heights observed in measurements on the PMTs deployed in IceCube, and is assumed to be the same for all DOMs (even though there might be differences). Similarlym the time delay for each pulse relative to the time of the MCPE is sampled from a distribution of time delays observed in the measurements of the PMTs in IceCube. In addition to the nominal pulses the response of prepulses (0.7%) and late pulses (3.5%) are also included (discussed in more detail in Section 3.3) in the time delay distribution. Each MCPE has some probability of producing an afterpulse (which itself can also create an afterpulse), which adds to the final set of MCPEs. Finally the time delay distribution is smeared with a small asymmetrical jitter in time which represents the non-uniformities of the PMT. In `PMTResponseSimulator` the saturation of the PMT is also taken into account by lowering the charge of the PMT pulses appropriately[154].

With the resulting charge and time delay of the PMT simulated, the response of the detector electronics are simulated with the software project `DOMLauncher`[91]. The local coincidence (LC) conditions are evaluated like it would be in the real detector by communicating the signals between DOMs, and depending on whether the LC condition is met, the pulse is digitised using either the detailed ATWD or the coarser FADC (taking into account that the ATWDs can be busy or in the dead time state). A template corresponding to each digitizer (and individual gain channels) for the specific DOM is used to turn the charge and delay time from the MCPEs into a simulated pulse. The templates are determined for each individual DOM (from calibration runs taken in-situ), reflecting the response of the PMT with all possible effects (and artifacts) included[91].

After the detector response the events are checked against the list of triggers used in experimental data. The implementation of the triggering software used for simulation emulates the one used for experimental data, with some historic and convenient variatons[154]. From here on out, the events are run through the same hit cleaning and filtering as the datasets from the experiment (presented in Section 3.6).

The years of data taking used in this analysis are all years with a stable detector

configuration (see Section 3.7), hence the simulation covers all the years considered. So at this stage of the thesis, both simulation and experimental datasets are in the same state and the more analysis specific event selection can be applied on an equal footing to both of them.

5

Data selection

With the experimental and simulated datasets understood, the search for a signal from WIMP annihilations can begin. The approach consists of two parts. First a *data selection* is done with the focus on removing background events and retaining expected signal events, in order to arrive at a more condensed *final selection*. Then the *final analysis* is carried out on the final selection, where the experimental data is ultimately compared to distributions of the expected signal and background to see if there is an excess of neutrinos above a background-only expectation. In this chapter the data selection shall be presented, starting with a more qualitative discussion of the approach, followed by a presentation of the details of the actual event selection. A presentation of the event rates going through the event selection is given and lastly the properties of the final selection shall be discussed.

5.1 Signal and background components

The event selection is designed from investigating the expected distributions of muon neutrinos from WIMPs in the galactic halo with a mass of 100 GeV, annihilating through W^+W^-. This shall be referred to as the *benchmark* signal, and other signal combinations shall be highlighted when relevant. The neutrinos from the WIMP annihilations shall commonly be referred to as the *signal neutrinos*.

The present work is focused on muon neutrinos, as the neutrino induced muon tracks generally have a better pointing resolution, which is relevant because the final analysis is based on the arrival direction of the neutrinos. Other neutrino flavors are also produced in the WIMP annihilations, and the contributions are taken into account in the final analysis. Though, the directional resolution of electron neutrinos, tau neutrinos, and all neutral current interactions is worse, because they produce cascades in IceCube. This means that the directional information will be smeared out and they will contribute less to the sensitivity than charged current interactions of muon neutrinos.

The contributions from electron neutrinos and tau neutrinos to the signal are included in the design of the event selection. However, there will be neutrino induced muon tracks in the sample that either produce too few hits or have too short a length to distinguish the event from a pure cascade event. In addition, the neutral current interactions of muon neutrinos are included in the sample used to design the event selection, and they constitute a significant fraction of the final events. This means that interacting electron neutrinos and tau neutrinos that share similar characteristics with the muon neutrino sample also will be included. And as it

shall be clear from the presentation of the rates, the contribution to the signal from electron and tau neutrinos is not negligible in the final selection.

Signal in the equatorial coordinate system The arrival direction of particles with respect to IceCube is given in terms of the zenith angle $\theta_{\text{zen}} \in [0, \pi]$, measured from the direction of positive z in the IceCube coordinate system and down, and the azimuth angle $\phi \in [0, 2\pi]$, measured from the positive x axis towards the positive y axis. As such, a particle arriving from exactly above IceCube has $\theta_{\text{zen}} = 0$, and a particle from exactly below have $\theta_{\text{zen}} = \pi$. However, when describing objects in the universe, it is beneficial to use a coordinate system that is independent from the local coordinates of the Earth. For this analysis the equatorial coordinate system will be used, which is based on the equator of the Earth, projected onto the celestial sphere, such that *the equatorial plane* divides the celestial sphere into two halves. The declination, dec $\in [-\pi/2, \pi/2]$ is the angle above the equatorial plane, and the right ascension RA$\in [0, 2\pi]$ is the angle along the equatorial plane. RA is measured eastward from the point where the path of the sun crosses the equatorial plane from south to north (the March equinox). The dominant signal contribution comes from the galactic center of the Milky Way, located on the southern sky at dec $= 29.008^\circ \pm 0.003^\circ$ and RA $= 277.414^\circ \pm 0.002^\circ$ in equatorial coordinates (fixed to January 1, 2000 (J2000))[155].

Dominating backgrounds The fact that most of the signal neutrinos arrive from the southern hemisphere means that the biggest background is from atmospheric muons penetrating through the ice from above. Atmospheric muons are produced in the air showers of cosmic rays colliding with the atmosphere (discussed in further detail in Section 2.4.1) and can travel multiple kilometers through ice (depending on the energy). The atmospheric muons can either enter and exit the detector (through-going) or can enter and stop (stopping). The neutrino induced muons (or other leptons) might be produced outside of IceCube and move into IceCube, but they can also have a starting vertex within the volume of IceCube. This important difference gives the possibility to distinguish atmospheric muons from neutrinos (of any origin). Demanding that the lepton is produced in IceCube, or similarly that the light production (i.e. cascade or track) is *starting* within the fiducial volume, ensures that the lepton and associated track or cascade originates from an interacting neutrino. How this is carried out, shall be discussed in Section 5.3.

The other significant background is from atmospheric neutrinos. They can not be distinguished from signal neutrinos event by event, but the distributions of their arrival direction differ from the signal neutrinos. Atmospheric neutrinos are produced with a uniform distribution in right ascension, whereas the signal neutrinos will have a strong preference for the right ascension corresponding to the galactic center. The atmospheric neutrinos will be subdominant to the atmospheric muons, but not negligible in the final selection.

5.2 Datasets and blindness

The event selection is designed using simulated datasets to determine the distributions for signal neutrinos and the various backgrounds. Simulated GENIE datasets

are used to represent the signal neutrinos for the benchmark channel, as well as the atmospheric neutrinos. Experimental data with the possible contribution from signal neutrinos subtracted is used in the final analysis to estimate the atmospheric background.

When designing the event selection, only a smaller subsample of the experimental data is used, more precisely 10% of the data amount collected in one year. Throughout the event selection the signal contamination will not be subtracted, since even by assuming a WIMP annihilation cross section, $\langle \sigma v \rangle$, equal to that of the current best limits, the sample will be dominated by atmospheric background. This *burnsample* will not be used in the final analysis (following the blindness criteria, see below).

To ensure that the simulation of signal neutrinos represent the actual neutrino signal, the simulation chain is compared to data throughout the event selection. For the selection of downgoing neutrinos with energies below 1000 GeV used in this analysis, it is not feasible achieve a very clean neutrino sample that is significantly large enough to offer a comparison of only the atmospheric neutrinos in simulation and experimental data. Instead, CORSIKA datasets with simulated atmospheric muons are used to monitor the correspondence between simulation and experimental data. It is also the only possibility for inspecting the correspondence at early stages of the event selection, where atmospheric muons will dominate the atmospheric backgrounds. Hence, the comparison between data and simulation will be between the burnsample and the simulation of atmospheric muons only, providing a measure of how well the overall simulation chain represents actual data.

5.2.1 Blindness

The burnsample is not only set to 10% of a year of data in order to limit the signal contamination of the background estimator, but also in order to avoid any unintentional bias throughout the event selection. Without having the full data sample, there is no way of determining the exact effect of applying a specific cut, and the choice of selection variables and cut values must be based on more general considerations of the expected sensitivity, which shall be further discussed in Section 6.3.3. Hence one does not have the possibility (intentionally or not) of enhancing some feature in the dataset that looks like signal (but might just be a statistical fluctuation). In the final analysis only the arrival direction shall be used, and the right ascension will dominate the discrimination between background and the signal from WIMP annihilation.

The right ascension of an event in IceCube can be determined from the time and azimuthal direction, so in principle only the time and azimuth should be kept blind. However, as other features might show up through the event selection, the study of the full dataset is only carried out after the full analysis has been designed and approved by the IceCube collaboration. Then after *unblinding* the full dataset is run through the analysis to get the final result. At that time other variables can then be investigated if needed, but the event selection and analysis will not be changed at that stage.

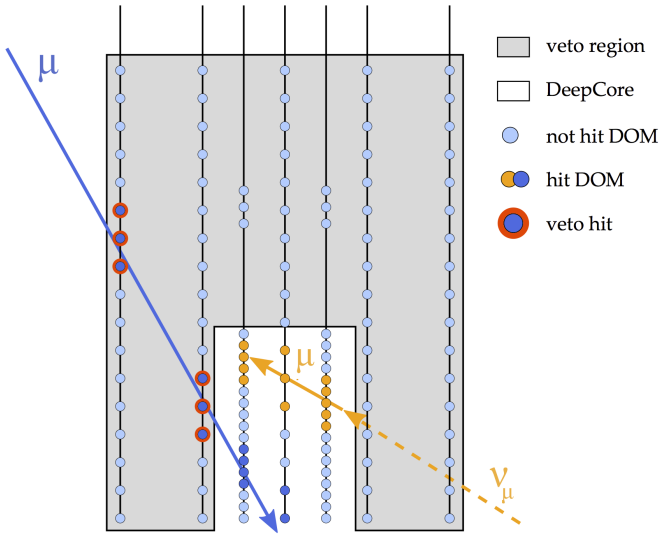

Figure 5.1: Illustration of the use of a veto for rejecting atmospheric muons (blue) that will be entering the fiducial volume through the veto volume, whereas neutrino induced muons (yellow) are as likely to start within the fiducial volume (from Ref. [156]).

5.2.2 Selecting the experimental data sample

The experimental data taking of IceCube is done in batches of about a year, where each data taking season starts around May. In this analysis, experimental data from the seasons 2012, 2013, and 2014 will be used. Data before season 2011 was recorded with the unfinished detector. It was decided to run the analysis on data from the complete detector only, for which all simulation and calibration is updated. However, even though it was a full year of a full deployment data the season 2011 was excluded from the sample as the rate of the DeepCore filter (and others) varied throughout the year, and are not similar to the rates in subsequent seasons that all match up (see Section 3.7 on detector stability). Part of this is due to an update of the DOM electronics firmware midway through the season, fixing a bug which unintentionally kept the ATWD digitizers busy for too long, resulting in fewer hits being read out. This alone increased the rates on the DeepCore filter with 10-15%, but since it is not clear if that is the only effect, the complete set of data from the 2011 season has been excluded from this analysis. As the present analysis was concluded just around the end of the 2015 season, the data for the 2015 season could not be included in this analysis.

5.3 Event selection strategy

The basic strategy is to identify starting events, which signify a neutrino induced event rather than an atmospheric muon, illustrated in Figure 5.1. In practice this hinges on the ability to identify the muons as they enter IceCube. This is difficult due to the scattering of photons moving through the ice, the limited efficiency of the DOMs, and the distance between DOMs, all of which gets increasingly difficult at lower energies where more and more layers of instrumentation are needed to tag penetrating muons. IceCube has a finite size, and even though only a fraction of

the active volume is used as fiducial volume, there will always be some amount of muons *sneaking* into the fiducial volume, i.e. penetrating muons for which the light is only detected in the inner regions of IceCube, imitating a starting event.

In order to tag as many sneaking muons as possible, the event selection is run as an iterative process, where at each level the most obvious atmospheric muons are identified and removed. At each successive levels it gets more and more difficult to distinguish starting events from sneaking muons. However, by steadily bringing down the rate of events at subsequent levels, more time consuming event reconstruction algorithms or calculations of derived quantities thereof becomes available, because running the algorithms over the remaining events becomes feasible. The first couple of levels use straight cuts on various variables, and only at the last level will a multivariate analysis be used to distinguish signal from background. This approach is taken to be as explicit as possible with the cuts, making it easier to assess the effect of a given cut and understand a possible disagreements between data and MC simulation.

After applying the cuts on level X, the data shall be referred to as being *at level* X (LX). The event selection presented here is based on the 79-string configuration of IceCube which established a good selection for the first few cut levels[157]. In this work those cut levels have only been slightly updated, and the significant update is reserved for the more challenging final level with the introduction of more advanced reconstruction algorithms that are providing essential information for the final level of the event selection.

Initially, the use of energy in the final analysis was considered, hence the event selection was intended to not rely on any variables strongly correlated with the neutrino energy. It was later decided not to include energy in the analysis, due to time constraints and too small improvements of the sensitivity. However, by keeping the event selection as independent of energy as possible, the decrease in efficiency for other combinations of WIMP mass and annihilation channels is minimized.

5.4 Cut level 2

Data at level 2 is the general dataset from IceCube with all the events that trigger a readout and pass at least one of the event filters (discussed in Section 3.6). It constitutes the minimal criteria one can impose on events in IceCube (for regular data taking), and form the common dataset from which the event selection for a given analysis start.

5.5 Cut level 3

First a set of very basic containment conditions and event quality criteria are imposed on data using detector level quantities. The cuts are intended to ensure an event quality needed in running the event reconstructions and limits the rate of events that need to be reconstructed by reducing the number of pure noise events and obvious incoming atmospheric muons.

5.5.1 Pulse containment

The DeepCore Filter is focusing on selecting events starting in the DeepCore fiducial volume, while rejecting penetrating muons by identifying hits outside the DeepCore fiducial volume that are causally connected to the hits inside the volume (details presented in Section 3.6). That criteria is here restricted further in order to reduce the amount of atmospheric muons entering from above. Hence, events are rejected if they have any SRT cleaned pulses on DOMs located in the upper half of IceCube, i.e. above a z position of -9 m. Further, the three first occuring SRT cleaned pulses must be within the DeepCore fiducial volume, removing the most obvious candidates of penetrating muons.

5.5.2 Number of strings

For most of the reconstructions, only the SRT cleaned pulses will be used. With all the SRT cleaned pulses in an event on one string, one can only hope to determine the zenith angle reasonably well, but not the azimuth angle. Hits on two strings makes it possible to get some idea of the azimuth angle, however with at least 3 strings it is actually possible to determine an interaction vertex. In this analysis events are required to have more than 3 strings in order to ensure a good reconstruction quality.

5.5.3 Number of channels

Each DOM that register at least one hit counts as a *channel*. Hence, the number of channels, n_{channel}, measures the number of DOMs with at least one hit. A cut on n_{channel} can limit the amount of events caused solely by noise hits. The contribution from noise falls off extremely fast with n_{channel}, and by demanding $n_{\text{channel}} > 10$, pure noise events can be almost completely removed. Additionally, the fewer channels available, the more difficult it is to reconstruct the track (or cascade), hence the cut helps ensuring a good freconstruction quality.

5.5.4 Summary of cut level 3

The signal neutrinos with bad event quality has been removed, and the most obvious atmospheric muons penetrating into IceCube have been removed. The rate has been descreased significantly, and it is feasible to run a suite of event reconstructions. After cut level 3 the experimental data (dominated by atmospheric muon background) has been reduced with about 4 orders of magnitude, and nearly all pure noise events have been removed, as shown in Table 5.1.

The cuts applied at level 3 are listed below for reference:

1. Event has passed DeepCore Filter condition
2. No pulses on DOMs above $z = -9$ (corresponding to DOM 31 (11) on nominal (dense) strings)
3. $n_{\text{channel}} > 10$
4. $n_{\text{strings}} > 3$

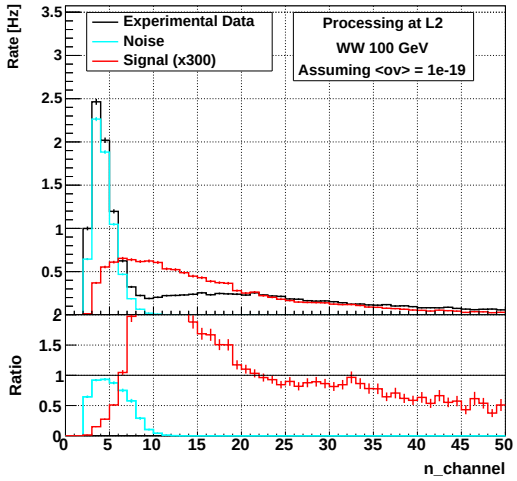

Figure 5.2: Distribution of n_{channel} for events at level 2 that pass the DeepCoreFilter. The experimental data in black is compared to the distribution of events from purely noise in teal, illustrating that the the experimental data is dominated by noise events for low n_{channel}. Additionally, the signal muon neutrinos in red, are shown to illustrate the distribution for the benchmark annihilation of a 100 GeV WIMP to W^+W^- assuming $\langle\sigma v\rangle = 10^{-19}\text{cm}^3/\text{s}$ (enhanced with a factor of 300 in in order to be able to see it on the plot).

Table 5.1: Rates of events expressed in mHz before and after applying the level 3 cut, as well as the rate of events at level 2 that pass the DeepCoreFilter (DCFilt).

	Level 2	Level 2 (DCFilt)	Level 3
Experimental data	$\sim 2.9 \cdot 10^6$	$\sim 16.4 \cdot 10^3$	640.4
Noise events	$\sim 35 \cdot 10^3$	$\sim 6.6 \cdot 10^3$	0.1
Signal ν_μ	—	100 %	70.6 %

5. The first 3 pulses in SRT cleaned pulse series must occur within the DeepCore fiducial volume

5.6 Cut level 4

Before cut level 4, the first reconstruction algorithms are run, allowing the rejection of atmospheric backgrounds based on direction as well as adding information to better select contained events by removing long length tracks and events reconstructed far from the DeepCore fiducial volume.

5.6.1 Improved LineFit

The more advanced event reconstructions in IceCube are initiated (or *seeded*) with a qualified guess determined from more simple reconstructions. As this event selection is focused on tracks from charged current interactions of muon neutrinos, the first guess used is the *improved LineFit*: For a selected pulseseries, a coarse hit cleaning is carried out by removing pulses from photons with an apparent scattering. The

improved LineFit is a Huber fit[158] (least squares optimization with an emperically determined penalty function), fitting an infinite straight line (moving through IceCube) to the position of the DOMs with accepted pulses[159]. The improved LineFit can be used in distinguishing cascades from tracks, but with the focus on tracks in this analysis, it is simply used as a seed for the following reconstruction.

5.6.2 SPEFit4

The reconstructed values of the direction, time, speed, and position from improved LineFit are used to seed the event reconstruction *SPEFit*[160]. SPEFit is based on the time of hits in the detector, but uses only the first hit (i.e. only a single photoelectron, or SPE) on each DOM, because the subsequent hits are expected to be scattered more (assuming the first hit is not from noise). SPEFit is a likelihood-based event reconstruction algorithm, used to determine a set of parameters $\mathbf{a}$ from a set of data points $\mathbf{d}_i$. The time of the hits from an SRT cleaned pulseseries in IceCube are used to determine the most likely parameters for an infinite line moving through IceCube; the direction of the line, the propagation speed, and a point x_0 on the line (with an associated time t_0) to fix the line in time and space.

For a hypothesized track, the distance r and orientation of the DOM η is determined for each hit and the most likely track hypothesis can be determined by maximizing the likelihood:

$$\mathcal{L}(\mathbf{a}|\mathbf{d}_i) = \prod_{i}^{N_{\text{hits}}} p(\mathbf{d}_i = t_{\text{res,i}}|\mathbf{a} = r_i, \eta_i). \tag{5.1}$$

In place of the hit time, the more relevant quantity of the residual time is used

$$t_{\text{res}} = t_{\text{hit}} - (t_0 + t_{\text{direct}}) \tag{5.2}$$

Reflecting the difference between when the hit was detected, t_{hit}, and when it would arrive at the DOM if it was unscattered or *direct* through the ice, t_{direct}. Since t_{direct} depends on the position and direction of the track, t_{res} is dependent on the track hypothesis (direction, position, time, and velocity).

The probability function in Eq. (5.1) describing the arrival time probabilities given a track hypothesis is in SPEFit described by the analytical *Pandel function*[161] parametrized in terms of r and η. Ideally, t_{res} would be a delta-function around zero, but due to scattering of photons in the ice (and to a lesser degree photons from radiative losses and jitter in the electronics), t_{res} will instead be a represented by broader distribution. The Pandel function describes this broadened distribution with, basically, a Gaussian that is tuned with four free parameters (some parametrized in terms of r and η), and was initially motivated from laser studies in the BAIKAL experiment[161]. For the initial implementation for use in the AMANDA experiment, these parameters were determined in order for the Pandel function to describe the optical properties in ice rather than in water.

Since the likelihood calculations need to be carried out for all track hypotheses tested it is a large benefit that the Pandel function is an analytical expression for the arrival time distribution t_{res}. This makes the likelihood calculations fast, and the SPEFit become computationally efficient and it is therefore feasible to use at cut levels with a rate of about 1 Hz.

SPEFit is run with multiple iterations in order to lower the risk of the fit finding a local minimum instead of the global minimum of the likelihood space. The first iteration of the fit is seeded by the improved LineFit. The subsequent iterations are seeded with the previous SPEFit, perturbed by assigning a new random direction and moving x_0 along the new track to the point closest to the COG of the hits in the hit series used, while shifting t_0 such that it matches the expectation of direct light from the Cherenkov cone. In this analysis the number of iterations were kept at 4 since no significant improvements in resolutions were gained with additional iterations (observed in the previous analysis[157]). The iteration with the best (i.e. highest) likelihood value is used in the analysis. If SPEFit does not converge to one set of parameters, the event is removed from the sample which occurs for less than 0.1% of the events.

Cuts applied Using the SPEFit reconstruction, only events with a reconstructed zenith angle within 20° of the galactic center are kept. As can be seen on Figure 5.3, there is a non-negligible fraction of the background sample that has a reconstructed zenith angle above $\pi/2$, corresponding to upgoing events. At this level almost all of the background is atmospheric muons (about 1% atmospheric neutrinos), so the events above $\pi/2$ are atmospheric muons that have been mis-reconstructed. This is the main motivation for also removing upgoing events, as the events reconstructed as upgoing are still dominated by background at this level. Later a more advanced reconstruction will be run, which will identify the zenith angle to a better precision.

In addition, a cut is placed on the likelihood value excluding events with low likelihood value, (or high value of LLH $= -\ln(\mathcal{L})$). In an attempt to reconcile the fact that more hits give more terms for the calculation of LLH, and hence a higher value, the LLH value is normalized to the number of channels in a similar way to the statistical measure of the reduced χ^2 value. The definition of the reduced LLH is given as rLLH $=$ LLH$/(n_{\text{channel}} - 5)$, and though it does not carry any statistical meaning, it has been shown to work as an empirical measure of the goodness-of-fit and a way of removing events with poor fit quality.

5.6.3 Paraboloid

In addition to the cut on rLLH, a more elaborate estimator is used to gauge the event quality. The *paraboloid* algorithm fits a 2D parabola to the likelihood plane for the zenith and azimuth angle. The error ellipse enclosing the paraboloid at $\frac{1}{2}\mathcal{L}_{\text{best}}$, characterizes the angular uncertainty of the likelihood fit with two parameters σ_1 and σ_2 (major and minor axis)[162]. This is commonly implemented as a single parameter $\sigma_{\text{para}} = \sqrt{(\sigma_1^2 + \sigma_2^2)/2}$, where larger values are correlated with a worse angular resolution, cutting away events with $\sigma_{\text{paraboloid}} > 0.5$.

5.6.4 Photon tables

The SPEFit reconstruction is based on the photon arrival times for solely the DOMs that recorded a hit. A more complete form of information can be achieved by determining the probability of seeing a hit in a given DOM for a given interacting particle hypothesis.

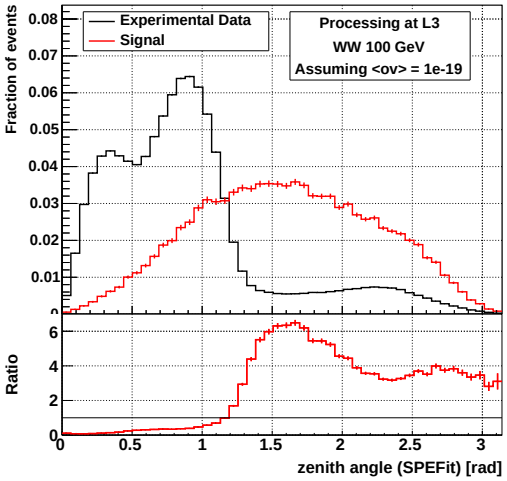

Figure 5.3: Distributions of the zenith angle from SPEFit before cut level 4 is applied, where the data in black (nearly completely dominated by atmospheric muon background at this level) is compared to the signal muon neutrinos in red (for the benchmark annihilation of a 100 GeV WIMP to W^+W^- assuming $\langle\sigma v\rangle = 10^{-19}\text{cm}^3/\text{s}$).

The photon detection probability for a given DOM is dependent on the distance to the track, the direction and length of the track, the orientation of the DOM relative to the track, and the optical properties of the ice. E.g. for muons the photon detection probabilities are determined by simulating a minimum ionizing muon starting at a given depth (between -800 m to 800 m), propagating through the ice with a given zenith angle (full range between 0-180°). From this the probabilities of detecting the Cherenkov photons are recorded out to a certain distance (depending on energy), and the distributions are parametrized in terms of time and position. This is combined with a multi-dimensional spline to smoothly interpolate across all different depths and track zenith angles. So for a given hypothetical track in IceCube, one can extract the probability that a photon should have been detected on a given DOM. These *photon tables* are exploited in advanced the reconstruction algorithms where the hypothetical track is varied in position, direction, and depth to find the most likely configuration. By comparing the expected photon distribution to the photons that are actually detected, both DOM with and without hits are adding information to the reconstruction.

One challenge that arises from using the photon tables is the added complexity from increasing dimensionality. From the updated model for the ice in IceCube, SPIce Lea, we know that the ice is anisotropic in the azimuthal direction, however the current photon tables do not include an azimuthal variation. First of all the generation of the photon tables would be non-trivial, with the additional simulation needs and a more complex multi-dimensional spline that must be ensured to interpolate smoothly between sample points. More importantly, it is already memory- and computationally-demanding to do lookups in the photon tables, adding another dimension would simply not be practically possible. As such it is simply not possible to incorporate the anisotropy into the photon tables, and analyses must therefore rely on tables generated with SPIce Mie for the reconstruction. This issue shall be discussed as a systematic uncertainty in Section 6.4.

5.6.5 FiniteReco

With the photon tables, it is possible to include the DOMs that did not see any hits, as that naturally adds valuable information. There should be no hits (caused by Cherenkov photons) before the interaction point, so the likelihood becomes more sensitive to the starting and stopping point of the track when including the DOMs with no hits. Including DOMs with no hits means adding many thousands of additional points (as most DOMs will need to be included), and if all the parameters describing the hypothesized track also need to be varied it will increase the computation time and complexity of the likelihood space considerably. At this stage of the event selection it is not feasible to use this approach, and instead the number of fit parameters for a photon table based reconstruction are limited to the length of the track, and the full parameter space shall be explored at a later cut level.

In the *FiniteReco* algorithm the direction and position of the track is given by SPEFit4, and only the interaction point and stopping point is varied to calculate the most probable length of the track. A muon track can in principle be passing through IceCube, it can be starting or stopping inside IceCube, or it can be fully contained within IceCube. The neutrino induced muons might travel many hundreds of meters through the ice before stopping, but if they start in the DeepCore fiducial volume and are downgoing the reconstructed length will be limited by the size of the fiducial volume, because there are no instrumentation below. Therefore, both the starting and stopping points shall be determined, and the length can be used as a discriminating variable.

An initial guess for the interaction vertex is determined from the SPEFit4 track, as the point where a direct Cherenkov photon would produce the hit on the DOM most upstream (i.e. DOM furthest back towards the arrival direction of the track). From this assumed interaction point FiniteReco is used to determine the most probable stopping point by varying the length of the track. In the next iteration the most probable starting point is determined in a similar way by tracing back from the established stopping point[163].

Cuts applied Demanding the track to be shorter than 600 m removes some background events while retaining most signal neutrinos, as can be seen in Figure 5.4. For the benchmark signal shown it is clear that the cut could be harder without loss of signal neutrinos, but signal neutrinos from WIMPs with a larger mass than 100 GeV will have higher energies, and their associated tracks in IceCube will be longer. So the cut ensures that the analysis is also efficient at higher WIMP masses.

In addition, a containment constraint is applied to ensure that the reconstructed interaction vertex is within 250 m from string 36, the center of the DeepCore fiducial volume, a cylinder that encapsulates all of the fiducial volume. The reconstructed interaction point will often be near the DOMs where the first light from the event was detected. Neutrinos will interact anywhere in IceCube with an equal probability, and hence the track will be reconstructed as starting anywhere in IceCube. Atmospheric muons sneaking into IceCube will predominantly be detected as they enter the fiducial volume, and hence they will more often have a reconstructed interaction point further away from the center of the detector.

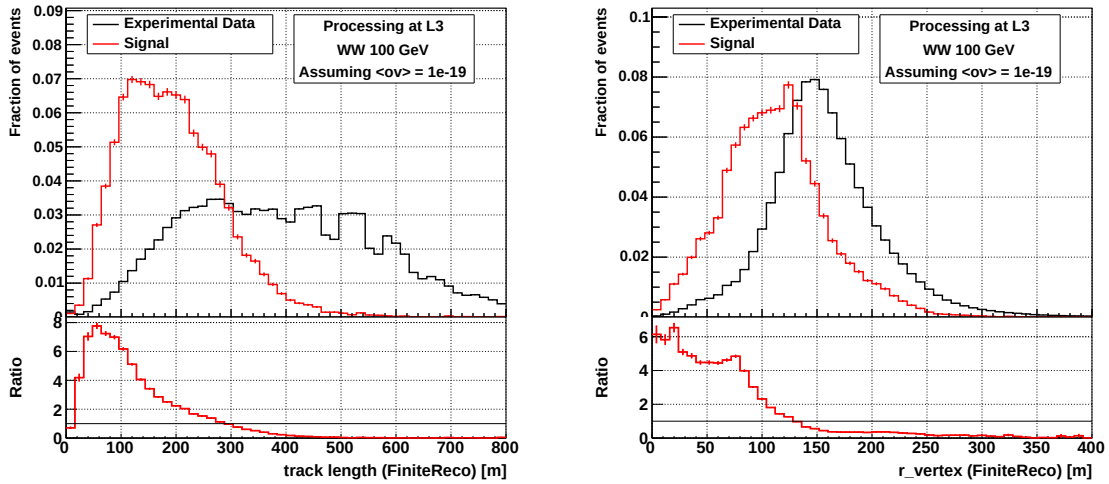

Figure 5.4: Distributions of the reconstructed length l_{FR} and radial distance from string 36 of the reconstructed interaction vertex r_{FR} (both based on FiniteReco) before cut level 4 is applied. The data in black (nearly completely dominated by atmospheric muon background at this level) is compared to the signal muon neutrinos in red (for the benchmark annihilation of a 100 GeV WIMP to W^+W^- assuming $\langle\sigma v\rangle = 10^{-19}\mathrm{cm}^3/\mathrm{s}$).

5.6.6 Spread of charge along the z-axis

The geometrical distribution of hits will ideally depend on the direction of the track, though it might be smeared out by scattering in the ice. Projecting all hits onto the z-axis and determining the charge weighted spread of charge σ_z, provides a variable constructed from only low-level detector information that can be descriptive of the zenith direction of the event. At the energies considered in this analysis the correlation between σ_z and the zenith angle is not really pronounced for neutrinos. However, an atmospheric muon sneaking into IceCube will generally have more hits further up in the detector than a signal neutrino which is why σ_z will generally be larger for atmospheric muons than for starting neutrinos. As can be seen from the corresponding plot on Figure 5.5, σ_z provides fairly good separation between the benchmark signal neutrinos and the backgrounds, and by cutting away events with $\sigma_z > 80$ most signal is kept, while removing a large amount of background.

5.6.7 Clustered hits in veto volume

After applying the cuts discussed above, an additional processing of the events is carried out. The *VetoPulses* are defined as the pulses that fulfill the following criteria:

1. is outside the fiducial volume,
2. is not in the SRT cleaned pulse series, and
3. happens before the end of the first quantile in time of hits in the SRT cleaned pulse series.

Hits in the veto volume that happen before the hits in the fiducial volume are what you expect to see from downgoing muons. The hits in the veto volume that happen

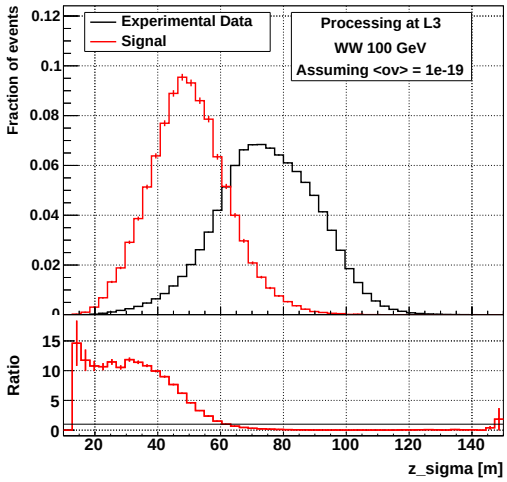

Figure 5.5: Distributions of σ_z before cut level 4 is applied, where the data in black (nearly completely dominated by atmospheric muon background at this level) is compared to the signal muon neutrinos in red (for the benchmark annihilation of a 100 GeV WIMP to W^+W^- assuming $\langle\sigma v\rangle = 10^{-19}\text{cm}^3/\text{s}$).

later than the hits in the fiducial volume are irrelevant because they cannot be related to an incoming muon. The first couple of hits in the SRT cleaned pulses might be noise hits and not related to the physics event, which is why the third criterion is included.

Each of the pulses in the VetoPulses is used to seed an iteration of SRT cleaning of the VetoPulses, and the size of the resulting cluster is saved. The number of hits of the iteration with the largest resulting cluster is used as a classifier between atmospheric muons and starting neutrinos. Keeping events with a size less than three gave the largest background rejection while retaining most of the signal neutrinos[91].

5.6.8 Data/MC agreement after level 4

In the analysis the experimental data will be used to estimate the background, which ensures that the background is correctly estimated (per definition). Comparing the simulation of atmospheric muons to data allows a cross check of the IceCube simulation framework. The best agreement of the total rates are achieved by applying the Gaisser H3a model of cosmic ray composition[151], and shall be used in the following comparisons. However, the check is focused on the shape of the distributions, ensuring that the general features are similar. On Figure 5.6 it can be seen that within the majority of the events the agreement between data and the atmospheric muon simulation is within 10% (taking the statistical fluctuations into account). The agreement between CORSIKA and data in IceCube is generally not great at trigger level, but it improves at higher cut levels such that comparisons to CORSIKA are informative. In this analysis the CORSIKA will not be used further than this cross check.

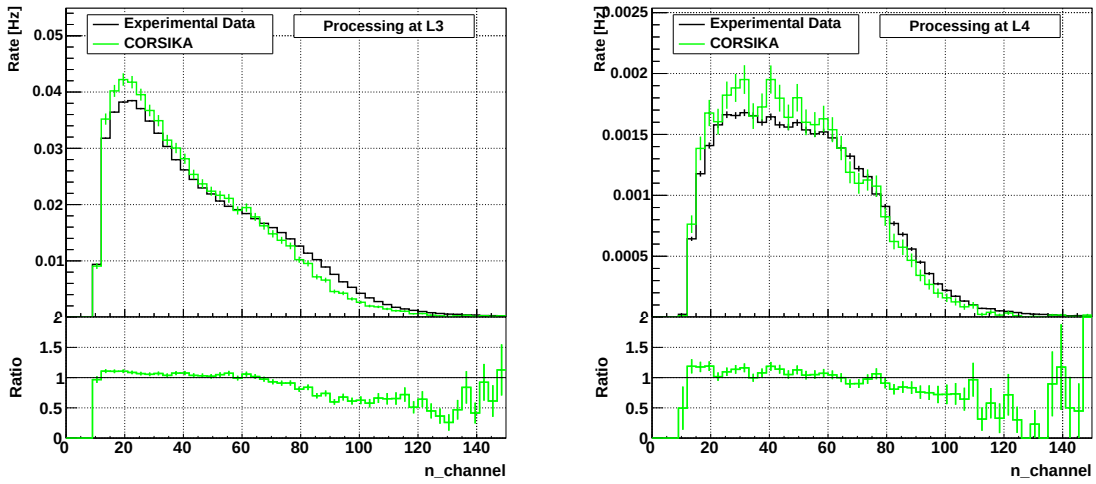

Figure 5.6: Distribution of the number of channels (number of DOMs with hits), comparing the burnsample of data (black) to the simulation of atmospheric muons (green) at cut level 3 (4) on the left (right).

Table 5.2: Rates of events expressed in mHz before and after applying the level 4 cuts. Every number is based on simulation apart from the experimental data.

	Level 3	Level 4
Experimental data	640.4	35.4
Atmospheric muons	656.9	37.9
Noise events	0.1	0.0
Signal ν_μ	100%	20.8%

5.6.9 Summary of cut level 4

After cut level 4, the experimental data is reduced by about a factor 20, and there are no pure noise events left. As presented in Table 5.2, the benchmark signal is reduced by about 80%, which is mainly due to cut in zenith.

The cuts applied at level 4 are listed below for reference:

1. $\theta^{\mathrm{SPE4}}_{\mathrm{zenith}}$ within 20° of $\theta^{\mathrm{GC}}_{\mathrm{zenith}}$
2. $\sigma_{\mathrm{paraboloid}} < 0.05$
3. $\frac{\mathrm{LLH}^{\mathrm{SPE4}}}{n_{\mathrm{channel}}-5} < 11$
4. $L^{\mathrm{FR}} < 600$ m
5. $r^{\mathrm{FR}} < 250$ m from the center of the DeepCore fiducial
6. $\sigma_z < 80$ m
7. Size of largest cluster in veto volume < 3 hits

5.7 Cut level 5

The atmospheric muons that dominate the sample at L4 are arriving from roughly the same direction as the signal neutrinos and look like starting events. At this level, additional methods of removing atmospheric muons are employed by looking for information in hits behind the reconstructed interaction vertex.

5.7.1 Constraining the zenith angle

Since the rate from atmospheric muons increases the further above the horizon one looks (for smaller zenith angles), at least around the position of the center of the galaxy, more background can be rejected by further constraining the zenith angle. In the experimental data there is still a significant fraction of events with a reconstructed zenith more than 10° above the galactic center, compared to the signal neutrinos. By applying the cut to the events, about 25% the atmospheric background is removed, while losing about 15% of the signal.

5.7.2 ConeHits

So far the event selection have relied on the SRT cleaned pulses series, however, some of the hits from an incoming muon might have been cleaned accidentally, but by looking into the full set of pulses that information can be retrieved. By looking at the full set of pulses possible information can revea, by looking into the full set of uncleaned hits, A cone with am opening angle of 20 degree is oriented back from the reconstructed interaction point towards the reconstructed incoming direction of the track. Looking at all pulses in the event (no cleaning applied), the number of pulses within a 1 μs time window starting 0.5 μs after the reconstructed interaction time is counted as the number of *ConeHits*. For atmospheric muons the number of ConeHits are expected to be non-zero, whereas for truly starting tracks it should be zero. As individual noise hits might be within the cone, one can not reject all events with a non-zero number of ConeHits. Looking at the distributions of signal and background (see Figure 5.7), a cut at less than 2 hits was employed which retains 99% of the signal neutrinos. The settings of the time window can be varied, but no significant increase in the performance was observed in doing so.

5.7.3 Likelihood of hits in veto volume

A cylinder with a given radius is extended backwards from the reconstructed interaction vertex, and all the pulses within the cylinder which are not part of the SRT cleaned pulse series are determined as the *CylinderHits*. The likelihood calculation used in SPEFit is used to determine the likelihood value of the reconstructed track given only the CylinderHits. For starting tracks the CylinderHits should be dominated by noise, whereas for atmospheric neutrinos there might be hits that compares well to the fitted track. So for truly starting tracks the likelihood value should be low, whereas atmospheric muons (with hits behind the reconstructed vertex) would have a better likelihood value. Starting with a cylinder radius of 250 m, events with $-ln(\mathcal{L})/(n_{\text{channel}}-5) < 18$ are cut away, which retains about 90% of the signal neutrinos. The value is motivated from the observation that it retains most

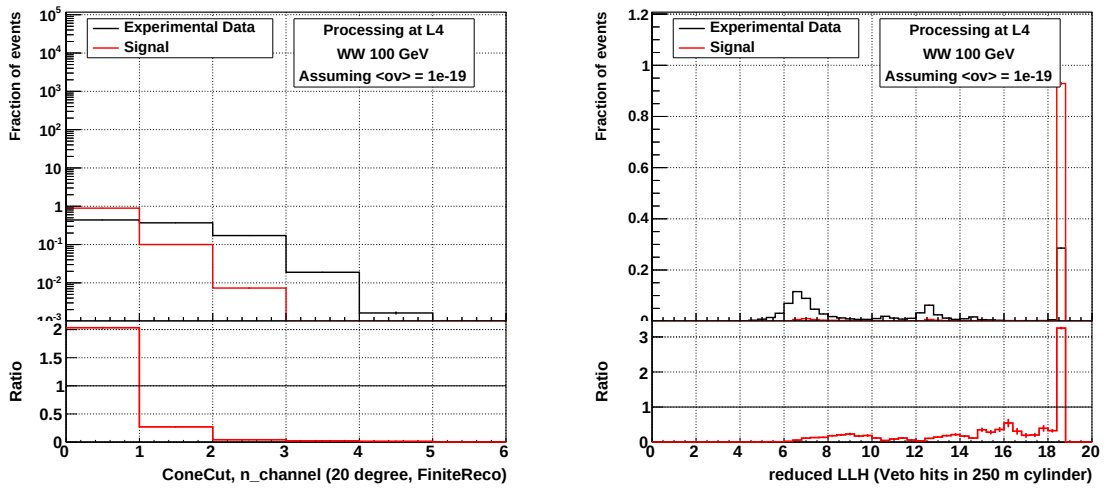

Figure 5.7: Left: Distributions of the ConeHits. Right: The $-ln(\mathcal{L})/(n_{\text{channel}} - 5)$ of the reconstructed track using only hits in a 250 m cylinder behind the reconstructed interaction point. Both distributions are shown before the cuts at level 5 are applied. The data is presented in black (still dominated by atmospheric muon background) and compared to the signal muon neutrinos in red (for the benchmark annihilation of a 100 GeV WIMP to W^+W^- with $\langle\sigma v\rangle = 10^{-19}\text{cm}^3/\text{s}$).

signal, as can be seen on the right panel of Figure 5.7. Subsequently, larger radii at 300 m and 350 m are run with weaker cuts of $-ln(\mathcal{L}) < 11$ and $-ln(\mathcal{L}) < 6.8$, respectively, using values estimated in the previous analysis[157]. Compared to the ConeHits, there is no time constraint imposed on the CylinderHits, so there might be more than one pulse in this set even after the cut on ConeHits.

5.7.4 Cut in the radius and depth

Most of the atmospheric muons sneaking into the DeepCore fiducial volume are reconstructed to be starting further away from the center of the fiducial volume, whereas the signal neutrinos will interact more or less uniformly throughout the volume. The radius r_{FR} describes the distance in the $(x-y)$-plane, and instead of using the z-position of the reconstructed interaction vertex it was observed in the previous analysis that the earliest hit in the SRT cleaned pulseseries, $z_{\text{first DOM hit}}$, gave a stronger separation[157]. In the right panel of Figure 5.8 a change at the depth of -300 m can be seen for signal neutrinos, which gives the possibility to reject a good fraction of atmospheric muons in data.

A cut is implemented in the 2D space of the two variables, such that the cut traces out the kink seen in signal neutrino, while excluding the large fraction of atmospheric background that can be seen in the region of $r_{\text{FR}} = 150$ and $z_{\text{first DOM hit}} = -200$. The value were determined in the previous analysis[157] resulting in the following cut:

$$r^{\text{FR}} \leq \begin{cases} 160 \text{ m} & , \text{ if } z_{\text{first DOM hit}} \leq -300 \text{ m} \\ -\frac{z_{\text{first DOM hit}} - 80}{2.333} & , \text{ else} \end{cases} \tag{5.3}$$

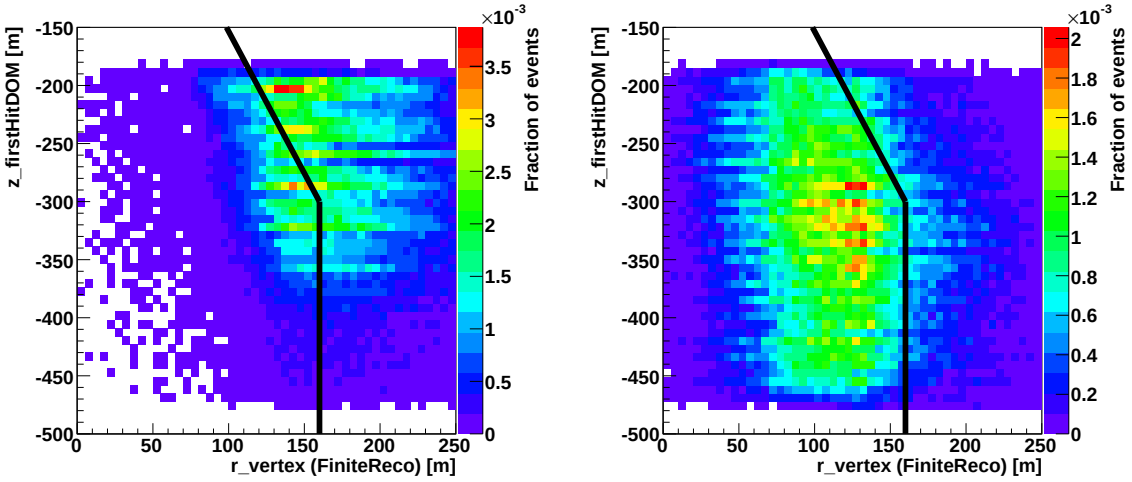

Figure 5.8: 2D-distribution of the radial position of the reconstructed interaction vertex and the depth of the DOM with the earliest hit from the SRT cleaned pulse series for background (signal) on the left (right) plot. Events to the right of the solid black line are discarded.

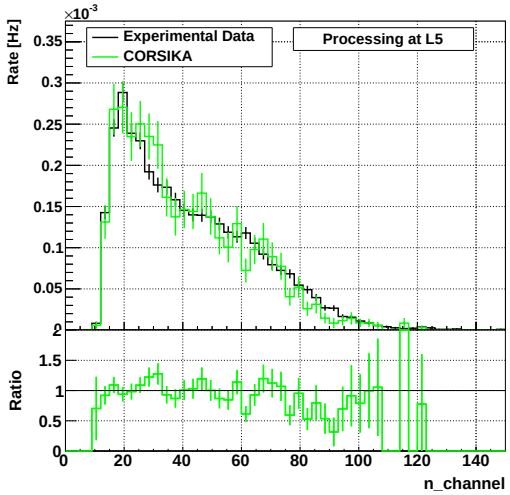

Figure 5.9: Distribution of the number of channels (DOMs with hits) at cut level 5, comparing the burnsample of experimental data (black) to the simulation of atmospheric muons (green).

5.7.5 Data/MC agreement after level 5

Since the simulated atmospheric muon background shall not be used to derive the final results, no computing time has been spent to process it all the way to final level. So the check at level 5 before the multivariate selection constitutes the final discussion of the data to MC simulation (dis)agreement. From Figure 5.9 it is clear that the statistics of the data set with atmospheric muons is low, even though more could be generated/processed if it was needed for the final analysis. Beneath the statistical fluctuations the two datasets agree to within 10%, indicating that an analysis that was dependent on the simulation of atmospheric muons could arrive at a sample that represents experimental data well.

Table 5.3: Rates of events expressed in mHz for some of the components before and after applying the level 5 cuts.

	Level 4	Level 5
Experimental data	35.4	3.5
Atmospheric muons	37.9	3.6
Signal μ_ν	100%	63.4%

5.7.6 Summary of cut level 5

After cut level 5 the atmospheric muons have been removed by identifying them as penetrating muons by using the information from hits in the veto volume have been removed. The experimental data is reduced with about a factor of 10, while about 60% of the benchmark signal neutrinos are retained, as presented in Table 5.3 and the use of cuts in multiple dimensions are starting to become necessary.

The cuts applied at level 5 are listed below for reference:

1. $\theta^{\text{SPE4}}_{\text{zenith}}$ constrained further to at most 10° above $\theta^{\text{GC}}_{\text{zenith}}$
2. Less than 2 hits within a 20° cone behind the reconstructed interaction vertex
3. Poor goodness-of-fit of track to hits in the veto volume behind the reconstructed interaction vertex, $\ln(\mathcal{L})/(n_{\text{chan}} - 5) < 18$
4. Cut in the 2D plane of radius and depth, see Section 5.7.4

5.8 Level 6 variables

At this level of the event selection it is becoming increasingly difficult to find variables that alone offer good separation between the signal neutrinos and the atmospheric background. By considering multiple variables at the same time, new possibilities for separation become available, therefore the multivariate analysis technique of boosted decision trees[164] (BDT) shall be trained and applied as the final step in the event selection.

Since the purpose of the BDT is to pick out dataset specific features, it is important that the selected features are not due to errors in the simulation. At lower level where the agreement between simulation and experimental data might not be appropriate for a multivariate analysis, straight cuts are used. Having ensured that there is a reasonably good agreement between experimental data and simulation at L5, the BDT is expected to pick out physics differences between background and data, rather than discrepancies between the production of them.

The variables used in the BDT are presented in this section, and the method, strategy and investigations of the BDT will be presented in the next section. A choice was made of using only the seven most important variables, as at that point the increase in sensitivity was small when adding more variables. The choice was done as a trade off between a better sensitivity versus higher complexity of the BDT.

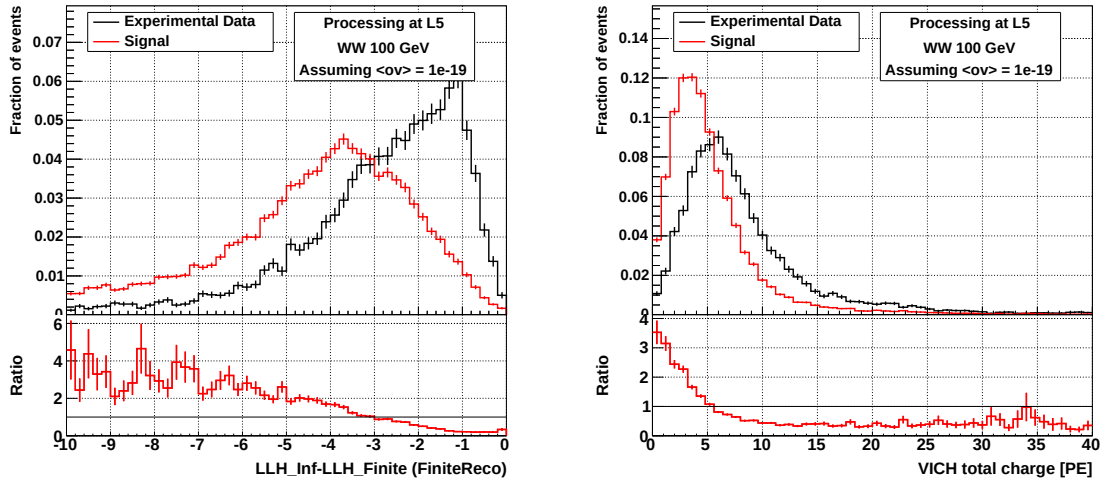

Figure 5.10: Distributions of the likelihood ratio represented as the LLH difference $\ln\left(\mathcal{L}^{\text{FR}}_{\text{contained track}}\right) - \ln\left(\mathcal{L}^{\text{FR}}_{\text{infinite track}}\right)$ and the total charge of VICH hits at level 5. The data is presented in black (stil nearly completely dominated by atmospheric muon background) and compared to the signal muon neutrinos in red (for the benchmark annihilation of a 100 GeV WIMP to W^+W^- assuming $\langle\sigma v\rangle = 10^{-19}\text{cm}^3/\text{s}$).

5.8.1 Comparison between finite and infinite track

In the evaluation of FiniteReco (at level 3), the most likely length of the track is determined. When running FiniteReco both the likelihood value for the contained track, $\mathcal{L}^{\text{FR}}_{\text{contained track}}$, and the likelihood for an infinite track with corresponding direction, $\mathcal{L}^{\text{FR}}_{\text{infinite track}}$, are calculated. By taking the ratio of the likelihood values (or subtracting the logarithm of the values) one arrives at a measure for which of the two hypotheses are most likely for a given event. This quantity is presented in Figure 5.10

Not using a more precise reconstruction? One should think that stronger separation of background and signal can be gained by applying the same strategy to results from the more advanced reconstruction (presented below). However, that turned out to not be the case, and using FiniteReco simply gave a slightly better separation. Even though the two reconstructions did not lead to dramatically different distributions, studies confirmed a difference in separation power.

5.8.2 Veto identified causal hits (VICH)

At this stage of the analysis, any extant muons will likely have left some small number of hits while traversing the veto region of the detector. The Veto Identified Causal Hits (VICH) and CorridorCut algorithms are filters designed to identify these rare hits which are causally connected with the observed hits in DeepCore. For the veto identified causal hits (VICH) algorithm the initial hit that fulfilled the trigger condition (effectively the hit with the same time as the trigger) is used as the starting point. Then the geometrical distance $d = |\mathbf{r}_{\text{trig}} - \mathbf{r}_i|$ and the time difference $\Delta t = t_{\text{trig}} - t_i$ to all other hits in the uncleaned hit series are calculated.

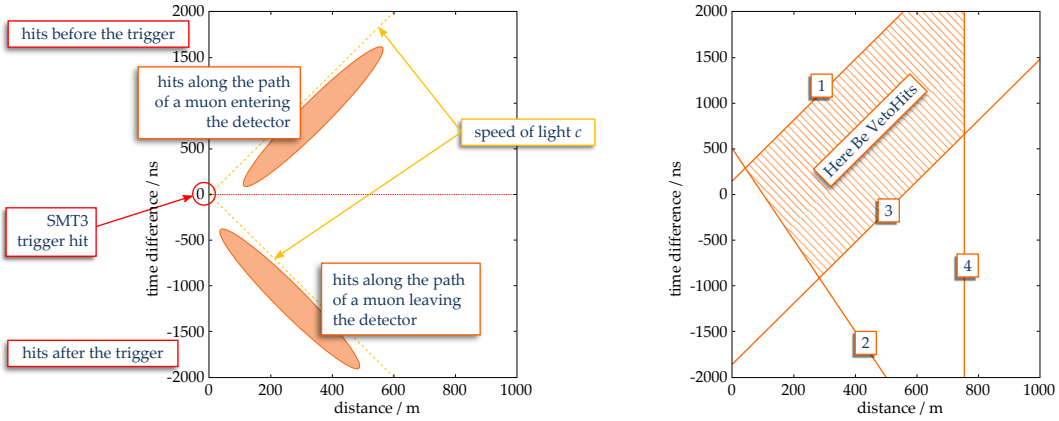

Figure 5.11: The idea of the Veto Identified Causal Hits (VICH) is presented in the left panel. In the right panel, the implementation of VICH is illustrated with the position of the lines discussed in the text. Figure from Ref. [156]

The idea of the cut is presented on the left panel of Figure 5.11. An incoming muon traveling at with the speed of light would produce hits along the line $\Delta t = d/c$ (*line 1*) while any scattered photons will correspond to Δt below this line. Any outgoing track would produce hits along the line $\Delta t = -d/c$ (*line 2*), or below if the photons get scattered. The signal neutrinos would have hits below line 2, but not below line 1, so the veto identified causal hits (VICH) between the two lines identify incoming atmospheric muons. In order to make the VICH algorithm more powerful, the position and slope of the lines has been optimized in a previous IceCube analysis using the DeepCore fiducial[156] and the resulting lines are presented on the right panel of Figure 5.11. In addition, the VICH are constrained to happen within 750 m from the trigger hit and no later than 2 μs after the expectation governed by line 1.

The number of channels and the total charge of the VICH are related, but both provide separation power in the BDT independent of each other. In Figure 5.10 the distribution of the total charge of the VICH at level 5 is presented.

CorridorCut Due to the repeating triangular layout of the nominal IceCube strings there are corridors where a muon can enter unobserved by passing between two rows of strings. In that case it will only be detected once it nears the DeepCore fiducial volume. These sneaking muons can only be identified if the track can be related to any individual hits on outer strings. The *CorridorCut* algorithm specifically looks at the corridors from the string with the largest deposited charge, and counts the number of hits causal to a hypothetical incoming track[165]. However, among the other variables discussed it turned out not to be one of the seven most important variables, and was therefore not used in the BDT.

5.8.3 HybridReco/MultiNest

The event rate of the experimental data has now decreased to a few mHz and it is now feasible to run the first full likelihood reconstruction based on photon tables that fit all relevant parameters. For the implementation used in this analysis, 8 pa-

rameters were fit; the direction (zenith and azimuth), the position of the interaction vertex (x, y, z, t), the length of the track L, and the energy of the hadronic cascade E_{cascade}. With this choice of fitting parameters the fit can also handle reconstruction of cascade topologies in IceCube, as that would simply favor a track length of zero.

In the same way as for FiniteReco, both DOMs with and without hits are included in the likelihood calculation in order to exploit the complete information in an event. *HybridReco* is the newest implementation of this complete reconstruction using the photon tables (discussed in Section 5.6.4). With 8 parameters that can be varied and more than 5000 data points (one for each DOM in IceCube) this task becomes quite challenging and computationally time consuming.

The HybridReco fit begins by selecting a fit hypothesis consisting of all eight dimensions (x, y, z, t, L, zenith, azimuth, $E_{cascade}$). For this hypothesized particle, the light output and flux at each DOM must be calculated from each segment of the proposed muon track in steps of a few nanoseconds per evaluation. This is performed through the use of the photon tables, which tabulate the detection probabilities of each DOM given the position and direction of an emitting light source. The tables must account for different depths, corresponding to the varying properties of the ice medium.

The photon tables must be queried for each DOM and each 15 meter segment of track in order to find the expected charge contribution on each DOM in the detector. The expected charge for each DOM at each time is then compared to the observed hit pattern in the event, giving a total likelihood for the hypothesis.

While a single evaluation of the table is relatively inexpensive, the thousands of evaluations for each hypothesis result is a significant computational burden. The complex likelihood space further requires many iterations in the fit in order to converge.

MultiNest minimizer In order to map out, navigate, and minimize the complicated 8 dimensional likelihood landscape used in the HybridReco fit, the Bayesian inference tool *MultiNest*[166] is employed. Designed to tackle multi-modal distributions, it maps out a given space by (at least one) hyper-ellipsoid spanned by a number of active points. As the algorithm runs, it removes the point with the lowest likelihood and samples from the ellipsoid(s) until another point with a higher likelihood value is found[166]. This is repeated until a converge criteria is satisfied.

For the reconstruction of IceCube events this is a very time consuming task, with a typical reconstruction time between 20-40 minutes per event. This minimization is stopped if it runs for longer than one hour, since the resolution does not increase significantly by running it for longer. No investigations were made to determine the most optimal wall time for the reconstruction. However, this also means that the algorithm potentially is not allowed the time needed to find the global minimum, hence running the algorithm again might result in a different best fit. The variability of HybridReco/MultiNest shall be discussed in Section 5.12.2.

Resolution improvement The resolution for the reconstructed variables are determined from simulation, where the true value of the parameters are known. In Table 5.4 the mean of the differences between the value of the reconstruction and the true value are presented for the most relevant variables using the benchmark

Table 5.4: Resolution comparison for various parameters, presenting the mean $\pm\sigma_{\mathrm{RMS}}$ for the SPEFit4 reconstruction and HybridReco/MultiNest on a NuGen sample weighted to the benchmark signal (annihilation of a 100 GeV WIMP to W^+W^- assuming $\langle\sigma v\rangle = 10^{-19}\mathrm{cm}^3/\mathrm{s}$).

	SPEFit4	HybridReco/MultiNest
zenith [rad]	0.0 ± 0.3	0.0 ± 0.3
azimuth [rad]	0.0 ± 0.4	0.0 ± 0.3
x [m]	-1.7 ± 48.7	1.1 ± 23.6
y [m]	3.5 ± 49.8	-2.4 ± 25.2
z [m]	17.2 ± 29.2	-3.8 ± 14.9
length [m]	78.4 ± 70.6	-14.4 ± 50.4

signal of a NuGen sample used for the initial design of the event selection. The uncertainty presented is the spread of the distribution, giving a measure of the resolution, while the mean provides some information about the accuracy of the two reconstructions. From HybridReco/MultiNest a significant gain in resolution on the interaction vertex is achieved, higher precision for the length of the muon, and a slight improvement in the resolution on the arrival direction. It is ultimately the azimuthal direction that will be exploited in the analysis, and even though there is not too much of an improvement in terms of that quantity, the improvement on the other variables provide better information for the BDT. Hence, the atmospheric background can be rejected more efficiently, and for one iteration of the BDT a 20% better signal retention for a 10% background contamination was achieved by using HybridReco/MultiNest reconstruction instead of SPEFit4.

Better separation using y than x The remaining incoming atmospheric muons will often be detected when they enter DeepCore and hence be reconstructed as starting somewhere along that rim around the denser string configuration, which can be seen in Figure 5.12 for background. Conversely, the signal neutrinos have interaction points reconstructed fairly uniformly over the DeepCore volume (with maybe some preference closer to the position of the strings). This is why the position of the reconstructed interaction point is a good separator, and the radial position of the reconstructed vertex is included in the BDT, due to the radial symmetry of the separation (which can be seen on Figure 5.14).

Additionally, many events in the experimental data are reconstructed with an interaction point at the negative y-values. More precisely, the events in the 4th quadrant of the plot correspond to muons sneaking in with azimuth angles in the interval of about $[3\pi/2, 2\pi]$, which is confirmed by looking at the distribution of reconstructed azimuth angles, where a spike is present for the same interval as can be seen in Figure 5.13.

The increase in the rate for this azimuth interval is likely caused by the fact that the number of strings surrounding the denser string configuration (the veto thickness) is only about 4 within the interval, compared to about 5 for the rest of the azimuth angle. The result is a weaker veto volume in that quadrant, which in turn explains why y provides a better separation of background from signal than x.

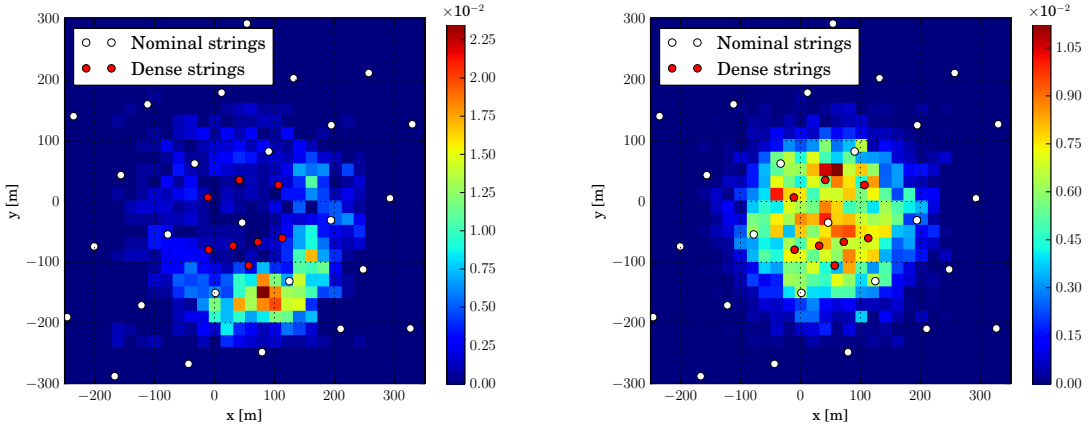

Figure 5.12: Overhead view of IceCube with the 2D distributions of the position of the reconstructed vertex position in the $(x-y)$-plane for the background sample (signal neutrinos) on the left (right) shown at level 5 for events with a reconstructed energy between 100-200 GeV. The figures show the difference between the reconstructed interaction points of incoming muons compared to signal neutrinos, shown here for the benchmark annihilation of a 100 GeV WIMP to W^+W^- assuming $\langle\sigma v\rangle = 10^{-19}\text{cm}^3/\text{s}$.

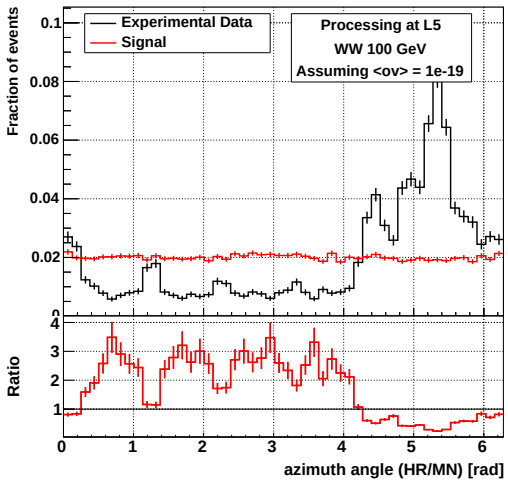

Figure 5.13: Distribution of the reconstructed azimuthal angle from HybridReco/MultiNest at level 5. The data is presented in black (still dominated by atmospheric muon background) and compared to the signal muon neutrinos in red (for the benchmark annihilation of a 100 GeV WIMP to W^+W^- assuming $\langle\sigma v\rangle = 10^{-19}\text{cm}^3/\text{s}$).

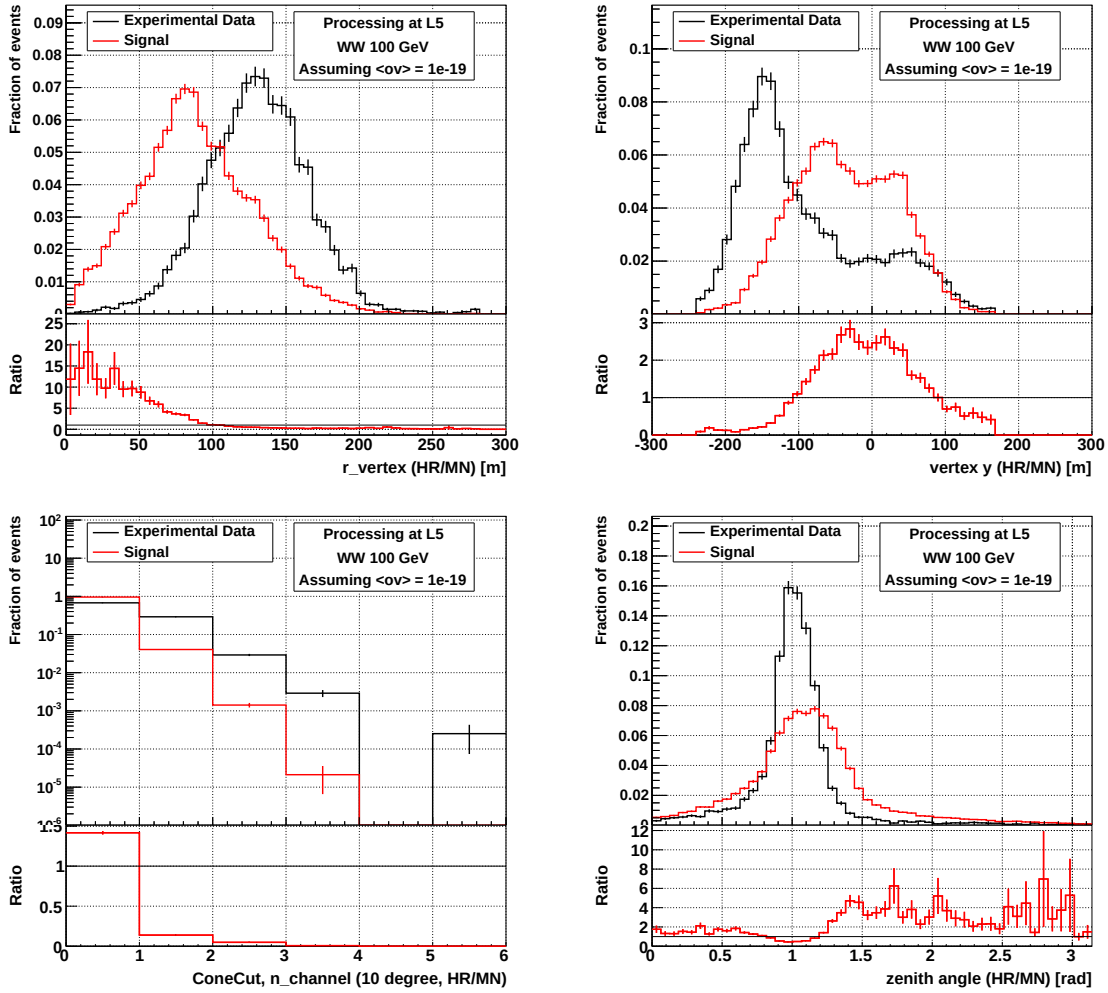

Figure 5.14: Distributions of varies quantities from HybridReco/MultiNest that go into the BDT at level 5. The data is presented in black (still dominated by atmospheric muon background) and compared to the signal muon neutrinos in red (for the benchmark annihilation of a 100 GeV WIMP to W^+W^- assuming $\langle\sigma v\rangle = 10^{-19}\text{cm}^3/\text{s}$).

5.8.4 Updated ConeCut

Using the track from MultiNest/HybridReco, the idea of the ConeHits is revisited. With a more precise reconstruction the cone more accurately covers the relevant space behind reconstructed interaction point. Cones with a 5°, 10°, 20°, and 50° opening angle were tested, because in principle the opening angle is used to cover a possible slight mismatch of the direction, and is expected to be related to the resolution of a given event. However, in practice the events in the sample span various energies, and as the resolution changes with energy (getting significantly worse at lower energies) the opening angle would have to change with energy, but the BDT is intended to be minimally effected by the energy of the signal neutrinos corresponding to different WIMP masses. In order to have a single BDT covering all WIMP masses, a cone with a fixed opening angle was chosen, and best separation was achieved with an opening angle of 10°, presented on Figure 5.14.

5.9 Prioritized list of variables at level 6

In the list below the variables are presented in order of BDT 'importance', i.e. how often the variable is used in the BDT (see next section).

- VICH, Total charge
- $r^{\mathrm{MN/HR}}$
- ConeHits (10°) using MN/HR track
- VICH, Number of channels
- $y^{\mathrm{MN/HR}}$
- $\ln\left(\mathcal{L}^{\mathrm{FR}}_{\text{contained track}}\right) - \ln\left(\mathcal{L}^{\mathrm{FR}}_{\text{infinite track}}\right)$
- $\theta^{\mathrm{MN/HR}}_{\text{zenith}}$

5.10 Multivariate analysis tool - the boosted decision tree

The boosted decision tree (BDT) is a supervised machine learning algorithm which can be used for classifying events as either signal or background. The machine learn from repeated iterations of the selection process, which is supervised by informing the machine which events are signal and which are background. The BDT uses the technique of decision tree with a boosting that puts more focus on misclassified events in subsequent iterations.

In a *decision tree*, events are classified as either signal or background by a linear cut on the variable that provides the best separation. Starting from one cut, or *leaf*, the sample is cut at multiple subsequent nodes, until a user defined tolerance is reached. The events classified as background at a given leaf are not discarded, but are classified further at the next leaf with a cut on a different variable. In the end the events is given a *BDT score* equal to the signal fraction in the final leaf.

This process is run over multiple iterations, where each new decision tree is employing *adaptive boosting* weighting misclassified events higher than correctly classified events. The weight α is calculated from the *misclassification error* (fraction of wrongly identified events in the leaf for that event) as $\alpha = 1/(\text{misclassification error} - 1)$[164].

The process of dividing the multidimensional parameter space into signal and background regions is optimized using a *training sample* of events randomly selected from the sample of neutrino signal and experimental data, still dominated by atmospheric muon background. The BDT method is implemented using the multivariate analysis tool package TMVA[167].

The separation of boosted decision tree (BDT) can be improved using a larger number of subsequent nodes, it's *depth*, and by doing more iterations (larger number) of trees. However, increasing the depth and/or number of tree also makes the BDT more prone to statistical fluctuations of the (often) limited training sample, instead of more general features. This *overtraining* can lead to a significant drop in the separation of the actual sample, and should naturally be avoided. For this reason the recommendation is to use a relative shallow tree with no more than 3-4

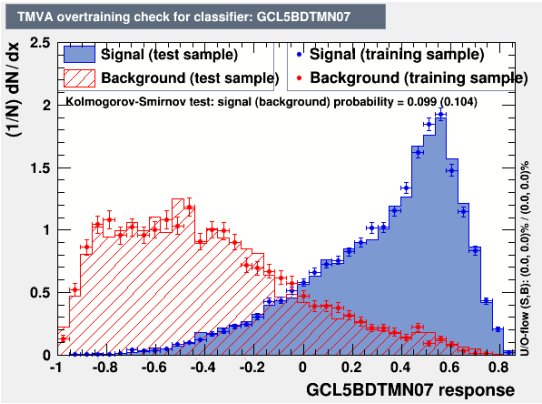

Figure 5.15: Distribution of the BDT score of the background (expected from experimental data) and the benchmark signal (annihilation of a 100 GeV WIMP to W^+W^- assuming $\langle\sigma v\rangle = 10^{-19}\text{cm}^3/\text{s}$) showing both the training and testing sample, demonstrating a fairly good agreement.

levels, and train not much more than about a hundred trees[167], implemented in this work.

5.10.1 Overtraining checks

Overtraining can be studied by comparing the separation of the training sample with an independent *testing sample*. If overtraining is not an issue the testing sample should perform nearly as well as the training sample. This is often done by comparing the distribution of BDT values from the training and testing sample, often done by eye, looking at a distribution like the one on Figure 5.15. However, in order to more systematically check the performance of the BDT and the effect of varying the depth and number of trees, it is beneficial to look at the ROC-curve of the selection. Plotting out the fraction of background and signal for a given cut on BDT score, the ROC-curve shows the separation of the two samples, and is an additional way to check for overtraining. In Figure 5.16 the ROC-curves for the training and testing sample are presented for the BDT used in this work, when varying the number of trees used. Presented is both the situation when either 1% or 10% of a full year of experimental data is used as the background sample, of which one half is used for training, and the other for testing. For the 1% sample, one can see that as more trees are added to the BDT the separation in the training sample becomes better, as more and more of the features of the distributions are identified. However, it becomes clear from looking at the separation of the testing sample that those features must be unique to the training sample as the separation in the testing sample gets correspondingly worse. So not only is the separation expected by the training sample incorrect, the actual separation also gets worse. For the 10% sample this problem is much reduced, and instead one see that the performance of both samples are slightly increasing with the number of trees.

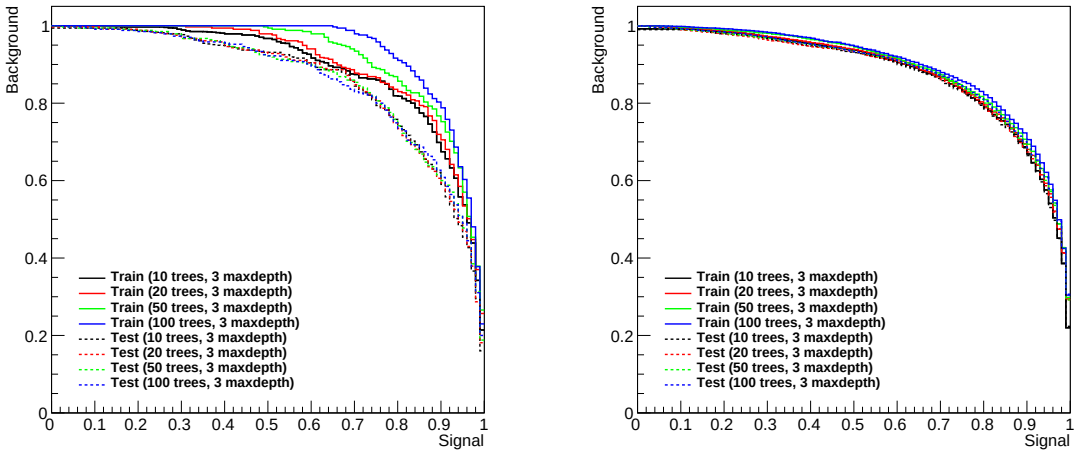

Figure 5.16: ROC-curve for BDT used in this work with different number of trees using a experimental dataset of 1% (10%) of a full year for background estimation presented on the left (right). Half of the events are used in training the BDT, and the other half is used for testing. It is seen how the 1% background sample is so small that the BDT starts training on statistical fluctuations, resulting in an actual separation in the testing sample that is much worse than expected from the training sample. Conversely, when the training sample is large enough the ROC-curves of the training and the testing sample follow each other very well, demonstrating that there are no obvious problems with overtraining.

5.10.2 Determining the BDT cut value

The optimal BDT value to cut on is determined such that the resulting sensitivity in the final analysis is as good as possible. How the sensitivity is determined shall be discussed in the following chapter, but the discussion of the effect of the choice of BDT score cut value shall be included here in order to finalize the event selection. From Figure 5.17 it is seen that using a cut value above about 0.25 does not improve the sensitivity significantly. Above that value more background is rejected, but also more signal is rejected until the statistics are too low to reliably determined the sensitivity. Since the sensitivity is not increasing for higher values anyway, it was chosen to apply a cut at a BDT score of 0.25.

5.11 Event rates and effective area

Throughout the event selection the purpose is to reduce the background and arriving at a sample with an enhanced fraction of signal neutrinos. In Table 5.5 the resulting rates for the various sets of experimental data and simulated datasets are presented. The signal neutrinos are presented for the benchmark signal (annihilation of a 100 GeV WIMP to W^+W^-) and assuming $\langle\sigma v\rangle = 10^{-19}\text{cm}^3/\text{s}$ (three orders of magnitude above the current best limits from neutrinos), which provide a normalization for the values. Hence, the rates for the signal neutrinos should be compared across flavors and cut levels, but should not be compared to the rates from the other components.

One feature worth pointing out is that the tau neutrino rate is less than half that

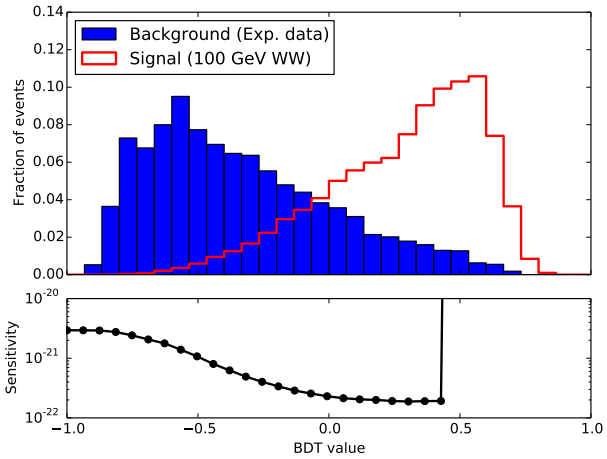

Figure 5.17: Distribution of the BDT value of the background (expected from experimental data) and the benchmark signal (annihilation of a 100 GeV WIMP to W^+W^- assuming $\langle\sigma v\rangle = 10^{-19}\text{cm}^3/\text{s}$). Bottom show the sensitivity achieved by cutting away event with BDT values below that given value.

Table 5.5: Event rates given in mHz for various components going through the analysis, where signal neutrinos are weighted to the benchmark signal (annihilation of a 100 GeV WIMP to W^+W^-) and assuming $\langle\sigma v\rangle = 10^{-19}\text{cm}^3/\text{s}$ to provide a normalization. In the table everything but the experimental data is based on simulation. The rates of the atmospheric muons are assuming the GaisserH3a energy spectrum[151], and is not processed past L5. The rates for the atmospheric neutrinos are based on Ref. [98], and due to vanishing rates at higher levels the atmospheric ν_τ are not listed. The rates presented at L2 are the rates of events that pass the DeepCoreFilter (DCFilt).

Dataset	L2 DCFilt	L3	L4	L5	L6
Experimental data	$\sim$ 15 Hz	655.0	36.73	3.59	0.27
Atmos. μ (H3a)	$\sim$ 9.5 Hz	656.9	37.88	3.53	—
Signal ν_μ	39.81	28.06	5.84	3.70	2.47
Signal ν_e	33.44	27.19	3.66	2.32	1.66
Signal ν_τ	14.96	12.06	1.59	1.09	0.88
Atmos. ν_μ	6.49	2.14	0.319	0.199	0.07
Atmos. ν_e	2.06	0.43	0.043	0.027	0.01
Noise only events	$\sim$ 6.6 Hz	0.1	0	0	0

of the other flavors. This is due to the charged-current interaction cross section of tau neutrinos being lower because of the mass of the tau lepton causing a significant effect at energies below 50 GeV. As the signal neutrinos are here shown for the 100 GeV WIMP mass, this difference in rates is expected. The data set of simulated atmospheric muons is not used in the final analysis and is therefore not processed further than level 5.

For completeness the effective areas are calculated at final level and presented in Figure 5.18. The lower charged-current cross section of tau neutrinos at lower energies, becomes rather clear and asymptotically approaches the other flavors at higher

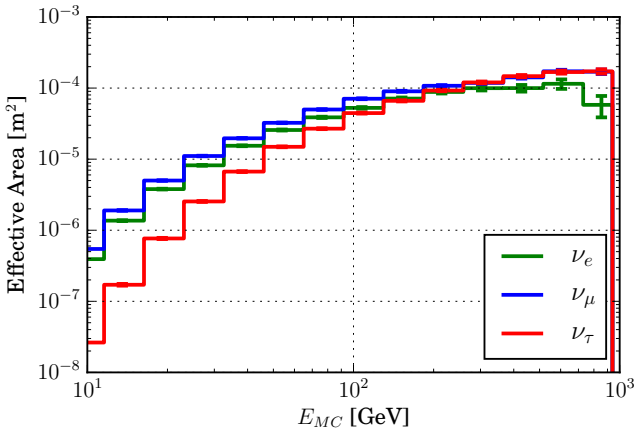

Figure 5.18: Calculated effective area for this analysis, presented for the three neutrino flavors.

energies. The drop off of the electron neutrinos seems to be statistical fluctuations with underestimated error bars (will be updated).

5.12 Final data properties

At level 6 the data selection is complete and ready to be analyzed for a galactic WIMP annihilation signal. In this section the properties of the final selection shall be discussed.

5.12.1 Final resolution

For the analysis the most important information needed from each event is the arrival direction. In the simulated datasets the true direction of the simulated neutrino can be compared to the reconstructed direction, and the difference between the two determines the resolution of the reconstruction. In Figure 5.19 the median difference is presented for the muon neutrino sample along with the inherent limit from the kinematic opening angle. The zenith angle is generally better resolved than the azimuth angle for low energy events, as it can be constrained from hits on fewer strings. Going up in energy the median resolution settles at a few degrees (slightly worse in azimuth), following the kinematic opening angle fairly well. At higher energies there are fewer events generated, and statistical fluctuations can be observed on the median resolution at higher energies.

The resolution is never as good as one might desire, as a higher resolution will be beneficial in the search for a signal. The resolution could be improved by applying a more strict event selection, but a trade off must be made between resolution and number of events, and limiting the statistics for this analysis beyond what has already been done would only worsen the sensitivity.

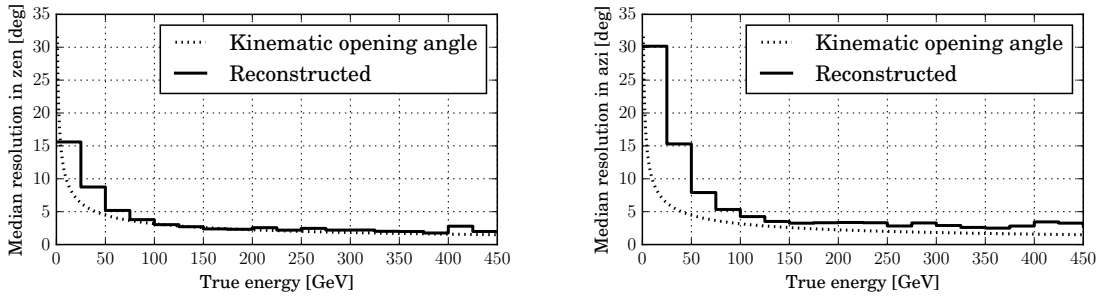

Figure 5.19: Resolution of final event sample of muon neutrinos as a function of true energy, for the zenith angle (azimuth angle) on the left (right).

5.12.2 Variability of HybridReco/MultiNest

After finalising the event selection it was discovered that HybridReco/MultiNest behaves non-deterministic with respect to the reconstruction values. That means that if it is run again on the same event, it produces different results.

This is driven by the fact that the seed for the random generator can not be controlled in the current implementation of the algorithm. Secondly, the likelihood space is complex with frequent equivalent local minima. The algorithm is inherently deterministic, but since the seed for the random number generation will be different every time the algorithm is run, and if the process is terminated before the global minimum is found, HybridReco/MultiNest will generally produce different values for the reconstructed variables every time it is run.

In the left panel of Figure 5.20 the effect is demonstrated for five randomly chosen events, showing the variation in the reconstructed values by reconstructing each event 100 times. The stars indicate the true value, and though a perfect match would be great, the important part is that the distributions are unimodal and seem to favor a single best fit value with some uncertainty The standard deviation of the 100 reconstruction of the same variable is calculated and used to quantify the variability or *volatility* of HybridReco/MultiNest. In the right panel of Figure 5.20 the distribution of the volatility on azimuth for 1000 random events are presented, with a mean value across all energies of about 23 degrees.

In the left panel of Figure 5.21 the volatility of 1000 muon neutrinos reconstructed 100 times is compared to the median resolution of the muon neutrinos as a function of energy. It shows an effect that is at least of the same order as the resolution itself, and gives a sense of the effect of the volatility compared to the resolution. A check was made to ensure that the sample of 1000 events is large enough to be representative of the full sample, in terms of judging the effect of the volatility. It was established that the median resolution of the 1000 events, estimated across the 100 reconstructed values, is consistent with the resolution of the entire sample where each event is only reconstructed once. This indicates that the volatility does not add to the general resolution, but as it will be an inherent effect for the reconstruction a given event might be reconstructed with a worse resolution in one run of the reconstruction and a good value in the next, but the effect appears to average out over large enough samples.

For experimental data there are no information available about true energy and

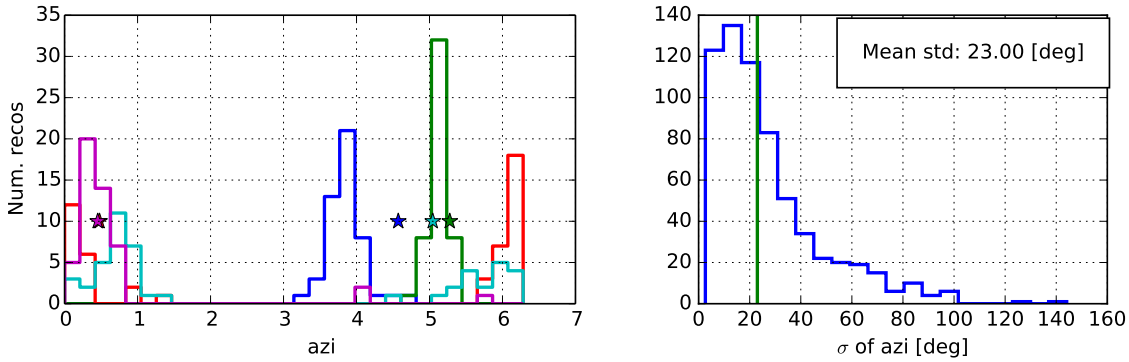

Figure 5.20: Left: a random selection of events, with individual colors, and a histogram of the reconstructed value of the azimuth angle, the star of the same color show the true value. Right: The spread in reconstructed azimuth angle for the same event reconstructed 100 times, shown for 1000 random events from the final event selection.

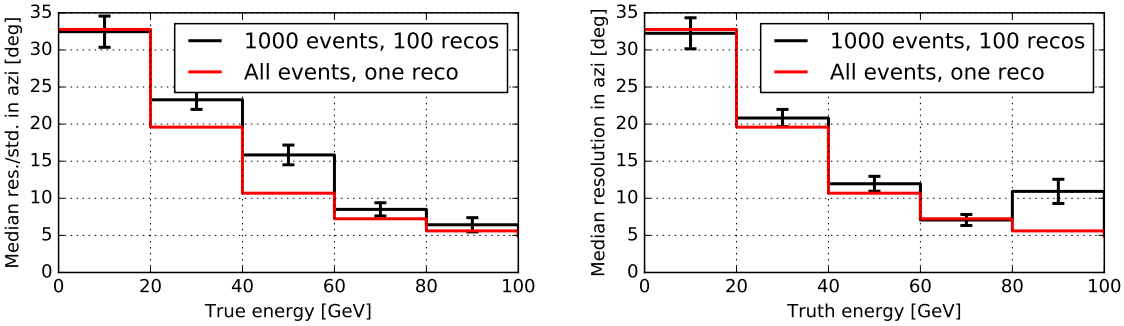

Figure 5.21: Left: The median resolution of the full event sample of muon neutrinos binned in true energy (red) is compared to the median spread (volatility) of 1000 randomly selected muon neutrino events each reconstructed 100 times (black). Right: The median resolution of the full event sample (red) is compared to the median resolution of the 100 reconstructions (black), demonstrating that the 1000 events are representative of the full sample in terms of the resolution.

angular resolution. Assuming that the observation of the resolution and the volatility being about the same also holds for experimental data, the volatility can instead be used as a measure for the resolution in experimental data. The comparison is made in the right panel of Figure 5.22 demonstrating that the volatility is at least not a larger problem in experimental data. In order to explore this more precisely, one should take into account the complication from the fact that in experimental data there are a mix of atmospheric muons and various neutrino flavors, compared to the simplicity of only muon neutrinos in the simulation considered here. However, in this analysis it is sufficient ensure that the volatility is not significantly worse for experimental data.

From the considerations discussed in this section regarding valotility, two approaches are taken for the analysis. First, the distributions of events used in the analysis will be binned with a bin width that covers the volatility of the events, such that the events end up in the same bin regardless of whether the volatility was present or not. The details of this shall be covered when discussing the generation of the distributions used in the likelihood analysis presented in Section 6.1.

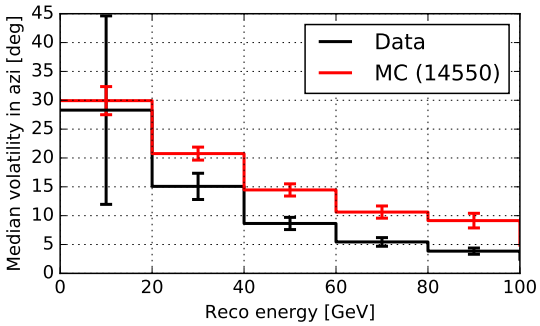

Figure 5.22: The median volatility in the simulated sample (14550) of muon neutrinos (red) is compared to 150 events from experimental data (black).

Secondly, the effect from the volatility on the final results shall be investigated to ensure that it does not introduce features that are unaccounted for. This is done by running the reconstruction two times on each event in the experimental data, and determining the effect on the thermally averaged product of the WIMP annihilation cross section and the relative velocity, $\langle \sigma v \rangle$. Using the likelihood values from the two reconstructions, the one that arrived at a more likely set of reconstructed parameters (better likelihood value) shall be used for calculating the final results.

6

Analysis method

With the distribution of signal neutrinos and atmospheric backgrounds in the final event selection, a shape likelihood analysis is used to calculate the most likely fraction of the experimental data that can be ascribed to neutrinos from the annihilation of WIMPs in the galactic center.

The analysis is carried out in the full range of right ascension and within a declination band of (± 1 radians) as a binned shape likelihood analysis. The final events are filled into a binned two dimensional distribution of the arrival direction, which for signal neutrinos and atmospheric background shall serve as the probability density function (PDF). The signal expectation is varied over multiple WIMP masses between 10 and 1000 GeV for annihilations through b-quarks ($b\bar{b}$), W-bosons (W^+W^-), muons ($\mu^+\mu^-$), taus ($\tau^+\tau^-$), as well annihilation directly to neutrinos ($\nu\bar{\nu}$). The search will be carried out for all combinations of aforementioned WIMP mass and annihilation channels. For the W^+W^--channel only WIMP masses above 100 GeV are probed, as on-shell W-bosons can only be produced by annihilations of WIMPs with a mass above 80 GeV (the mass of the W-boson).

The construction of confidence intervals, the calculation of sensitivities and final limits, as well as the handling of systematic uncertainties will be discussed in this chapter before presenting the results in the next chapter.

6.1 Producing PDFs

The shape likelihood analysis is based on the PDFs of signal neutrinos and atmospheric background, that shall be compared to the distribution of the actual observation of the full experimental dataset. Four different distributions are produced: two based on the experimental data, and two based on the signal neutrino simulation. One is filled with the actual reconstructed values of the right ascension and one is filled with the randomized (or *scrambled*) right ascension (denoted scr.).

The events from simulation are weighted to a given WIMP annihilation signal, and represent the *signal PDF*. The scrambled experimental data shall be used to represent the *background PDF*, however it may be contaminated by signal, which is accounted for in the likelihood formulation by subtracting the *scrambled signal PDF*.

Under the hypothesis that a fraction μ, of the experimental data is from signal neutrinos, the PDF of scrambled experimental data, will be composed of scrambled background and scrambled signal, such that:

$$\mathrm{PDF}_{\text{scr. data}} = (1-\mu)\mathrm{PDF}_{\text{scr. bkg}} + \mu\mathrm{PDF}_{\text{scr. signal}}. \tag{6.1}$$

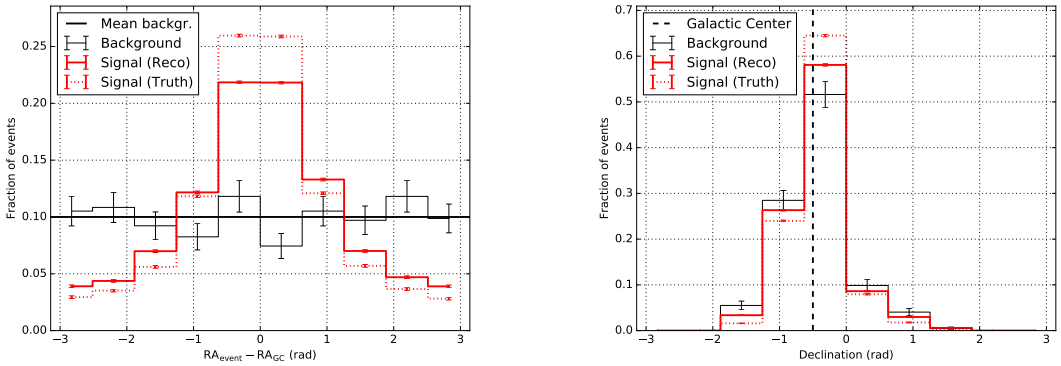

Figure 6.1: Projection of the probability distributions of the expected signal for the benchmark channel (100 GeV WIMP annihilating through W^+W^-) in red and the scrambled background in black (no scrambled signal subtracted) for the right ascension relative to the galactic center on the left, and the declination on the right.

The atmospheric background is uniform in right ascension[157], and therefore the background PDF can be determined from Eq. (6.1) as:

$$\mathrm{PDF}_{\mathrm{bkg}} = \mathrm{PDF}_{\mathrm{scr.\ bkg}} = \frac{1}{1-\mu}\left(\mathrm{PDF}_{\mathrm{scr.\ data}} - \mu\mathrm{PDF}_{\mathrm{scr.\ signal}}\right). \tag{6.2}$$

The unscrambled experimental data is referred to as the *actual observation*, and shall be discussed further after unblinding in the next chapter.

In Figure 6.1 the signal and background PDFs are projected to one dimension, with the binning used in the analysis (which shall be discussed below). The background distribution presented is the burn sample (i.e. 10% of experimental data from 2012), which explains the large statistical fluctuations.

In right ascension, one can observe how the signal PDF peaks around the right ascension corresponding to the galactic center (smeared out from the true distribution be the limited resolution of the reconstruction), whereas the background PDF is fluctuating around a uniform distribution in right ascension due to the scrambling.

The declination angle at the South Pole is given as $\mathrm{dec} = \theta_{zenith} - \pi/2$. So the atmospheric muon are expected to dominate at declinations and vanish at positive declinations, but some atmospheric muons will be mis-reconstructed as upgoing, and show up for positive declinations. The PDFs in declination for the signal neutrinos look very similar to the atmospheric background PDF because the declination, or rather the zenith angle is used in the event selection, so most information from that dimension has already been exploited.

6.1.1 Choosing the binning of the PDF

For the binning of the PDFs used in the analysis, the effect of the volatility of the HybridReco/MultiNest reconstruction, i.e. achieving different reconstructed values when rerunning the algorithm (discussed in Section 5.12.2) needs to be taken into account. The bins need to be wide enough that most events get collected in the bin that they would be in if HybridReco/MultiNest had properly found a consistent minimum. By reducing the migration of events between bins, the

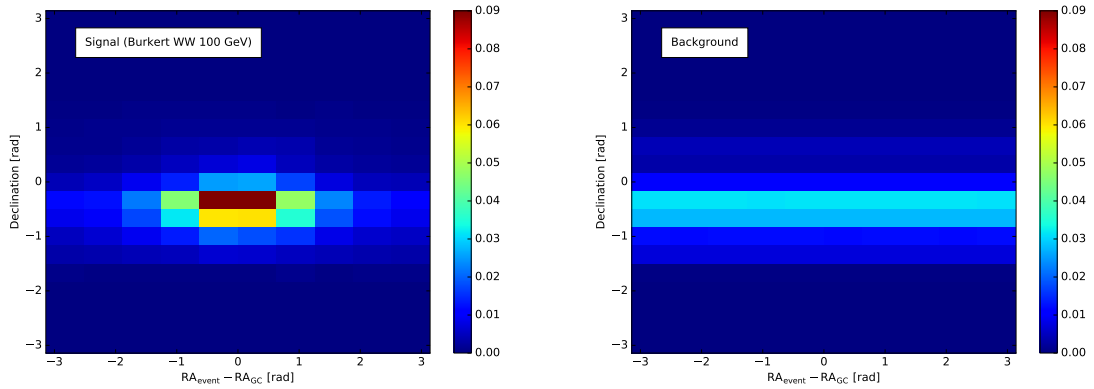

Figure 6.2: Probability distributions of the expected signal for the benchmark channel (100 GeV WIMP annihilating through W^+W^-) on the left and scrambled background (without scrambled signal subtracted) on the right.

effect of the volatility is reduced. On the other hand, if we knew for sure that the reconstructions worked the same for MC and data, any bin width could be used (within the constraints imposed by statistical considerations). There is no evidence that there is a difference, but since the limits should reflect our best knowledge, we should rather be conservative than optimistic. Hence it was chosen to go with the conservative choice in bin widths that insure that the possible shift in reconstructed values of azimuth and zenith angle are accommodated by the binning.

It was discussed in Section 5.12.2 that the volatility is observed to be within the size of the resolution, therefore the resolution is used to guide the choice of bin width. In order for the analysis to be consistent over multiple WIMP masses and annihilation channels, the resolution of the worst case scenario is chosen. The annihilation through $b\bar{b}$ produces neutrinos with the softest spectrum (i.e. larger fraction of low energy neutrinos), and will on average have the worst angular resolution. By choosing a bin width of (dec, RA) = (22.9°, 36°) the worst case scenario of a 10 GeV WIMP annihilating through $b\bar{b}$ is accommodated. From the annihilation of high mass WIMPs, a significant fraction of the signal neutrinos will also have a low energy, so even though the volatility and average resolution becomes smaller for higher WIMP masses, these wider bins are also needed at higher WIMP masses.

The resulting two dimensional PDFs for signal and background are presented in Figure 6.2.

6.1.2 Effect on sensitivity

Using a conservative bin width means that we lose some of the details in the pointing. The degradation will vary for different signals, a few of which are presented in Table 6.1, when comparing the choice of having (dec, RA) = (22.9°,36°) to the initial choice of (dec, RA) = (11.5°,12°). As the NFW profile has a relatively larger contribution to the density distribution near the center of the galaxy, it is affected more by a coarser binning, because it will hide more of the peaking structure of the halo model. As a result, the degradation is more substantial for the signal assuming the NFW profile. With the goal of increasing the sensitivity from previous analyses by an order of magnitude, a 50% degradation of the limits are acceptable,

Table 6.1: Table showing the degradation in sensitivity by using triple and double the original bin widths in azimuth and zenith angle, respectively.

channel/mass	NFW	Burkert
$\tau\bar{\tau}$, 20 GeV	45%	7%
$\tau\bar{\tau}$, 50 GeV	13%	3%
$\tau\bar{\tau}$, 100 GeV	19%	2%
$\tau\bar{\tau}$, 1000 GeV	56%	10%

and though the loss in sensitivity is not favorable, it is needed in order to account properly for the volatility.

6.2 Likelihood formulation

Depending on the *signal fraction* $\mu \in [0, 1]$, a certain fraction of all the events is expected in a given bin, determined from the PDFs for each component:

$$\begin{aligned} f(\text{bin}_i|\mu) &= \mu\text{PDF}_{\text{signal}}(\text{bin}_i) + (1-\mu)\text{PDF}_{\text{bkg}}(\text{bin}_i) \\ &= \mu\text{PDF}_{\text{signal}}(\text{bin}_i) + \text{PDF}_{\text{src. data}}(\text{bin}_i) - \mu\text{PDF}_{\text{src. signal}}(\text{bin}_i). \end{aligned} \tag{6.3}$$

The expected number of events in a bin $n_{\text{exp}}(\text{bin}_i|\mu)$, is determined from the total number of observed events $n_{\text{obs}}^{\text{total}}$ as

$$n_{\text{exp}}(\text{bin}_i|\mu) = n_{\text{obs}}^{\text{total}} f(\text{bin}_i|\mu). \tag{6.4}$$

The likelihood is then formulated as a product over all bins in the PDF, as the Poisson probability of observing $n_{\text{obs}}(\text{bin}_i)$ in bin_i for a given signal fraction:

$$\mathcal{L}(\mu) = \prod_{\text{bin}_i}^{n \text{ bins}} \frac{(n_{\text{exp}}(\text{bin}_i))^{n_{\text{obs}}(\text{bin}_i)}}{n_{\text{obs}}(\text{bin}_i)!} e^{n_{\text{exp}}(-\text{bin}_i)}. \tag{6.5}$$

6.3 Statistical treatment of analysis

For a given observation, the most likely value of the signal fraction that maximizes the likelihood $\hat{\mu}$, and the (lower and/or upper) confidence interval on the signal fraction $[\mu_{\text{lower}}, \mu_{\text{upper}}]$ can be determined from the likelihood formulation in Eq. (6.5). That shall generally be determined with a confidence $\alpha \in [0, 1]$. The intervals are constructed according to the 'frequentist' approach, which ensures that if the approach is followed in N independent experiments, then αN of the resulting confidence intervals will cover the true signal fraction, μ_{true}. This is an important point of the statistical method used here. It produces specifically defined intervals and does not state anything about the credibility or certainty of the values (which would require a more Bayesian approach).

6.3.1 Confidence intervals

In order to construct the confidence intervals on μ, it is necessary to first generate the acceptance intervals of some test statistic, R (that shall be discussed below).

The distribution of R is sampled from the combined PDF of signal and background for various values of μ. The acceptance intervals are defined as the intervals that holds α of the distribution of possible outcomes of the test statistic. To constrain a discovery, *central confidence intervals* are produced by acceptance intervals with $(1-\alpha)/2$ of the possible outcomes on each side of the interval. If no discovery is made, an *upper limit* is calculated from acceptance intervals with $1-\alpha$ of the possible outcomes on the upper (large value) side of the interval.

From a measurement, the corresponding value of the test statistics is calculated, and the confidence interval for that measurement is composed of all the values of μ that contain the measured value of the test statistic in their acceptance intervals.

For this classical approach to confidence intervals (Neyman intervals[168]), one needs to choose which kind of interval to calculate before looking at the data. Determining which interval to use after looking at the measurement can give confidence intervals that do not reflect the intended confidence α. More precisely, they might suffer from *undercoverage*, corresponding to a α confidence interval that covers less than α of the possible outcomes for a given μ.

6.3.2 Introducing a ranking parameter

In order to avoid the problem of undercoverage, the approach of Feldman and Cousins[169] (FC) is followed. Here a rank is introduced to help guide the construction of acceptance intervals. These intervals will not exhibit the problems mentioned above, and it makes the approach more versatile, because the choice of interval is made by the procedure naturally, providing the proper coverage. The FC method might produce some *overcoverage*, where α confidence intervals cover more than α of the possible outcomes, e.g. for discrete values of the test statistic. It is always better if the desired confidence level is matched, but if it can not be achieved it is better to be conservative, and hence overcoverage is preferred over undercoverage.

The rank is calculated as the ratio of the likelihood of a given signal fraction μ to the likelihood of $\hat{\mu}$ given an observation:

$$R(\mu, \text{obs}) = \frac{\mathcal{L}(\mu|\text{obs})}{\mathcal{L}(\hat{\mu}|\text{obs})}. \tag{6.6}$$

The ratio is limited for all μ for any set of observation (obs), i.e. $R \leq 1$, since $\mathcal{L}(\mu|\text{obs}) \leq \mathcal{L}(\hat{\mu}|\text{obs})$. The acceptance interval is then produced from the values of the test statistic, starting with the highest rank and adding values with lower rank until α of the possible outcomes are covered. The test statistic could in principle be anything, but by using the likelihood ratio R of Eq. (6.6) as the test statistic it will follow the FC method (by construct), making it very simple to construct confidence intervals.

The approach is illustrated on Figure 6.3, where in the left panel, R is calculated for 10000 pseudo-experiments carried out by drawing $n_{\text{obs}}^{\text{total}}$ events from a combined PDF of signal and background with $\mu = 0.1$, where $n_{\text{obs}}^{\text{total}}$ is the total number of events in the actual observation. The α acceptance intervals are created by taking the α highest value of R among the pseudo-experiments, presented in Figure 6.3 with the critical value of the test statistic, $R^{\alpha}_{\text{critical}}(\mu)$.

The results of this analysis shall be quoted at $\alpha = 90\%$ confidence level, and the result is therefore determined from $R^{90\%}_{\text{critical}}(\mu)$. For a given experiment/observation

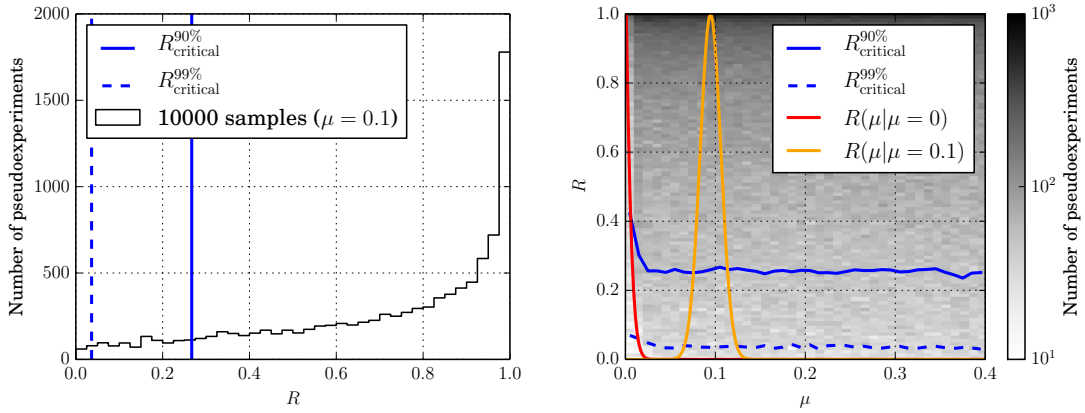

Figure 6.3: Left: The distribution of the test statistic R calculated for 10000 pseudo-experiments for $\mu = 0.1$, with the 90% (99%) critical value of the test statistic, corresponding to the 90% (99%) acceptance intervals indicated with blue solid (dashed) line. Right: Distribution of pseudo-experiments across multiple values of μ presented in the grey scale histogram. The 90% (99%) acceptance intervals $R_{\text{critical}}(\mu)$ are indicated and $R(\mu)$ is calculated for two pseudo-experiments with specific values of μ. The values of μ where $R(\mu) = R_{\text{critical}}(\mu)$ constitute the confidence interval on μ.

obs, the corresponding value of the test statistic across all values of μ, $R(\mu, \text{obs})$, is calculated and the points where $R(\mu, \text{obs}) = R^{90\%}_{\text{critical}}(\mu)$ are found.

On the right panel of Figure 6.3 two pseudo-experiments are compared to the acceptance intervals. One pseudo-experiment (red) is carried out by sampling from a background-only ($\mu = 0$) PDF, and the corresponding line for $R(\mu, \text{obs})$ only crosses $R^{90\%}_{\text{critical}}(\mu)$ for one value of $\mu = \mu^{90\%}_{\text{upper}}$, since $\mu > \hat{\mu} = 0$ the value of μ corresponds to a 90% upper limit. The other pseudo-experiment (orange) is sampled from a combined PDF with $\mu = 0.1$, the resulting test statistic is seen to cross the critical value for two values of $\mu \in \mu^{90\%}_{\text{lower}}, \mu^{90\%}_{\text{upper}}$, which would correspond to a 90% central limit.

6.3.3 Calculating the sensitivity

Before calculating the result from the observation in experimental data, the expected limit or *sensitivity* of the selection and analysis is calculated for the background-only hypothesis. This defines the expectation for the values for $\langle \sigma v \rangle$ if no signal is present in the actual observation, wheres as if the result is significantly above that expectation, a claim of a discovery can be made.

The sensitivity is determined from 100000 pseudo-experiments of background-only ($\mu = 0$), sampled from the scrambled experimental data with the scrambled signal subtracted. In order not to be prone to statistical fluctuations, the median of resulting upper limits is quoted as the sensitivity $\mu^{90\%}_{\text{upper}}$, technically the 90% median upper limit. This is also the approach used in order to optimize the choice of cut on the BDT score (discussed in Section 5.10.2).

The statistical uncertainty on the sensitivity is determined from the same distribution of pseudo-experiments and presented in terms of the 1σ and 2σ uncertainties (referring to the corresponding inclusive percentages of a Gaussian).

6.3.4 Relating measurement to the annihilation cross section

While the previous measured quantity is defined as the signal fraction, the desired physically relevant value is the thermally averaged product of the WIMP annihilation cross section and relative velocity, $\langle \sigma v \rangle$.

From the actual observation the total number of observed events $n_{\text{obs}}^{\text{total}}$, is calculated, and with the PDFs describing the signal and background, the limit on the signal fraction $\mu_{\text{upper}}^{90\%}$, is determined from the likelihood analysis as described above, resulting in an upper limit on the number of signal events:

$$N_{\text{signal}}^{\text{upper}} = \mu_{\text{upper}}^{90\%} n_{\text{obs}}^{\text{total}}. \tag{6.7}$$

Conversely the number of signal events in the sample N_{signal}, is dependent on the livetime of the detector T_{detector}, and the flux realised in the analysis Φ_{analysis}:

$$N_{\text{signal}} = \Phi_{\text{analysis}} T_{\text{detector}}. \tag{6.8}$$

By introducing the acceptance of the analyses, $A_{\text{analysis}}(E_\nu, \Psi)$ (which will be dependent on neutrino energy E_ν and direction Ψ), Ψ_{analysis} can be calculated by using the differential flux of Eq. (1.10):

$$\Phi_{\text{analysis}} = \int A_{\text{analysis}}(E_\nu, \Psi) \frac{d\Phi}{dE_\nu}(\Psi) dE_\nu d\Psi \tag{6.9}$$

$$= \frac{\langle \sigma v \rangle}{8\pi m_{\text{DM}}^2} \int \left[A_{\text{analysis}}(E_\nu, \Psi) \frac{dN}{dE}(E_\nu) \int_{\text{los}} \rho_{\text{DM}}^2(r(s, \Psi)) ds \right] dE_\nu d\Psi. \tag{6.10}$$

Here m_{DM} is the WIMP mass and $dN/dE(E_\nu)$ is the differential energy distribution depending on the WIMP annihilation channel. The spherically symmetric density of the galactic dark matter halo $\rho_{\text{DM}}(r)$ is integrated along the line-of-sight a distance s into the halo.

The simulation of signal neutrinos is weighted to the expected differential signal flux $d\Phi/dE_\nu(\Psi)$, and by propagating the simulation of the signal neutrinos through the analysis, the resulting number of signal neutrino events provide the value N_{signal} for any value of $\langle \sigma v \rangle$. Hence, the upper limit on the thermally averaged product of the WIMP annihilation cross section and velocity $\langle \sigma v \rangle_{\text{upper}}^{90\%}$, can be determined as the value of $\langle \sigma v \rangle$ that give a number of signal neutrinos that corresponds to the upper limit determined from Eq. (6.7).

By the approach described the sensitivity on μ can be related to a sensitivity on $\langle \sigma v \rangle$, which is presented for the individual annihilation channels, for various WIMP masses in Figure 6.4. In addition, the sensitivity of the predecessor of this analysis (IC79) is also presented, demonstrating an improvement of more than an order of magnitude for various channels with the present work, which further explores the sensitivity to lower WIMP masses.

6.4 Systematic uncertainties

The strength of the neutrino signal from the WIMP annihilations and efficiency of detecting the signal neutrinos are not known with complete certainty. The uncertainty on the strength of the signal is dominated by the uncertainties of the

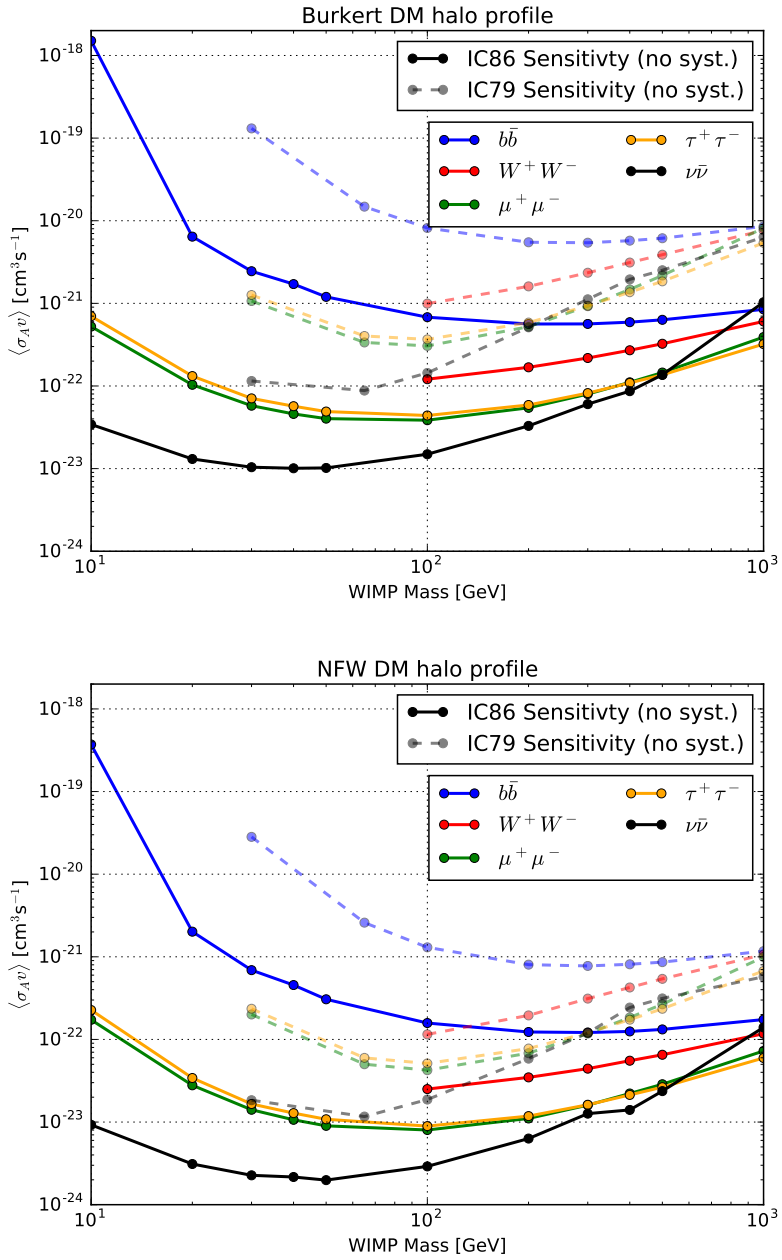

Figure 6.4: The sensitivity (or 90% median upper limit) of the present analysis (IC86) on $\langle\sigma v\rangle$ as a function of WIMP mass, for various annihilation channels assuming the Burkert or NFW halo profile. In addition, the sensitivity of the preceding analysis (IC79) is present for comparison, demonstrating an improvement in some channels of more than an order of magnitude, as well as an increase in the range of WIMP masses probed.

halo density profile, and shall be handled by presenting the result for different halo profiles. The impact of the implementation of physics of the neutrino interactions and their detection is specific to IceCube and will be incorporated as a combined uncertainty, that will be taken into account by worsening the final limits with the combined systematic uncertainty on the detection.

The detection efficiency of neutrinos in IceCube depends mainly on the optical properties of the South Pole ice, and the efficiency of the individual DOMs. In simulation, the optical properties are implemented by given models and parameters, and the detection efficiency of the signal neutrinos will depend on these choices, which in turn will influence the final results. The effect of each systematic uncertainty is determined by propagating simulated datasets with variations in the models all the way through the analysis. The difference on the resulting value for $\langle \sigma v \rangle$ from the systematic dataset to the baseline datasets, is quoted as the systematic uncertainty for that given variation. The systematic uncertainty on $\langle \sigma v \rangle$ is calculated for the muon neutrinos, as it is the main component of the search, and the effect is assumed to be the same across all flavours.

The total systematic uncertainty is determined by adding all the individual contributions from the detection uncertainty in quadrature. For some of the systematic effects, the model is changed by both increasing and decreasing the given value, but only the variation that affects the result most is included in calculating the total systematic uncertainty. The systematics considered are discussed in the following subsections, and in Figure 6.5 the values of the individual components of the systematic uncertainty on the detection efficiency is presented for the $b\bar{b}$ annihilation channel, though the values are similar across annihilation channels.

6.4.1 Bulk ice model

The propagation of photons through the South Pole ice is dependent on the optical properties of the ice, which mainly vary with depth. The ice within IceCube has been modeled using estimates for the effective absorption and scattering length from flashers in the ice (as discussed in Section 3.1.2).

The latest incorporated ice model (SPIce Lea) is the best estimate of the optical properties of the South Pole ice, but it is still just a simplified model, which can never give an identical representation of the bulk ice at the South Pole. Traditionally the light absorption and scattering parameters of the bulk ice are varied with 10%, corresponding to the expected uncertainty from the ice modelling. That approach is reflecting a choice of working from the best possible model available and then studying the effect of varying the parameters of the model. Though it does not probe the fact that various generation of ice models are different, both in parameters and in approach.

This is especially relevant, since SPIce Lea can not currently be employed in reconstructions that use photon tables (discussed in Section 5.6.4). The added complexity of the azimuthal dependence of the optical properties would increase the dimensionality of the already memory- and computationally-expensive photon tables, making it impractical to use in current reconstructions. Instead the previous iteration, SPIce Mie, that does not include the known effect of the azimuthal anisotropy, must be used.

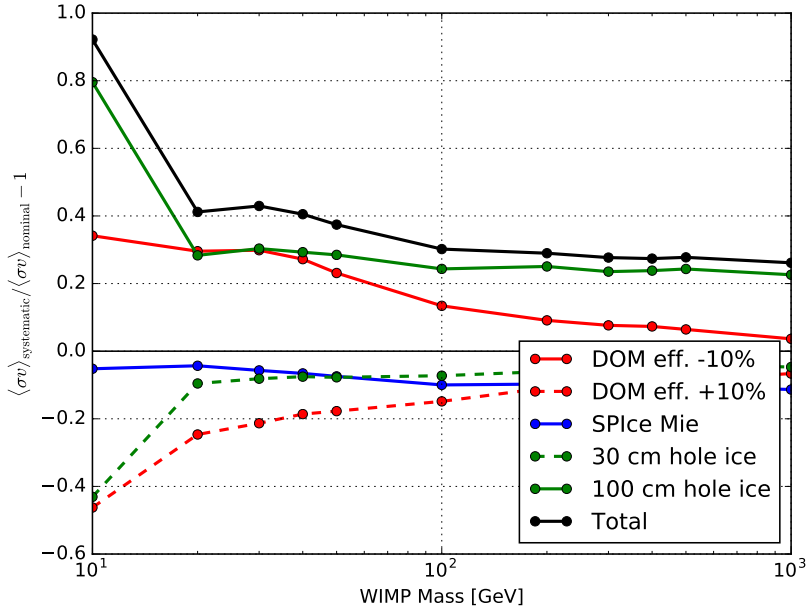

Figure 6.5: The relative contributions of the individual systematic uncertainties on the detection efficiency of muon neutrinos, when compared to the baseline sets. They are plotted as a function of WIMP mass for the annihilation through $b\bar{b}$ (with similar values across other annihilation channels) assuming the Burkert halo profile. The total systematic uncertainty is calculated by adding each contribution in quadrature.

So even for the baseline simulation set, the reconstruction is based on a different ice model than what is actually used in the simulation. This is in principle reflecting the situation with reconstructing events in the experimental data, as the ice model used for reconstruction also will be different than the one that is actually present.

In an attempt to estimate the effect of reconstructing with a different ice model, a dataset is simulated using the SPIce Mie ice model, and reconstructed with the same model. By comparing the resulting value on $\langle\sigma v\rangle$ for this set to the baseline set (SPIce Lea), the effect of discrepant ice models in the reconstruction can be estimated for experimental data. So in this work the systematic effect related to the bulk ice is actually focusing on investigating the general effect of reconstructing assuming a different ice, than the one that the light actually propagated through.

As can be seen from Figure 6.5 changing to a simulation of SPIce Mie (i.e. same as used in the reconstruction) changes the result 5-15%. In previous analyses a similar effect is seen from simply varying the parameters within a given ice model, which is then also covered in this work by changing the entire model.

6.4.2 Hole ice

The refrozen ice from the melted water in the drill holes, has a much shorter effective scattering length than the surrounding bulk ice. This is especially apparent in the column of bubbles within the *hole ice* affects the optical properties of the ice right around the DOMs (as discussed in Section 3.1.3). In simulation, the different optical properties of the hole ice (dominated by the bubble column) are described by an

angular acceptance of the DOM, parametrized in terms of the incident angle of the photon to the DOM. This effectively describes the result of the shorter scattering length in the hole ice, without adding complexity to the photon propagation.

The current implementation is based on data from flasher runs from AMANDA (the predecessor to IceCube), and simulations of photons scattering off of air bubbles. It was determined that the hole ice has a geometrical scattering length of 50 cm, with an uncertainty that is bracketed by varying it between 30 cm and 100 cm[137]. The measured geometrical scattering length can be translated to an effective scattering length[170] between 100-350 cm, much smaller than the tens of meters for the bulk ice.

The 50 cm hole ice model described constitutes the baseline for simulation in IceCube, however, that is only covering this particular parametrization of the hole ice. There are ongoing investigations within IceCube, some of which favor another parametrization, and some that confirm the baseline choice[171]. At the time of writing, it has not been determined that another model should be employed, and this analysis will follow the established standard approach, and investigate the effect on $\langle \sigma v \rangle$ from changing the effective scattering length of the hole ice.

An increased scattering in the hole ice makes it more probable to detect photons propagating downwards, because the enhanced backscatter directing more photons onto the active surface of the down facing DOM, but will decrease the acceptance of incoming photons propagating upwards. This is illustrated on Figure 6.6 where the deviations can be compared to the baseline geometrical scattering length of 50 cm.

A larger scattering in the hole ice makes the detector more sensitive to downgoing photons, hence to downgoing tracks, and therefore more sensitive to the signal neutrinos, that are predominantly downgoing. So a shorter scattering length (resulting in photons being scattered more) would yield a better sensitivity on $\langle \sigma v \rangle$. On Figure 6.5 the result of shortening the effective scattering length to 30 cm, is seen to improve the sensitivity by about 10%, with only a slight dependence on neutrino energy and hence WIMP mass. Conversely, increasing the scattering length results in a 20-30% worse sensitivity on $\langle \sigma v \rangle$.

6.4.3 DOM optical efficiency

If a photon truly arrives at the face of a PMT, the probability of it producing a photoelectron is given by the quantum efficiency of the PMT. In the simulation the quantum efficiency is implemented by accepting a photon randomly with a certain probability when it has reached the DOM. The probability implemented in the simulation is referred to as the optical efficiency of the DOM or *DOM efficiency*, and incorporates the PMT quantum efficiency, cable shadowing, and other subdominant hardware elements that limit the detection probability of the DOM.

The DOM efficiency is estimated using a sample of minimun ionizing atmospheric muons, producing photons roughly uniformly through IceCube. The average charge detected by DOMs with a certain distance to the track was determined in experimental data and in simulations with different values of the DOM efficiency. The best estimate of the DOM efficiency is then estimated by comparing the observation and the different variations in simulation[172].

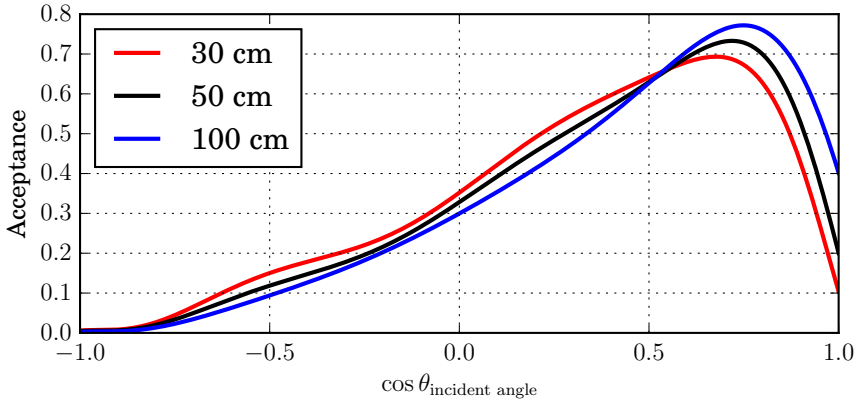

Figure 6.6: Angular acceptance incorporated to account for the scattering of photons in the hole ice. The baseline 50 cm geometrical scattering length is shown together with the deviations from changing the geometrical scattering length between 30 cm and 100 cm. It is illustrated how the increase (decrease) in scattering result in an increase (decrease) of downgoing photons backscattering, and a decrease (increase) of upgoing photons.

In the process of estimating the DOM efficiency it is a challenge to distinguish the strictly DOM related effects from the effect of local variations in the ice around the DOM. The task of determining the optical efficiency of the DOMs is being approached in different ways, resulting in a DOM efficiency with a conservative uncertainty of 10%. Even though the systematic effect of the hole ice model and the DOM efficiency might be correlated, they shall be regarded as independent when calculating the total systematic uncertainty.

The effect of increasing the DOM optical efficiency will increase the detection of light, making it easier to detect charged particles in IceCube. This makes the detection of lower energy particles easier and the veto techniques employed to reject the background more effective. Because atmospheric muons are taken from data, by definition they have a perfect DOM efficiency and as such only the simulation of signal neutrinos is modified, increasing the number of (especially) low energy signal neutrinos. This results in an improvement on $\langle \sigma v \rangle$, which is larger for lower WIMP masses, because they are more sensitive to detection efficiencies, as can be seen on Figure 6.5. A decrease in DOM efficiency would result in the opposite effect of decreasing the sensitivity to $\langle \sigma v \rangle$, which can also be seen on Figure 6.5.

The DOM optical efficiency constitutes the largest systematic uncertainty for this analysis with an effect between 5-50%.

6.4.4 Applying the systematic uncertainty

The following conservative approach is employed: The final limits in $\langle \sigma v \rangle$ are worsened (i.e. made weaker) by a factor corresponding to the total systematic uncertainty, no matter whether a given systematic effect increases or decreases the value of $\langle \sigma v \rangle$. In this way, only one final limit is presented for each combination of WIMP mass and annihilation channel. The total systematic uncertainty in this analysis is between about 20-80% depending on the WIMP mass. Since the background

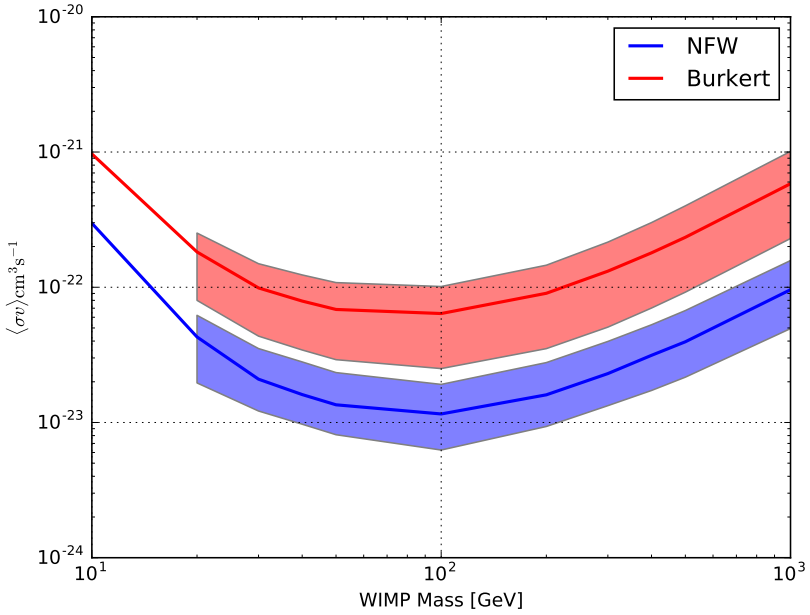

Figure 6.7: The sensitivity to $\langle\sigma v\rangle$ for the $\tau^+\tau^-$ annihilation channel, comparing the two halo models examined. The bands reflect changing the halo model's parameters one standard devation according to the model fits of Ref. [84].

is estimated from data, no systematic variations are needed for the atmospheric backgrounds as the experimental data will, per definition, be correct.

6.4.5 Astrophysical uncertainties

From Figure 6.4 it was clear that changing the halo profile changes the value of $\langle\sigma v\rangle$ quite substantially. Because the correct dark matter halo profile is not known, this adds an uncertainty on $\langle\sigma v\rangle$ of 200-400%. In this work the model fits of Ref. [84] are employed for estimating the dark matter halo profiles (as discussed in Section 1.4). Where the parameters of the model fits are determined with some uncertainty.

The resulting effect on $\langle\sigma v\rangle$ due to the uncertainty on the parameters of the individual models is presented on Figure 6.7. It illustrates that changing the fit parameters of the halo models within one standard deviation (indicated in Table 1.1) change the values of $\langle\sigma v\rangle$ by 150-200%, matching investigations made in a previous analysis[91]. Only the major effect of changing between halo models shall be represented by reporting the resulting value of $\langle\sigma v\rangle$ for both profiles.

7

Results

With the final event selection, the analysis ready, and the expected sensitivity calculated, the final limits can be calculated for the experimental data. The directional information is unblinded, and the analysis is run for all combinations of WIMP annihilations to determine the *final limits*. The results shall be discussed and compared to other experiments in the field. The chapter shall end with an outlook on future similar analyses, a discussion of the limitations of this specific analysis, and the general opportunities of searches for WIMP annihilations with neutrinos.

7.1 Unblinding data

After the analysis was approved by the IceCube Collaboration the data is unblinded, and the actual directional information is revealed for the full 3 years of IceCube data. The event selection result in 22632 events in the unblinded sample from a total detector livetime of 1004.8 days from May 15, 2012 to May 18, 2015. In Figure 7.1 the projection onto the right ascension plane of the PDFs for the expected benchmark signal is presented with the distribution of the unblinded data (normalized) and the uniform background from scrambled data. From looking at the figure, only small deviations are visible from the scrambled background, and more importantly, there is no visible correlation with the expected signal.

7.1.1 Volatility checks

As an additional check of the impact of the volatility of HybridReco/MultiNest, the experimental data was reconstructed twice. Using only the first or only the second reconstruction gives slightly different final results on $\langle \sigma v \rangle$ that deviate within about 10% from each other, well below the systematic uncertainty for most WIMP masses. Because the HybridReco/MultiNest reconstruction provides a likelihood value, the iteration with the better likelihood value is chosen, since it will be representing the more correct value for that given event. This approach has been applied in all the results shown in the remainder of this chapter.

7.1.2 Unblinded results

With the implementation of the Feldman and Cousins method for calculating limits from a set of ranks (discussed in the Section 6.3) the 90% confidence intervals are calculated for all the combinations of WIMP mass, annihilation channel, and dark matter halo density. No large deviation from the background-only expectation is

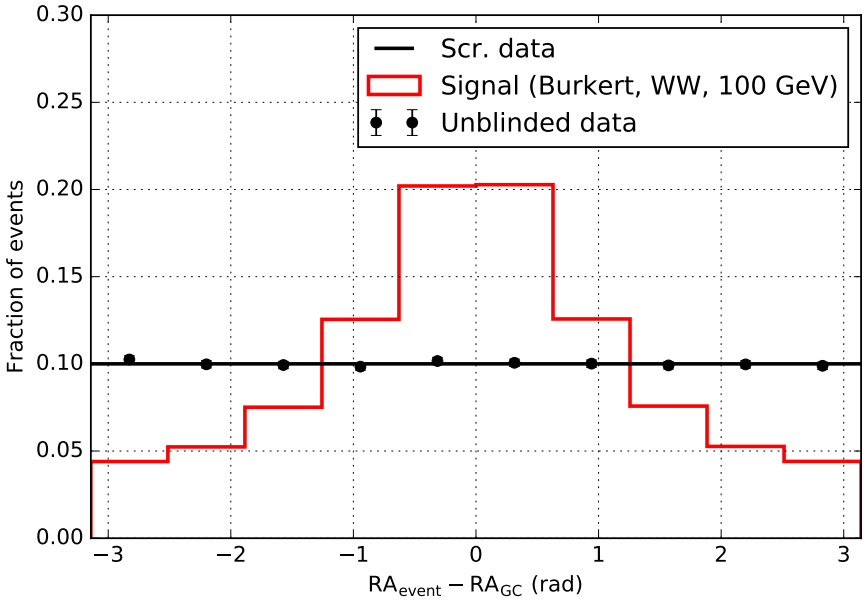

Figure 7.1: The unblinded data distribution in right ascension relative to the galactic center, plotted with the distribution of the scrambled data and the benchmark signal neutrino simulation. All distributions are normalized, and the statistical error on the unblinded data is barely visible as it amount to an uncertainty on the fraction of events of about 0.002 across all bins.

observed in the unblinded data on Figure 7.1, and the best fit value for the signal fraction μ is less than 1% for all combinations of WIMP properties. The confidence interval on μ includes the zero signal point for all combinations, hence the central limits will not be relevant, i.e. no discovery was made, and instead upper limits are presented for $\langle \sigma v \rangle$.

In Figure 7.2 and Figure 7.3 the unblinded 90% upper limits are presented together with the sensitivity and corresponding statistical uncertainty band for 1σ and 2σ uncertainties for the Burkert and NFW profiles respectively. The limits on the figures are presented without systematic uncertainties. Since the same event sample is used in the same analysis to calculate the individual WIMP mass points the resulting limits are correlated between WIMP mass points and across annihilation channels.

There is a slight change in the ratio between the resulting limits and the sensitivity between WIMP masses of 30-200 GeV (depending on annihilation channel), which for the NFW profile results in the two matching and for the Burkert profile results in an under fluctuation at low WIMP masses. At high WIMP masses a slight overfluctuation is observed for both halo profiles. However, all of the fluctuations are well within the 1σ statistical uncertainty, and the slight excess seen is not statistically significant.

7.1.3 Including systematic uncertainties

Accounting for the systematic uncertainties, the resulting limits are worsened (increased in value) with the corresponding total systematic uncertainty for that given

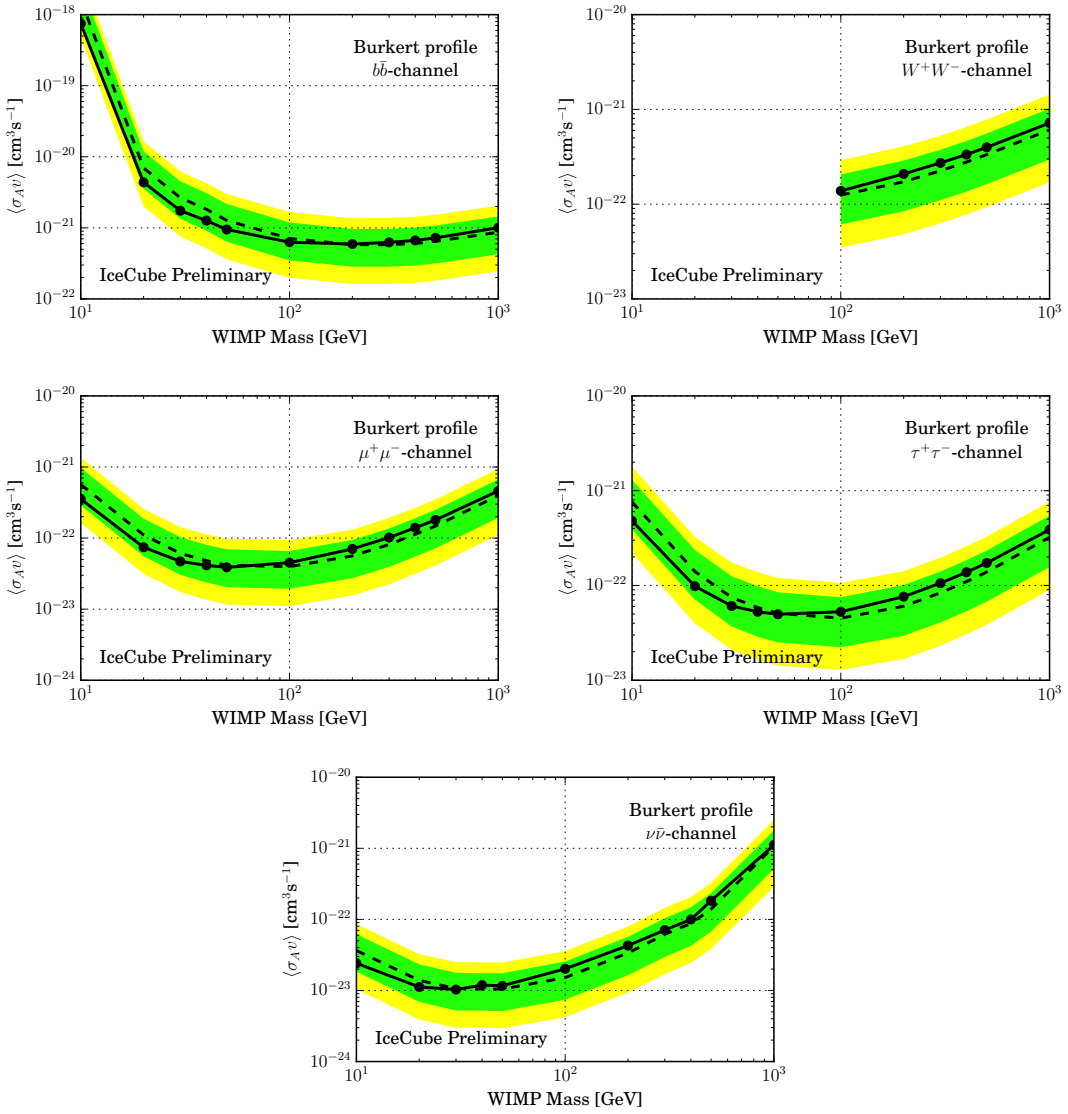

Figure 7.2: The resulting 90% upper limits (solid black line) and the sensitivity (dashed black line) along with its associated statistical uncertainty of 1σ (2σ) standard deviations in green (yellow), plotted as a function of WIMP mass for the Burkert halo profile. Each plot shows one of the probed annihilation channels, with no systematic uncertainties added.

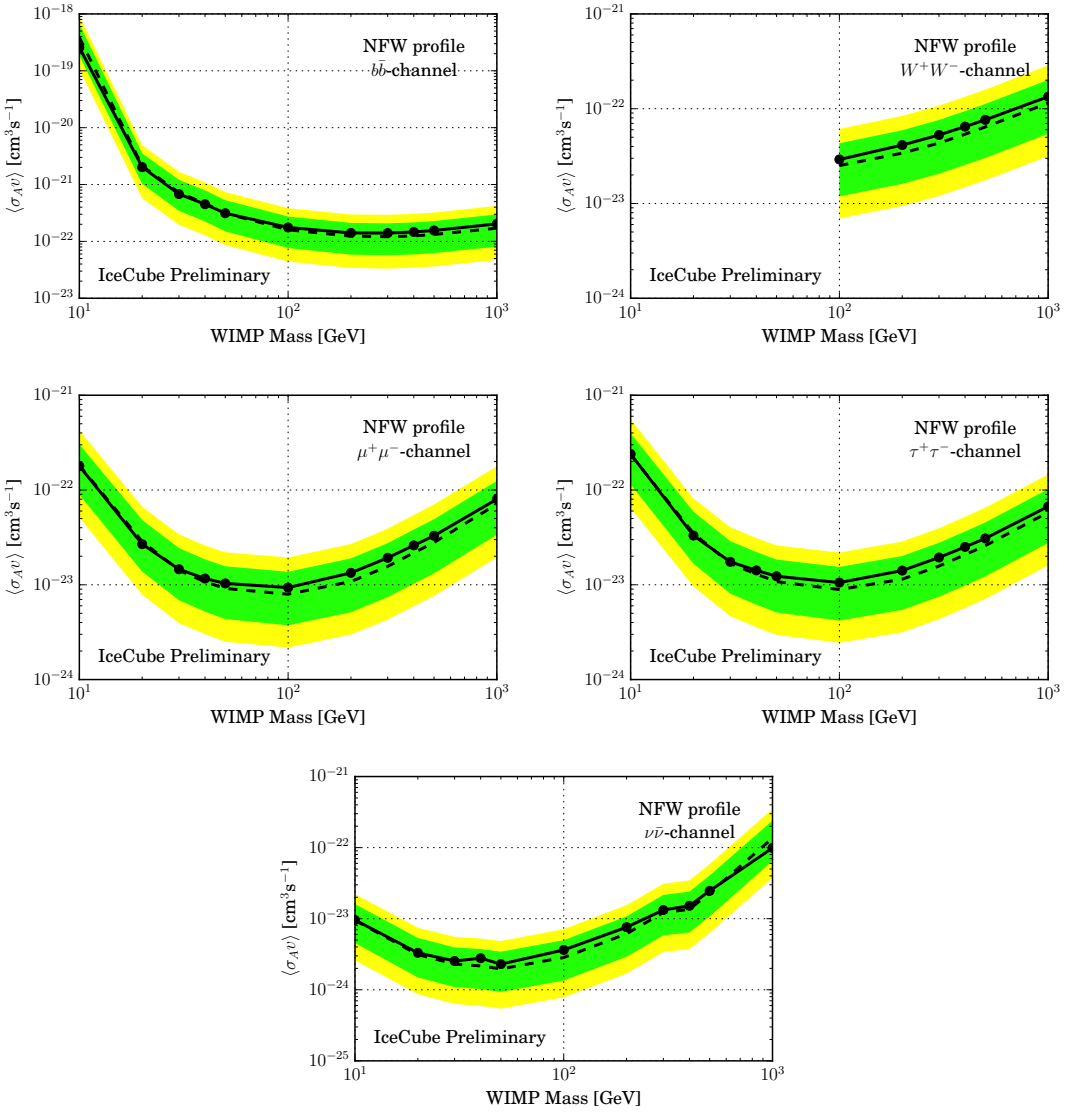

Figure 7.3: The resulting 90% upper limits (solid black line) and the sensitivity (dashed black line) along with its associated statistical uncertainty of 1σ (2σ) standard deviations in green (yellow), plotted as a function of WIMP mass for the NFW halo profile. Each plot shows one of the probed annihilation channels, with no systematic uncertaintie added.

Table 7.1: Final upper limits on $\langle\sigma v\rangle$, presented for the Burkert halo profiles.

m_{DM} [GeV]	$\langle\sigma v\rangle$ for the Burkert profile $[10^{23}\mathrm{cm}^3\mathrm{s}^{-1}]$				
	$b\bar{b}$	W^+W^-	$\mu^+\mu^-$	$\tau^+\tau^-$	$\nu\bar{\nu}$
10	143 667.49	—	49.61	70.60	3.64
20	616.16	—	10.40	14.50	1.52
30	249.35	—	6.25	8.45	1.33
40	177.95	—	5.31	7.15	1.53
50	130.33	—	5.00	6.68	1.60
100	81.79	17.94	5.77	6.97	2.60
200	76.30	26.83	8.92	10.05	5.58
300	79.82	35.18	12.98	13.85	8.84
400	84.82	42.68	17.58	18.00	14.01
500	92.37	50.31	22.71	22.19	28.39
1000	126.69	90.16	58.92	50.04	187.39

Table 7.2: Final upper limits on $\langle\sigma v\rangle$, presented for the NFW halo profiles.

m_{DM} [GeV]	$\langle\sigma v\rangle$ for the NFW profile $[10^{23}\mathrm{cm}^3\mathrm{s}^{-1}]$				
	$b\bar{b}$	W^+W^-	$\mu^+\mu^-$	$\tau^+\tau^-$	$\nu\bar{\nu}$
10	96 549.33	—	25.43	36.03	1.63
20	292.24	—	3.81	4.94	0.44
30	98.70	—	1.95	2.43	0.33
40	63.33	—	1.51	1.91	0.37
50	43.10	—	1.33	1.67	0.33
100	23.06	3.84	1.20	1.42	0.47
200	18.28	5.36	1.68	1.86	0.93
300	18.00	6.75	2.44	2.52	1.85
400	18.78	8.17	3.20	3.17	3.04
500	19.80	9.54	3.97	3.87	5.09
1000	25.45	16.84	10.22	8.59	22.27

combination of WIMP mass, annihilation channel and halo profile, in order to arrive at the *final limits*. All combinations of annihilation channels and WIMP masses considered are presented with the associated final 90% upper limits in Table 7.1 and Table 7.2 for the Burkert and NFW halo profile respectively. All the limits are listed assuming a branching ratio of the WIMP annihilation of 100% through a specific channel. The limits for the $\nu\bar{\nu}$ are assuming a production ratio of $(\nu_e : \nu_\mu : \nu_\tau) = (1 : 1 : 1)$ at source.

For the neutrino signal from WIMP annihilation to non-neutrino particle, the neutrino flavor ratio is determined by the particles produced, but for the annihilation straight to neutrinos there are currently no observations that favor a specific choice of flavor ratio. The default assumption for WIMPs annihilating directly to neutrinos, is that it happens with a flavor ratio of $(\nu_e : \nu_\mu : \nu_\tau) = (1 : 1 : 1)$. However, in order for the limit to cover other possible flavor ratios at the source, the

Table 7.3: Impact on the final limits on $\langle \sigma v \rangle$ for the WIMP annihilating into signal neutrino with different flavor ratios, comparing the flavor ratios are source to what they will be at Earth after long baseline neutrino oscillations.

Ratio at source	Ratio at Earth	$\langle \sigma v \rangle$ for 100 GeV WIMP (Bur)
$(1:1:1)$	$(1:1:1)$	$2.60 \cdot 10^{-23}$ cm^3/s
$(1:0:1)$	$(0.37:0.32:0.31)$	$2.65 \cdot 10^{-23}$ cm^3/s
$(1:0:0)$	$(0.55:0.25:0.20)$	$2.86 \cdot 10^{-23}$ cm^3/s
$(0:1:0)$	$(0.25:0.37:0.38)$	$2.49 \cdot 10^{-23}$ cm^3/s
$(0:0:1)$	$(0.20:0.38:0.42)$	$2.48 \cdot 10^{-23}$ cm^3/s

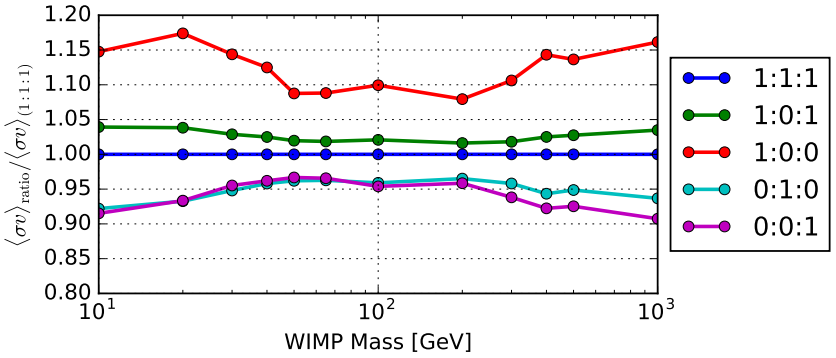

Figure 7.4: Ratio of the sensitivity to $\langle \sigma v \rangle$ for a few different flavour ratios for the signal neutrinos at source compared to the a flavor ratio of $(\nu_e : \nu_\mu : \nu_\tau)_{\text{pes}} = (1:1:1)$.

flavor ratio that gives the most conservative limits should be pursued. The flavor ratio that provide the most conservative limit will depend on the flavor to which the analysis is most sensitivity to. For this analysis most of the sensitivity comes from muon neutrinos, so the lower the fraction of muon neutrinos at Earth, the worse the sensitivity should be.

In calculating the limits for various flavor ratios of the produced neutrinos at source, the effect of long baseline neutrino oscillations have to be taken into account. The resulting flavor ratios at Earth are presented in Table 7.3 for a few different flavor ratios at source. Due to the neutrino oscillations the flavor ratio will be washed out when the neutrinos reach Earth, and there will always be a significant fraction of muon neutrinos in the sample when they reach Earth, so the limits on $\langle \sigma v \rangle$ do not change considerably.

The most conservative limits can be set for a flavor ratio of $(\nu_e : \nu_\mu : \nu_\tau)_{\text{conc}} = (1:0:0)$. The best case scenario is a flavor ratio of $(\nu_e : \nu_\mu : \nu_\tau)_{\text{opt}} = (0:0:1)$, since the large mixing between ν_e and ν_μ means that a pure muon neutrino production at source results in slightly worse sensitivity after taking oscillations into account. As can be seen on Figure 7.4, the change in sensitivity is more or less independent of WIMP mass, and amounts to about 15% worse (10% better) sensitivity for the most pessimistic (optimistic) flavor ratio at source.

7.2 Comparisons to other experiments

In the current experimental landscape there are many similar experiments searching for a signal from annihilating WIMPs. On Figure 7.5 a selection of results are presented with a focus on neutrino based experiments as well as the strongest limits from γ-ray observatories. For the search from the galactic halo, the SuperKamiokande experiment has a larger sensitivity to lower neutrino energies and lower WIMP masses. The ANTARES experiment is located on the northern hemisphere, and therefore does not look for a signal in the large background of atmospheric muons. However at sufficiently low energies, the rejection of atmospheric muons and detection of signal neutrinos are so good in IceCube that the limits become competitive around WIMP masses of 100 GeV, for which this analysis has been optimized.

The strongest limits on $\langle \sigma v \rangle$ for WIMP masses below a few TeV are provided from γ-ray observations, though the neutrino observations are (with the latest preliminary results from ANTARES) dominating the searches for WIMP masses above a few TeV, where the universe starts to become opaque to photons.

The search for annihilating WIMPs outside of the Milky Way is less affected by uncertainties on the halo density profile, but results in a much lower sensitivity due to the lower flux of signal neutrinos. The latest published result from IceCube on dwarf galaxies is indicated in solid green line on Figure 7.5.

Even though this analysis of the indirect detection of WIMP annihilation covers WIMP masses where some of the direct detection experiments have claimed to observed signal from dark matter, the two search methods cannot be compared without multiple assumptions on the connection between the two.

It can be observed from Figure 7.5 that the improvement in the final limits of the present analysis are not an order of magnitude better than the previous analysis of the galactic center using the 79-string configuration of IceCube (IC79 GC). This was the expectation from comparing the sensitivities of the two analyses (discussed in Section 6.3.3). A large under-fluctuation in the unblinded data in the IC79 yielded a stronger-than-expected limit. Regardless, this analysis reaches stronger limits for WIMP masses up to 800 GeV, but not by an order of magnitude.

The analysis presented in this work sets the strongest limits from IceCube below 500 GeV. It provide a competitive contribution to global limits of WIMP annihilations from the galactic halo. At the time of writing, this analysis present the worlds strongest limits from neutrino observations on annihilations of WIMPs with masses between 40-250 GeV.

7.3 Outlook

The investigations and study of dark matter physics continues to be at a very exciting stage. There are claims of observations of WIMP-nucleon interactions in direct detection experiments, that would indicate that WIMPs are the right candidate for dark matter, whereas other experiments rule out those observations. From γ-ray experiments a range of claims of signal from annihilating WIMPs have been made, however, most of them have not been confirmed in followup studies, demonstrating that they are due to unmodelled foreground contributions. At the

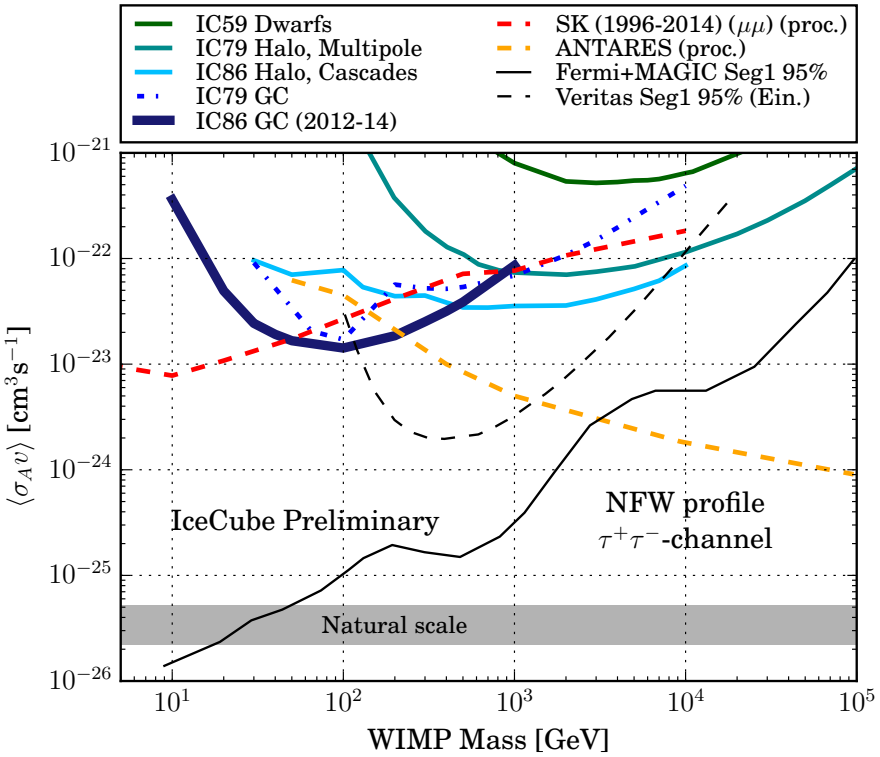

Figure 7.5: Final limits of the present analysis (thick solid dark blue) plotted along with the previous iteration[157] (dot-dashed blue), other neutrino results from IceCube (indicated with IC and the number of strings deployed in the given analysis, as well as the source investigated)[173, 174, 175] (solid lines in lighter blue, green), SuperKamiokande[176] (dashed red), ANTARES[177] (dashed orange), and results from x-ray observations with Fermi+MAGIC[77] (solid black) and Veritas[178]. The natural scale indicates with required value of $\langle\sigma v\rangle$ if WIMPs are thermal relics.

time of writing the most interesting signal is the excess from the center of the Milky Way measured in Fermi, though there are still promising foreground contributions that might explain the excess[179]. Since the discovery of the Higgs boson, there has not been confirmed observations of additional resonances/particle from searches at accelerator experiments[180].

With the booming interest within neutrino astronomy and frequent publications, the exploration of the universe with this completely different probe is as strong as ever. The neutrino can bring information with higher energies and from other processes than photons. Combining dark matter searches and neutrino astronomy has by now introduced a field of research that can explore dark matter differently, and the last few years of research have seen a huge interest in going down that path.

Still no observations have been made of annihilating WIMPs from neutrinos, but the phase space is steadily being constrained, latest with the results presented in this thesis that constrain the value of $\langle\sigma v\rangle$ with the best limits for WIMP masses around 100 GeV.

7.3.1 Ideas for improvements

Looking forwards, there are a list of improvements that can be recommended for the future development of WIMP searches from the galactic center with IceCube. With the ongoing understanding of the high level reconstruction HybridReco, and the improved efficiency by the latest iterations of the minimization process, data can in principle be reconstructed at a larger rate. With that possibility, the analysis can be run for the full sky and not a narrow band in zenith.

For investigating the galactic center the only approach for removing the atmospheric muons are by utilizing various veto techniques, which might be improved by combining some of the methods employed in this work. Combining the muon neutrino focused selection with a selection of cascades, will increase the sensitivity. Especially at lower energies, where the resolution of cascades might supersede that of tracks as has been demonstrated in a concurrent analysis (contribution 9 of Ref. [181]).

For higher WIMP masses (above 10 TeV) including an energy estimator in the likelihood formulation has been shown to add significantly to the sensitivity[92], especially for the annihilation directly to neutrinos for which the energy distribution differs significantly from that of atmospheric muons and neutrinos.

To a lesser degree, improved understanding of the systematic uncertainties would lead to stronger resulting limits. With the ongoing investigations into more precise models of the optical properties of the ice, both the bulk ice and the understanding of the bubble column in the drill hole ice, there will be improvements to work from for the next generation analyses. It is not clear what magnitude of improvement these investigations will give for future studies, but enhanced understanding of systematics may be a necessary step for future large increases in sensitivity.

7.3.2 Limitations of indirect detection searches

The indirect detection experiments still have not seen persisting observations of any excess of neutrinos above background. Until that happens, analyses that increase the sensitivity with an order of magnitude are needed in order to steadily uncover the phase space of the WIMPs. When a discovery is made, there will be a need for many further checks, and a further development of the systematic scrutiny. For now the search is to find something out of the ordinary by a broad search of the phase space paying attention only to significant deviations. Now that high-energy neutrinos have been shown to exist with some extra-terrestrial origin[125], it will become increasingly important to take the astrophysical component into account in future indirect detection searches. Unless they actually originate from WIMP annihilation or decay, astrophysical neutrinos from other sources are just an additional background for the signal of dark matter annihilation.

As all indirect dark matter detection searches hinge on the assumption that dark matter self-annihilates or decays, the searches are limited to dark matter candidates with this property. With the, so far, unfruitful search for WIMPs, more and more of the interest in the community is shifting to non-WIMP candidates for dark matter. Though until an observation is confirmed, all options continue to be open, albeit getting more constrained. Even as the limits approach the natural scale of $\langle \sigma v \rangle$, the value needed for the WIMPs to be thermal relics, the class of WIMP type particles

are still not ruled out, as variations of the model can be made such that they do not need to be thermal relics. But every analyses that constrains a subset of dark matter candidates, helps guide the future analyses towards a possible discovery.

7.3.3 Future detectors

In addition to the changes that can be carried out with the current detector, the development of future neutrino telescopes is well under way, and will provide more and better possibilities to look for WIMPs using neutrinos. The construction of KM3Net[182], the next generation version of ANTARES, is ongoing and should be able to provide stronger limits on $\langle \sigma v \rangle$ from studying neutrinos from the galactic center, as it shares the benefit of being on the northern hemisphere. Whether improvements will mainly be at high energies or whether the part of KM3Net intended for detecting relatively low energy neutrinos will add to the low WIMP mass points, is to be demonstrated.

Developments on an additional low energy extension to IceCube are being finalized during the writing of this thesis. Referred to as PINGU[183], the goal is to bring the energy threshold from the current about 10 GeV down to 1 GeV, while exploiting the great veto of IceCube by embedding PINGU within the dense strings of the DeepCore volume in IceCube. Though mainly focused on the neutrino mass ordering and the detection of tau neutrino appearance from oscillating atmospheric neutrinos, PINGU will improve the sensitivity to low mass WIMPs. The current estimates are showing a sensitivity to WIMP masses of 5-10 GeV using PINGU, which are similar to those of the analysis of 100 GeV WIMP with IceCube/DeepCore[183]. Further in the future a high energy extension of IceCube will be expected in order to enhance the capture rate of high energy neutrinos, known as IceCube-Gen2[184] With the addition of the envisioned surface array, IceCube-Gen2 might provide competitive conditions for WIMP searches from the galactic center. If the initial phase of KM3Net adds as much new information to the field of neutrino astronomy as IceCube has, the expansion of IceCube will indeed be the natural next step for neutrino astronomy, with future experiments providing further possibilities to push the search for WIMPs to even higher energies.

8

Conclusion

This work presented the search for annihilating dark matter, in the form of a Weakly Interacting Massive Particle (WIMP). Employing the latest efforts in reconstruction of charged particles and the rejection of atmospheric muons with various veto techniques, this analysis sets the best limits from neutrino observations on the thermally averaged product of the WIMP annihilation cross section and velocity, $\langle \sigma v \rangle$, for WIMP masses between about 50-250 GeV (depending on annihilation channel). For annihilation of a 100 GeV WIMP through W^+W^-, the thermally averaged product of the WIMP annihilation cross section and velocity is constrained to $\langle \sigma v \rangle = 3.84 \cdot 10^{-23} \mathrm{cm}^3 \mathrm{s}^{-1}$. Using the DeepCore volume of IceCube, the low energy neutrinos are accessible, and by designing an improved data selection, the sensitivity from previous IceCube analyses has been improved with up to an order of magnitude. And the final limits on $\langle \sigma v \rangle$ provide the best limits from IceCube on annihilations in the galactic halo for WIMP masses below 500 GeV (depending on the annihilation channel).

Neutrinos can provide a different insight to dark matter than γ-rays, by the signal of neutrinos from WIMP annihilations. Even though the strength of the searches with neutrinos are limited by the low neutrino-nucleon cross section, and resulting low detection rate, when a signal is finally seen in neutrinos, it will be so much more exciting to understand the cause and origin. Each new analysis brings new ideas forward for the continued search, and the search with neutrinos will continue in following years.

A decade ago the construction of IceCube started following up on initial searches for dark matter signals with the first generation neutrino observatories. This analysis is part of the continuous exploration of the phase space of annihilating WIMPs, with larger or denser detectors, as well as better and more efficient reconstructions and vetoing algorithms. With the construction of larger and improved neutrino detection experiments even stronger results are possible within the next decade. Even though dark matter searches are not the single main driver for these future experiments, it adds a science case to the proposals. A science case for understanding the matter that constitute the majority of all gravitational mass in out universe, that is as strong as ever.

Bibliography

[1] Y. Sofue and V. Rubin. "Rotation Curves of Spiral Galaxies". In: *Annual Review of Astronomy and Astrophysics* 39.1 (Sept. 2001), pp. 137–174. DOI: 10.1146/annurev.astro.39.1.137.

[2] S. van den Bergh. "The Early History of Dark Matter". In: *Publications of the Astronomical Society of the Pacific* 111.760 (June 1999), pp. 657–660. DOI: 10.1086/316369.

[3] F. Zwicky. "Die Rotverschiebung von extragalaktischen Nebeln". In: *Helvetica Physica Acta* 6 (1933), pp. 110–127.

[4] F. Zwicky. "On the Masses of Nebulae and of Clusters of Nebulae". In: *The Astrophysical Journal* 86 (Oct. 1937), p. 217. DOI: 10.1086/143864.

[5] E. Hubble. "The Distribution of Extra-Galactic Nebulae". In: *The Astrophysical Journal* 79 (June 1934), p. 8. DOI: 10.1086/143517.

[6] S. Smith. "The Mass of the Virgo Cluster". In: *The Astrophysical Journal* 83 (Jan. 1936), p. 23. DOI: 10.1086/143697.

[7] J. P. Ostriker, P. J. E. Peebles, and A. Yahil. "The size and mass of galaxies, and the mass of the universe". In: *The Astrophysical Journal* 193 (Oct. 1974), p. L1. DOI: 10.1086/181617.

[8] J. Einasto, A. Kaasik, and E. Saar. "Dynamic evidence on massive coronas of galaxies". In: *Nature* 250.5464 (July 1974), pp. 309–310. DOI: 10.1038/250309a0.

[9] I. Newton. *Philosophiæ Naturalis Principia Mathematica*. July 1687.

[10] H. W. Babcock. "The rotation of the Andromeda Nebula". In: *Lick Observatory Bulletins* 19 (1939), pp. 41–51. DOI: 10.5479/ADS/bib/1939LicOB.19.41B.

[11] J. H. Oort. "Some Problems Concerning the Structure and Dynamics of the Galactic System and the Elliptical Nebulae NGC 3115 and 4494." In: *The Astrophysical Journal* 91 (Jan. 1940), p. 273. DOI: 10.1086/144167.

[12] S. M. Kent. "Dark matter in spiral galaxies. II - Galaxies with H I rotation curves". In: *The Astronomical Journal* 93 (Apr. 1987), p. 816. DOI: 10.1086/114366.

[13] C. Carignan and S. Beaulieu. "Optical and H I studies of the 'gas-rich' dwarf irregular galaxy DDO 154". In: *The Astrophysical Journal* 347 (Dec. 1989), pp. 760–770. DOI: 10.1086/168167.

[14] K. G. Begeman, A. H. Broeils, and R. H. Sanders. "Extended rotation curves of spiral galaxies: dark haloes and modified dynamics". In: *Monthly Notices of the Royal Astronomical Society* 249.3 (Apr. 1991), pp. 523–537. DOI: 10.1093/mnras/249.3.523.

[15] Y. Mellier. "Gravitational lensing and dark matter". In: *Particle Dark Matter: Observations, Models and Searches*. Ed. by G. Bertone. Cambridge University Press, 2013. ISBN: 978-1-107-65392-4.

[16] J. A. Tyson, G. P. Kochanski, and I. P. Dell'Antonio. "Detailed Mass Map of CL 0024+1654 from Strong Lensing". In: *The Astrophysical Journal* 498.2 (), p. L107. DOI: 10.1086/311314.

[17] H. Hoekstra, H. K. C. Yee, and M. D. Gladders. "Current status of weak gravitational lensing". In: *New Astronomy Reviews* 46.12 (Nov. 2002), pp. 767–781. DOI: 10.1016/S1387-6473(02)00245-2.

[18] U. Sarkar. *Particle and Astroparticle Physics*. Taylor & Francis Group, 2008. ISBN: 978-1-58488=931=1.

[19] W. Hu and S. Dodelson. "Cosmic Microwave Background Anisotropies". In: *Annual Review of Astronomy and Astrophysics* 40.1 (Sept. 2002), pp. 171–216. DOI: 10.1146/annurev.astro.40.060401.093926.

[20] W. Hu. "CMB temperature and polarization anisotropy fundamentals". In: *Annals of Physics* 303.1 (Jan. 2003), pp. 203–225. DOI: 10.1016/S0003-4916(02)00022-2.

[21] P. Collaboration et al. "Planck 2015 results. XIII. Cosmological parameters" (Feb. 2015).

[22] G. Bertone, D. Hooper, and J. Silk. "Particle dark matter: evidence, candidates and constraints". In: *Physics Reports* 405.5-6 (Jan. 2005), pp. 279–390. DOI: 10.1016/j.physrep.2004.08.031.

[23] K. N. Abazajian et al. "The Seventh Data Release of the Sloan Digital Sky Survey". In: *The Astrophysical Journal Supplement Series* 182.2 (May 2009), pp. 543–558. DOI: 10.1088/0067-0049/182/2/543.

[24] D. J. Eisenstein et al. "Detection of the Baryon Acoustic Peak in the Large-Scale Correlation Function of SDSS Luminous Red Galaxies". In: *The Astrophysical Journal* 633.2 (Nov. 2005), pp. 560–574. DOI: 10.1086/466512.

[25] W. J. Percival et al. "Baryon acoustic oscillations in the Sloan Digital Sky Survey Data Release 7 galaxy sample". In: *Monthly Notices of the Royal Astronomical Society* 401.4 (Feb. 2010), pp. 2148–2168. DOI: 10.1111/j.1365-2966.2009.15812.x.

[26] L. Anderson et al. "The clustering of galaxies in the SDSS-III Baryon Oscillation Spectroscopic Survey: baryon acoustic oscillations in the Data Releases 10 and 11 Galaxy samples". In: *Monthly Notices of the Royal Astronomical Society* 441.1 (June 2014), pp. 24–62. DOI: 10.1093/mnras/stu523.

[27] V. Springel et al. "Simulations of the formation, evolution and clustering of galaxies and quasars". In: *Nature* 435.7042 (June 2005), pp. 629–636. DOI: 10.1038/nature03597.

[28] M. Boylan-Kolchin et al. "Resolving cosmic structure formation with the Millennium-II Simulation". In: *Monthly Notices of the Royal Astronomical Society* 398.3 (Sept. 2009), pp. 1150–1164. DOI: 10.1111/j.1365-2966.2009.15191.x.

[29] V. Springel, C. S. Frenk, and S. D. M. White. "The large-scale structure of the Universe". In: *Nature* 440.7088 (Apr. 2006), pp. 1137–1144. DOI: 10.1038/nature04805.

[30] S. D. M. White, C. S. Frenk, and M. Davis. "Clustering in a neutrino-dominated universe". In: *The Astrophysical Journal* 274 (Nov. 1983), p. L1. DOI: 10.1086/184139.

[31] P. Bode, J. P. Ostriker, and N. Turok. "Halo Formation in Warm Dark Matter Models". In: *The Astrophysical Journal* 556.1 (July 2001), pp. 93–107. DOI: 10.1086/321541.

[32] M. Moniez. "Microlensing as a probe of the Galactic structure: 20 years of microlensing optical depth studies". In: *General Relativity and Gravitation* 42.9 (Sept. 2010), pp. 2047–2074. DOI: 10.1007/s10714-009-0925-4.

[33] S. Hannestad. "Primordial Neutrinos". In: *Annual Review of Nuclear and Particle Science* 56.1 (Nov. 2006), pp. 137–161. DOI: 10.1146/annurev.nucl.56.080805.140548.

[34] J. Lesgourgues and S. Pastor. "Neutrino Mass from Cosmology". In: *Advances in High Energy Physics* 2012.4-5 (2012), pp. 1–34. DOI: 10.1155/2012/608515.

[35] D. J. Griffiths. *Introduction to Elementary Particles*. Second. WILEY-VCH Verlag GmbH & Co. KGaA, 2008. ISBN: 978-3-527-40601-2.

[36] K. N. Abazajian et al. "Light Sterile Neutrinos: A White Paper" (Apr. 2012). arXiv: 1204.5379 [hep-ph].

[37] K. Abazajian, G. M. Fuller, and M. Patel. "Sterile neutrino hot, warm, and cold dark matter". In: *Physical Review D* 64.2 (May 2001), p. 023501. DOI: 10.1103/PhysRevD.64.023501.

[38] S. Alekhin et al. "A facility to search for hidden particles at the CERN SPS: the SHiP physics case". In: *Reports on Progress in Physics* 79.12 (Oct. 2016), p. 124201. DOI: 10.1088/0034-4885/79/12/124201.

[39] J. D. Bekenstein. "Modified Gravity as an Alternative to Dark Matter". In: *Particle Dark Matter: Observations, Models and Searches*. Ed. by G. Bertone. Cambridge University Press, 2013. ISBN: 978-1-107-65392-4.

[40] D. Clowe, A. Gonzalez, and M. Markevitch. "Weak-Lensing Mass Reconstruction of the Interacting Cluster 1E0657-558: Direct Evidence for the Existence of Dark Matter". In: *The Astrophysical Journal* 604.2 (Apr. 2004), pp. 596–603. DOI: 10.1086/381970.

[41] M. Bradač et al. "Revealing the Properties of Dark Matter in the Merging Cluster MACS J0025.4-1222". In: *The Astrophysical Journal* 687.2 (Nov. 2008), pp. 959–967. DOI: 10.1086/591246.

[42] A. Mahdavi et al. "A Dark Core in Abell 520". In: *The Astrophysical Journal* 668.2 (Oct. 2007), pp. 806–814. DOI: 10.1086/521383.

[43] M. J. Jee et al. "Hubble Space Telescope/Advanced Camera for Surveys Confirmation of the Dark Substructure in A520". In: *The Astrophysical Journal* 783.2 (Feb. 2014), p. 78. DOI: 10.1088/0004-637X/783/2/78.

[44] M. Pohl and D. Eichler. "Fermi Constrains Dark-Matter Origin of High-Energy Positron Anomaly". In: *The Astrophysical Journal Letters* 712.1 (2010), p. L53. DOI: 10.1088/2041-8205/712/1/L53.

[45] J. Merten et al. "Creation of cosmic structure in the complex galaxy cluster merger Abell 2744". In: *Monthly Notices of the Royal Astronomical Society* 417.1 (Oct. 2011), pp. 333–347. DOI: 10.1111/j.1365-2966.2011.19266.x.

[46] W. A. Dawson et al. "Discovery of a Dissociative Galaxy Cluster Merger with Large Physical Separation". In: *The Astrophysical Journal* 747.2 (Feb. 2012), p. L42. DOI: 10.1088/2041-8205/747/2/L42.

[47] F. Kahlhoefer et al. "On the interpretation of dark matter self-interactions in Abell 3827". In: *Monthly Notices of the Royal Astronomical Society: Letters* 452.1 (July 2015), pp. L54–L58. DOI: 10.1093/mnrasl/slv088.

[48] D. Hooper and S. Profumo. "Dark matter and collider phenomenology of universal extra dimensions". In: *Physics Reports* 453.2-4 (Dec. 2007), pp. 29–115. DOI: 10.1016/j.physrep.2007.09.003.

[49] K. Garrett and G. Duda. "Dark Matter: A Primer". In: *Advances in Astronomy* 2011.6 (2011), pp. 1–22. DOI: 10.1155/2011/968283.

[50] Y. B. Zel'dovich. "Survey of Modern Cosmology". In: Advances in Astronomy and Astrophysics, 1965, pp. 241–379. ISBN: 9781483199214. DOI: 10.1016/B978-1-4831-9921-4.50011-9.

[51] J. Edsjö and P. Gondolo. "Neutralino relic density including coannihilations". In: *Physical Review D* 56.4 (Aug. 1997), pp. 1879–1894. DOI: 10.1103/PhysRevD.56.1879.

[52] G. Gelmini and P. Gondolo. "DM production mechanisms". In: *Particle Dark Matter: Observations, Models and Searches*. Ed. by G. Bertone. Cambridge University Press, 2013. ISBN: 978-1-107-65392-4.

[53] G. Jungman, M. Kamionkowski, and K. Griest. "Supersymmetric dark matter". In: *Physics Reports* 267.5-6 (Mar. 1996), pp. 195–373. DOI: 10.1016/0370-1573(95)00058-5.

[54] G. Steigman, B. Dasgupta, and J. F. Beacom. "Precise relic WIMP abundance and its impact on searches for dark matter annihilation". In: *Physical Review D* 86.2 (July 2012), p. 023506. DOI: 10.1103/PhysRevD.86.023506.

[55] J. L. Feng. "Non-WIMP candidates". In: *Particle Dark Matter: Observations, Models and Searches*. Ed. by G. Bertone. Cambridge University Press, 2013. ISBN: 978-1-107-65392-4.

[56] J. L. Feng and J. Kumar. "The WIMPless Miracle: Dark Matter Particles without Weak-Scale Masses or Weak Interactions". In: *Physical Review Letters* 101.23 (Dec. 2008), p. 231301. DOI: 10.1103/PhysRevLett.101.231301.

[57] Y. Hochberg et al. "Mechanism for Thermal Relic Dark Matter of Strongly Interacting Massive Particles". In: *Physical Review Letters* 113.17 (Oct. 2014), p. 171301. DOI: 10.1103/PhysRevLett.113.171301.

[58] K. Griest and M. Kamionkowski. "Unitarity limits on the mass and radius of dark-matter particles". In: *Physical Review Letters* 64.6 (Feb. 1990), pp. 615–618. DOI: 10.1103/PhysRevLett.64.615.

[59] S. Profumo. "TASI 2012 Lectures on Astrophysical Probes of Dark Matter" (Jan. 2013). arXiv: 1301.0952 [hep-ph].

[60] H. Ejiri, K. Fushimi, and H. Ohsumi. "Search for spin-coupled dark matter by studying the axial-vector excitation of nuclei". In: *Physics Letters B* 317.1-2 (Nov. 1993), pp. 14–18. DOI: 10.1016/0370-2693(93)91562-2.

[61] R. Bernabei et al. "Final model independent result of DAMA/LIBRA–phase1". In: *The European Physical Journal C* 73.12 (Nov. 2013), p. 2648. DOI: 10.1140/epjc/s10052-013-2648-7.

[62] C. E. Aalseth et al. "Search for An Annual Modulation in Three Years of CoGeNT Dark Matter Detector Data" (Jan. 2014). arXiv: 1401.3295 [astro-ph.CO].

[63] C. E. Aalseth et al. "Maximum Likelihood Signal Extraction Method Applied to 3.4 years of CoGeNT Data" (Jan. 2014). arXiv: 1401.6234 [astro-ph.CO].

[64] R. Agnese et al. "Silicon Detector Dark Matter Results from the Final Exposure of CDMS II" (Apr. 2013). arXiv: 1304.4279 [hep-ex].

[65] R. Agnese et al. "Improved WIMP-search reach of the CDMS II germanium data". In: *Physical Review D* 92.7 (Oct. 2015), p. 072003. DOI: 10.1103/PhysRevD.92.072003.

[66] G. Angloher et al. "Results on low mass WIMPs using an upgraded CRESST-II detector". In: *The European Physical Journal C* 74.12 (Dec. 2014), p. 3184. DOI: 10.1140/epjc/s10052-014-3184-9.

[67] M. T. Frandsen et al. "The unbearable lightness of being: CDMS versus XENON". In: *Journal of Cosmology and Astroparticle Physics* 2013.07 (July 2013), p. 023. DOI: 10.1088/1475-7516/2013/07/023.

[68] J. Billard, E. Figueroa-Feliciano, and L. Strigari. "Implication of neutrino backgrounds on the reach of next generation dark matter direct detection experiments". In: *Physical Review D* 89.2 (Jan. 2014), p. 023524. DOI: 10.1103/PhysRevD.89.023524.

[69] A. Drukier and L. Stodolsky. "Principles and applications of a neutral-current detector for neutrino physics and astronomy". In: *Physical Review D* 30.11 (Dec. 1984), pp. 2295–2309. DOI: 10.1103/PhysRevD.30.2295.

[70] B. Cabrera, L. M. Krauss, and F. Wilczek. "Bolometric detection of neutrinos". In: *Physical Review Letters* 55.1 (July 1985), pp. 25–28. DOI: 10.1103/PhysRevLett.55.25.

[71] J. Monroe and P. Fisher. "Neutrino backgrounds to dark matter searches". In: *Physical Review D* 76.3 (Aug. 2007), p. 033007. DOI: 10.1103/PhysRevD.76.033007.

[72] D. Abercrombie et al. "Dark Matter Benchmark Models for Early LHC Run-2 Searches: Report of the ATLAS/CMS Dark Matter Forum" (July 2015). arXiv: 1507.00966 [hep-ex].

[73] V. A. Mitsou. "Overview of searches for dark matter at the LHC". In: *Journal of Physics: Conference Series* 651.1 (2015), p. 012023. DOI: 10.1088/1742-6596/651/1/012023.

[74] J. Goodman et al. "Constraints on dark matter from colliders". In: *Physical Review D* 82.11 (Dec. 2010), p. 116010. DOI: 10.1103/PhysRevD.82.116010.

[75] Y. Bai, P. J. Fox, and R. Harnik. "The Tevatron at the frontier of dark matter direct detection". In: *Journal of High Energy Physics* 2010.12 (Dec. 2010), p. 48. DOI: 10.1007/JHEP12(2010)048.

[76] D. Hooper and L. Goodenough. "Dark matter annihilation in the Galactic Center as seen by the Fermi Gamma Ray Space Telescope". In: *Physics Letters B* 697.5 (Mar. 2011), pp. 412–428. DOI: 10.1016/j.physletb.2011.02.029.

[77] M. L. Ahnen et al. "Limits to dark matter annihilation cross-section from a combined analysis of MAGIC and Fermi-LAT observations of dwarf satellite galaxies". In: *Journal of Cosmology and Astroparticle Physics* 2016.02 (Feb. 2016), p. 039. DOI: 10.1088/1475-7516/2016/02/039.

[78] O. Adriani et al. "An anomalous positron abundance in cosmic rays with energies 1.5-100 GeV". In: *Nature* 458.7238 (Apr. 2009), pp. 607–609. DOI: 10.1038/nature07942.

[79] M. Aguilar et al. "First Result from the Alpha Magnetic Spectrometer on the International Space Station: Precision Measurement of the Positron Fraction in Primary Cosmic Rays of 0.5–350 GeV". In: *Physical Review Letters* 110.14 (Apr. 2013), p. 141102. DOI: 10.1103/PhysRevLett.110.141102.

[80] S. Fukuda et al. "The Super-Kamiokande detector". In: *Nuclear Instruments and Methods in Physics Research Section A: Accelerators, Spectrometers, Detectors and Associated Equipment* 501.2-3 (Apr. 2003), pp. 418–462. DOI: 10.1016/S0168-9002(03)00425-X.

[81] M. Ageron et al. "ANTARES: The first undersea neutrino telescope". In: *Nuclear Instruments and Methods in Physics Research Section A: Accelerators, Spectrometers, Detectors and Associated Equipment* 656.1 (2011), pp. 11–38.

[82] A. Achterberg et al. "First year performance of the IceCube neutrino telescope". In: *Astroparticle Physics* 26.3 (Oct. 2006), pp. 155–173. DOI: 10.1016/j.astropartphys.2006.06.007.

[83] S.-L. Chen and Y. Zhang. "Isospin-violating dark matter and neutrinos from the Sun". In: *Physical Review D* 84.3 (Aug. 2011), p. 031301. DOI: 10.1103/PhysRevD.84.031301.

[84] F. Nesti and P. Salucci. "The Dark Matter halo of the Milky Way, AD 2013". In: *Journal of Cosmology and Astroparticle Physics* 2013.07 (July 2013), p. 016. DOI: 10.1088/1475-7516/2013/07/016.

[85] J. F. Navarro, C. S. Frenk, and S. D. M. White. "Simulations of X-ray clusters". In: *Monthly Notices of the Royal Astronomical Society* 275.3 (Aug. 1995), pp. 720–740. DOI: 10.1093/mnras/275.3.720.

[86] J. F. Navarro, C. S. Frenk, and S. D. M. White. "The Structure of Cold Dark Matter Halos". In: *The Astrophysical Journal* 462 (May 1996), p. 563. DOI: 10.1086/177173.

[87] A. Burkert. "The Structure of Dark Matter Halos in Dwarf Galaxies". In: *The Astrophysical Journal Letters* 447.1 (July 1995), pp. L25–L28. DOI: 10.1086/309560.

[88] B. Moore and J. Diemand. "Simulations of cold dark matter haloes". In: *Particle Dark Matter: Observations, Models and Searches*. Ed. by G. Bertone. Cambridge University Press, 2013. ISBN: 978-1-107-65392-4.

[89] W. J. G. de Blok, S. S. McGaugh, and V. C. Rubin. "High-Resolution Rotation Curves of Low Surface Brightness Galaxies. II. Mass Models". In: *The Astronomical Journal* 122.5 (2001), p. 2396. DOI: 10.1086/323450.

[90] D. Merritt. "Dark matter at the centres of galaxies". In: *Particle Dark Matter: Observations, Models and Searches*. Ed. by G. Bertone. Cambridge University Press, 2013. ISBN: 978-1-107-65392-4.

[91] S. Flis. "Searching for Dark Matter In the Galactic Center with the IceCube 79-String Detector ". PhD thesis. Stockholm University, Dec. 2014.

[92] M. Wolf. "Indirect Searches for Dark Matter in the Milky Way with IceCube-DeepCore". PhD thesis. Department of Physics, Stockholm University, 2016.

[93] T. Sjöstrand, S. Mrenna, and P. Skands. "A brief introduction to PYTHIA 8.1". In: *Computer Physics Communications* 178.11 (June 2008), pp. 852–867. DOI: 10.1016/j.cpc.2008.01.036.

[94] T. J. Bowles and V. N. Gavrin. "The Status of the Solar Neutrino Problem". In: *Annual Review of Nuclear and Particle Science* 43.1 (Dec. 1993), pp. 117–164. DOI: 10.1146/annurev.ns.43.120193.001001.

[95] K. A. Olive et al. "Review of Particle Physics". In: *Chinese Physics C* 38.9 (2014), p. 090001. DOI: 10.1088/1674-1137/38/9/090001.

[96] B. Pontecorvo. *Inverse beta processes and nonconservation of lepton charge*. 1958.

[97] Z. Maki, M. Nakagawa, and S. Sakata. "Remarks on the Unified Model of Elementary Particles". In: *Progress of Theoretical Physics* 28.5 (Nov. 1962), pp. 870–880. DOI: 10.1143/PTP.28.870.

[98] M. C. Gonzalez-Garcia, M. Maltoni, and T. Schwetz. "Updated fit to three neutrino mixing: status of leptonic CP violation". In: *Journal of High Energy Physics* 2014.11 (Nov. 2014), p. 52. DOI: 10.1007/JHEP11(2014)052.

[99] G. Drexlin et al. "Current Direct Neutrino Mass Experiments". In: *Advances in High Energy Physics* 2013.1–3 (2013), pp. 1–39. DOI: 10.1155/2013/293986.

[100] V. N. Aseev et al. "Upper limit on the electron antineutrino mass from the Troitsk experiment". In: *Physical Review D* 84.11 (Dec. 2011), p. 112003. DOI: 10.1103/PhysRevD.84.112003.

[101] S. Dell'Oro et al. "Neutrinoless Double Beta Decay: 2015 Review". In: *Advances in High Energy Physics* 2016.10 (2016), pp. 1–37. DOI: 10.1155/2016/2162659.

[102] C.-P. Ma. "Linear Power Spectra in Cold + Hot Dark Matter Models: Analytical Approximations and Applications". In: *The Astrophysical Journal* 471.1 (1996), p. 13. DOI: 10.1086/177949.

[103] N. Aghanim et al. "Planck intermediate results. XLVI. Reduction of large-scale systematic effects in HFI polarization maps and estimation of the reionization optical depth" (May 2016). arXiv: 1605.02985 [astro-ph.CO].

[104] N. Palanque-Delabrouille et al. "Neutrino masses and cosmology with Lyman-alpha forest power spectrum". In: *Journal of Cosmology and Astroparticle Physics* 2015.11 (Nov. 2015), p. 011. DOI: 10.1088/1475-7516/2015/11/011.

[105] S. Hannestad, J. Hamann, and Y. Y. Y. Wong. "Current and future constraints on neutrino physics from cosmology". In: *Journal of Physics: Conference Series* 485.1 (2014), p. 012008. DOI: 10.1088/1742-6596/485/1/012008.

[106] J. A. Formaggio and G. P. Zeller. "From eV to EeV: Neutrino cross sections across energy scales". In: *Reviews of Modern Physics* 84.3 (Sept. 2012), pp. 1307–1341. DOI: 10.1103/RevModPhys.84.1307.

[107] S. L. Glashow. "Resonant Scattering of Antineutrinos". In: *Physical Review* 118.1 (Apr. 1960), pp. 316–317. DOI: 10.1103/PhysRev.118.316.

[108] S. Tavernier. *Experimental Techniques in Nuclear and Particle Physics*. Brussels, Belgium: Springer-Verlag, 2010.

[109] R. Fernow. *Introduction to experimental particle physics*. Cambridge University Press, 1989. ISBN: 0 521 37940 7.

[110] D. Müller. "Electron Showers of High Primary Energy in Lead". In: *Physical Review D* 5.11 (June 1972), pp. 2677–2683. DOI: 10.1103/PhysRevD.5.2677.

[111] P. A. Cherenkov. "Nobel Lecture: Radiation of Particles Moving at a Velocity Exceeding That of Light, and Some of the Possibilities for Their Use in Experimental Physics". In: *Nobel Lecture* (Dec. 1958).

[112] D. Green. *The Physics of Particle Detectors*. Cambridge Monographs on Particle Physics, Nuclear Physics and Cosmology. Cambridge University Press, 2005.

[113] P. A. Cherenkov. "Visible luminescence of pure fluids induced by gamma rays ". In: *Dokl.Akad.Nauk Ser.Fiz.* (1934), pp. 451–454.

[114] I. M. Frank and I. Tamm. "Coherent visible radiation of fast electrons passing through matter". In: *Comptes Rendus de l'Academie des Sciences de l'URSS* 14.3 (1937), pp. 109–114.

[115] P. A. Cherenkov. "Visible Radiation Produced by Electrons Moving in a Medium with Velocities Exceeding that of Light". In: *Physical Review* 52.4 (Aug. 1937), pp. 378–379. DOI: 10.1103/PhysRev.52.378.

[116] D. J. Griffiths. *Introduction to Electrodynamics*. Fourth edition. Pearson Education Limited, 2013.

[117] K. Kleinknecht. *Detectors for Particle Radiation*. Cambridge University Press, 1998.

[118] L. Rädel and C. Wiebusch. "Calculation of the Cherenkov light yield from low energetic secondary particles accompanying high-energy muons in ice and water with Geant4 simulations". In: *Astroparticle Physics* 38 (Oct. 2012), pp. 53–67. DOI: 10.1016/j.astropartphys.2012.09.008.

[119] P. Blasi. "The origin of galactic cosmic rays". In: *The Astronomy and Astrophysics Review* 21.1 (Nov. 2013), p. 70. DOI: 10.1007/s00159-013-0070-7.

[120] R. Engel, D. Heck, and T. Pierog. "Extensive Air Showers and Hadronic Interactions at High Energy". In: *Annual Review of Nuclear and Particle Science* 61.1 (Nov. 2011), pp. 467–489. DOI: 10.1146/annurev.nucl.012809.104544.

[121] M. G. Aartsen et al. "Anisotropy in Cosmic-Ray Arrival Directions in the Southern Hemisphere Based on Six Years of Data From the Icecube Detector". In: *The Astrophysical Journal* 826.2 (Aug. 2016), p. 220. DOI: 10.3847/0004-637X/826/2/220.

[122] M. G. Aartsen et al. "Determining neutrino oscillation parameters from atmospheric muon neutrino disappearance with three years of IceCube DeepCore data". In: *Physical Review D* 91.7 (Apr. 2015), p. 072004. DOI: 10.1103/PhysRevD.91.072004.

[123] M. Honda et al. "Atmospheric neutrino flux calculation using the NRLMSISE-00 atmospheric model". In: *Physical Review D* 92.2 (July 2015), p. 023004. DOI: 10.1103/PhysRevD.92.023004.

[124] X. Bertou, M. Boratav, and A. Letessier-Selvon. "Physics of Extremely High Energy Cosmic Rays". In: *International Journal of Modern Physics A* 15 (2000), p. 2181. DOI: 10.1016/S0217-751X(00)00090-2.

[125] M. G. Aartsen et al. "Evidence for High-Energy Extraterrestrial Neutrinos at the IceCube Detector". In: *Science* 342.6161 (Nov. 2013), p. 1242856. DOI: 10.1126/science.1242856.

[126] D. Besson et al. "Radio Frequency Birefringence in South Polar Ice and Implications for Neutrino Reconstruction" (May 2010). arXiv: 1005.4589 [astro-ph.IM].

[127] S. W. Barwick et al. "Greenland '90: A First Step Toward Using the Polar Ice Cap as a Cherenkov Detector". In: *International Trends in Astroparticle Physics* (1992), pp. 413–417.

[128] E. Andrés et al. "Observation of high-energy neutrinos using Cherenkov detectors embedded deep in Antarctic ice". In: *Nature* 410.6827 (Mar. 2001), pp. 441–443. DOI: 10.1038/35068509.

[129] S. L. Miller. "Clathrate Hydrates of Air in Antarctic Ice". In: *Science* 165.3892 (Aug. 1969), pp. 489–490. DOI: 10.1126/science.165.3892.489.

[130] P. B. Price, K. Woschnagg, and D. Chirkin. "Age vs depth of glacial ice at South Pole". In: *Geophysical Research Letters* 27.14 (July 2000), pp. 2129–2132. DOI: 10.1029/2000GL011351.

[131] M. G. Aartsen et al. "Measurement of South Pole ice transparency with the IceCube LED calibration system". In: *Nuclear Instruments and Methods in Physics Research Section A: Accelerators, Spectrometers, Detectors and Associated Equipment* 711 (May 2013), pp. 73–89. DOI: 10.1016/j.nima.2013.01.054.

[132] N. E. Bramall et al. "A deep high-resolution optical log of dust, ash, and stratigraphy in South Pole glacial ice". In: *Geophysical Research Letters* 32.21 (2005), p. L21815. DOI: 10.1029/2005GL024236.

[133] R. C. Bay et al. "South Pole paleowind from automated synthesis of ice core records". In: *Journal of Geophysical Research* 115.D14 (July 2010), p. D14126. DOI: 10.1029/2009JD013741.

[134] R. C. Smith and K. S. Baker. "Optical properties of the clearest natural waters (200–800 nm)". In: *Applied Optics* 20.2 (1981), pp. 177–184. DOI: 10.1364/AO.20.000177.

[135] J. A. Aguilar et al. "Transmission of light in deep sea water at the site of the Antares neutrino telescope". In: *Astroparticle Physics* 23.1 (Feb. 2005), pp. 131–155. DOI: 10.1016/j.astropartphys.2004.11.006.

[136] M. G. Aartsen et al. "The IceCube Neutrino Observatory Part VI: Ice Properties, Reconstruction and Future Developments" (Sept. 2013). arXiv: 1309.7010 [astro-ph.HE].

[137] A. Karle and K. Woschnagg. *Hole Ice Studies with YAG Data/MC*. Tech. rep. Sept. 1998.

[138] R. Abbasi et al. "The IceCube data acquisition system: Signal capture, digitization, and timestamping". In: *Nuclear Instruments and Methods in Physics Research Section A: Accelerators, Spectrometers, Detectors and Associated Equipment* 601.3 (Apr. 2009), pp. 294–316. DOI: 10.1016/j.nima.2009.01.001.

[139] E. Calvo et al. "Characterization of large-area photomultipliers under low magnetic fields: Design and performance of the magnetic shielding for the Double Chooz neutrino experiment". In: *Nuclear Instruments and Methods in Physics Research Section A: Accelerators, Spectrometers, Detectors and Associated Equipment* 621.1-3 (Sept. 2010), pp. 222–230. DOI: 10.1016/j.nima.2010.06.009.

[140] K. Hoshina, K. Mase, and M. Inaba. *DOM Acceptance Table for Photonics and Romeo*. Tech. rep. 2007.

[141] R. Abbasi et al. "Calibration and characterization of the IceCube photomultiplier tube". In: *Nuclear Instruments and Methods in Physics Research Section A: Accelerators, Spectrometers, Detectors and Associated Equipment* 618.1-3 (June 2010), pp. 139–152. DOI: 10.1016/j.nima.2010.03.102.

[142] R. Abbasi et al. "The design and performance of IceCube DeepCore". In: *Astroparticle Physics* 35.10 (May 2012), pp. 615–624. DOI: 10.1016/j.astropartphys.2012.01.004.

[143] K. Woschnagg. *Ice Shear Measurement*. Tech. rep. 2009.

[144] R. Bay. *Inclinometers*. Tech. rep. 2013.

[145] M. J. Larson. "Simulation and Identification of Non-Poissonian Noise Triggers in the Icecube Neutrino Detector". MA thesis. University of Alabama, 2013.

[146] M. G. Aartsen et al. "Energy reconstruction methods in the IceCube neutrino telescope". In: *Journal of Instrumentation* 9.03 (Mar. 2014), P03009. DOI: 10.1088/1748-0221/9/03/P03009.

[147] C. Andreopoulos et al. "The GENIE neutrino Monte Carlo generator". In: *Nuclear Instruments and Methods in Physics Research Section A: Accelerators, Spectrometers, Detectors and Associated Equipment* 614.1 (Feb. 2010), pp. 87–104. DOI: 10.1016/j.nima.2009.12.009.

[148] A. Gazizov and M. Kowalski. "ANIS: High energy neutrino generator for neutrino telescopes". In: *Computer Physics Communications* 172.3 (Nov. 2005), pp. 203–213. DOI: 10.1016/j.cpc.2005.03.113.

[149] D. Heck et al. "CORSIKA: a Monte Carlo code to simulate extensive air showers". In: *FZKA 6019* (Feb. 1998).

[150] R. S. Fletcher et al. "SIBYLL: An event generator for simulation of high energy cosmic ray cascades". In: *Physical Review D* 50.9 (Nov. 1994), pp. 5710–5731. DOI: 10.1103/PhysRevD.50.5710.

[151] T. K. Gaisser. "Spectrum of cosmic-ray nucleons, kaon production, and the atmospheric muon charge ratio". In: *Astroparticle Physics* 35.12 (July 2012), pp. 801–806. DOI: 10.1016/j.astropartphys.2012.02.010.

[152] J. H. Koehne et al. "PROPOSAL: A tool for propagation of charged leptons". In: *Computer Physics Communications* 184.9 (Sept. 2013), pp. 2070–2090. DOI: 10.1016/j.cpc.2013.04.001.

[153] S. Agostinelli et al. "Geant4—a simulation toolkit". In: *Nuclear Instruments and Methods in Physics Research Section A: Accelerators, Spectrometers, Detectors and Associated Equipment* 506.3 (July 2003), pp. 250–303. DOI: 10.1016/S0168-9002(03)01368-8.

[154] C. Weaver. "Evidence for Astrophysical Muon Neutrinos from the Northern Sky ". PhD thesis. University of Wisconsin–Madison, 2015.

[155] F. Aharonian et al. "HESS Observations of the Galactic Center Region and Their Possible Dark Matter Interpretation". In: *Physical Review Letters* 97.22 (Nov. 2006), p. 221102. DOI: 10.1103/PhysRevLett.97.221102.

[156] S. Euler. "Observation of oscillations of atmospheric neutrinos with the IceCube Neutrino Observatory ". PhD thesis. RWTH Aachen, Feb. 2014.

[157] M. G. Aartsen et al. "Search for dark matter annihilation in the Galactic Center with IceCube-79". In: *The European Physical Journal C* 75.10 (Oct. 2015), p. 492. DOI: 10.1140/epjc/s10052-015-3713-1.

[158] S. Boyd and L. Vandenberghe. *Convex Optimization*. 2nd ed. Cambridge University Press, 2009. ISBN: 978-0-521-83378-3.

[159] M. G. Aartsen et al. "Improvement in fast particle track reconstruction with robust statistics". In: *Nuclear Instruments and Methods in Physics Research Section A: Accelerators, Spectrometers, Detectors and Associated Equipment* 736 (Feb. 2014), pp. 143–149. DOI: 10.1016/j.nima.2013.10.074.

[160] J. Ahrens et al. "Muon track reconstruction and data selection techniques in AMANDA". In: *Nuclear Instruments and Methods in Physics Research Section A: Accelerators, Spectrometers, Detectors and Associated Equipment* 524.1-3 (May 2004), pp. 169–194. DOI: 10.1016/j.nima.2004.01.065.

[161] D. Pandel. "Bestimmung von Wasser- und Detektorparametern und Rekonstruktion von Myonen bis 100 TeV mit dem Baikal-Neutrinoteleskop NT-72". PhD thesis. Humboldt-Universität zu Berlin, 1996.

[162] T. Neunhöffer. "Estimating the angular resolution of tracks in neutrino telescopes based on a likelihood analysis". In: *Astroparticle Physics* 25.3 (Apr. 2006), pp. 220–225. DOI: 10.1016/j.astropartphys.2006.01.002.

[163] J.-P. Hülß. "Search for Neutrinos from the Direction of the Galactic Center with the IceCube Neutrino Telescope ". PhD thesis. RWTH Aachen, Tech. Hochsch., Nov. 2010.

[164] Y. Freund and R. E. Schapire. "A Decision-Theoretic Generalization of On-Line Learning and an Application to Boosting". In: *Journal of Computer and System Sciences* 55.1 (Aug. 1997), pp. 119–139. DOI: 10.1006/jcss.1997.1504.

[165] J. P. Y. Garza. "Measurement of neutrino oscillations in atmospheric neutrinos with the IceCube DeepCore detector". PhD thesis. Humboldt-Universität zu Berlin, Mathematisch-Naturwissenschaftliche Fakultät I, June 2014.

[166] F. Feroz, M. P. Hobson, and M. Bridges. "MultiNest: an efficient and robust Bayesian inference tool for cosmology and particle physics". In: *Monthly Notices of the Royal Astronomical Society* 398.4 (Oct. 2009), pp. 1601–1614. DOI: 10.1111/j.1365-2966.2009.14548.x.

[167] A. Hoecker et al. "TMVA - Toolkit for Multivariate Data Analysis". In: *Proceedings of Science, XI International Workshop on Advanced Computing and Analysis Techniques in Physics Research* (Mar. 2007), p. 040. arXiv: physics/0703039 [physics.data-an].

[168] J. Neyman. "Outline of a Theory of Statistical Estimation Based on the Classical Theory of Probability". In: *Philosophical Transactions of the Royal Society A: Mathematical, Physical and Engineering Sciences* 236.767 (Aug. 1937), pp. 333–380. DOI: 10.1098/rsta.1937.0005.

[169] G. J. Feldman and R. D. Cousins. "Unified approach to the classical statistical analysis of small signals". In: *Physical Review D* 57.7 (Apr. 1998), pp. 3873–3889. DOI: 10.1103/PhysRevD.57.3873.

[170] J. Lundberg et al. "Light tracking through ice and water—Scattering and absorption in heterogeneous media with Photonics". In: *Nuclear Instruments and Methods in Physics Research Section A: Accelerators, Spectrometers, Detectors and Associated Equipment* 581.3 (Nov. 2007), pp. 619–631. DOI: 10.1016/j.nima.2007.07.143.

[171] M. Rongen. "Measuring the optical properties of IceCube drill holes". In: *EPJ Web of Conferences* 116 (Apr. 2016), p. 06011. DOI: 10.1051/epjconf/201611606011.

[172] J. Feintzeig. "Searches for Point-like Sources of Astrophysical Neutrinos with the IceCube Neutrino Observatory ". PhD thesis. University of Wisconsin–Madison, Aug. 2014.

[173] M. G. Aartsen et al. "IceCube search for dark matter annihilation in nearby galaxies and galaxy clusters". In: *Physical Review D* 88.12 (Dec. 2013), p. 122001. DOI: 10.1103/PhysRevD.88.122001.

[174] M. G. Aartsen et al. "Multipole analysis of IceCube data to search for dark matter accumulated in the Galactic halo". In: *The European Physical Journal C* 75.1 (Jan. 2015), p. 20. DOI: 10.1140/epjc/s10052-014-3224-5.

[175] M. G. Aartsen et al. "All-flavour Search for Neutrinos from Dark Matter Annihilations in the Milky Way with IceCube/DeepCore". In: *The European Physical Journal C* 76.10 (Sept. 2016), p. 531. DOI: 10.1140/epjc/s10052-016-4375-3.

[176] K. Frankiewicz. "Searching for Dark Matter Annihilation into Neutrinos with Super-Kamiokande" (Oct. 2015). arXiv: 1510.07999 [hep-ex].

[177] J. Zornoza. "Results on Dark Matter Searches with the ANTARES Neutrino Telescope". In: *Nuetrino 2016*. IFIC (UV-CSIC), Spain. July 2016.

[178] E. Aliu et al. "VERITAS deep observations of the dwarf spheroidal galaxy Segue 1". In: *Physical Review D* 85.6 (Mar. 2012), p. 062001. DOI: 10.1103/PhysRevD.85.062001.

[179] R. Bartels, S. Krishnamurthy, and C. Weniger. "Strong Support for the Millisecond Pulsar Origin of the Galactic Center GeV Excess". In: *Physical Review Letters* 116.5 (Feb. 2016), p. 051102. DOI: 10.1103/PhysRevLett.116.051102.

[180] M. Aaboud et al. "Search for new phenomena in final states with an energetic jet and large missing transverse momentum in ppcollisions at s=13âĂŁâĂŁTeVusing the ATLAS detector". In: *Physical Review D* 94.3 (Aug. 2016), p. 032005. DOI: 10.1103/PhysRevD.94.032005.

[181] M. G. Aartsen et al. "The IceCube Neutrino Observatory - Contributions to ICRC 2015 Part IV: Searches for Dark Matter and Exotic Particles" (Oct. 2015).

[182] S. Adrián-Martínez et al. "Letter of intent for KM3NeT 2.0". In: *Journal of Physics G: Nuclear and Particle Physics* 43.8 (June 2016), p. 084001. DOI: 10.1088/0954-3899/43/8/084001.

[183] M. G. Aartsen et al. "Letter of Intent: The Precision IceCube Next Generation Upgrade (PINGU)" (Jan. 2014). arXiv: 1401.2046 [physics.ins-det].

[184] M. G. Aartsen et al. "IceCube-Gen2: A Vision for the Future of Neutrino Astronomy in Antarctica" (Dec. 2014). arXiv: 1412.5106 [astro-ph.HE].